Stony Brook University

Coherent Quasiparticle Transport in Multi-Antidot Structures with Potential Applications to Quantum Information

A Dissertation Presented

by

James Albert Nesteroff

to

The Graduate School

in Partial Fulfillment of the Requirements

for the Degree of

Doctor of Philosophy

in

Physics

Stony Brook University

May 2009

Stony Brook University

The Graduate School

James Albert Nesteroff

We, the dissertation committee for the above candidate for the Doctor of Philosophy degree, hereby recommend acceptance of this dissertation.

Dmitri V. Averin – Dissertation Advisor
Professor, Department of Physics and Astronomy

Ismail Zahed – Chairperson of Defense
Professor, Department of Physics and Astronomy

Vladimir J. Goldman
Professor, Department of Physics and Astronomy

Leon Takhtajan
Professor, Department of Mathematics
Stony Brook University

This dissertation is accepted by the Graduate School.

Lawrence Martin
Dean of the Graduate School

Abstract of the Dissertation

Coherent Quasiparticle Transport in Multi-Antidot Structures with Potential Applications to Quantum Information

by

James Albert Nesteroff

Doctor of Philosophy

in

Physics

Stony Brook University

2009

The two dimensional electron gas in the regime of the Fractional Quantum Hall Effect is one of the hallmarks of condensed matter physics. One of its main characteristic features is that quasiparticle excitations of this system exhibit both fractional charge and fractional "anyonic" exchange statistics. Experiments involving resonant quasiparticle tunnelling through Quantum Antidots have demonstrated the potential to manipulate individual quasiaprticles. It is also known that the anyonic exchange statistics of the quasiparticles can be exploited for use in Quantum Information. The basic building block for this type of Quantum Information processing is the FQHE qubit which is formed from two tunnel coupled quantum antidots. In the first part of this dissertation, a model describing the coherent tunnelling of quasiparticles of quantum hall liquids in a system consisting of multiple antidots will be discussed. The main result is that the anyonic exchange statistics of these quasiparticles is manifested directly in the DC tunnel con-

ductance of these systems even in the absence of quasiparticle exchange. Most notably, it will be shown that in tunnelling through a line of three antidots, the statistics should be exhibited as a non-vanishing resonant peak of the tunnel conductance. The second half will be dedicated in part to exploring the potential use of FQHE qubits in applications involving Quantum Information. To begin with, the Quantum Antidot Electrometer will be discussed as a detector for quantum measurements of FQHE qubits. Next, the non-trivial aspects of wave function reduction will be examined as well as the coherent synchronization of oscillations in a continuously measured double qubit system. The dissertation concludes with an examination of a different paradigm in Quantum Information processing namely that of adiabatic quantum computation (AQC). Due to the ground state evolution of AQC it is expected that this scheme provides a measure of protection against environmental decoherence. The stability of this scheme of quantum computation is assessed with respect to decoherence induced by low frequency noise which is of particular relevance to solid state implementations of AQC.

This thesis is dedicated to all those who have helped me over the years to achieve my dream.

Contents

List of Figures

List of Abbreviations

- **AQC** - Adiabatic Quantum Computation
- **CQED** - Circuit Quantum Electrodynamics
- **CLL** - Chiral Luttinger Liquid
- **FL** - Fermi Liquid
- **FQHE** - Fractional Quantum Hall Effect
- **IQHE** - Integer Quantum Hall Effect
- **LL** - Landau Level
- **LZ** - Landau Zener
- **QAD** - Quantum Antidot
- **QAE** - Quantum Antidot Electrometer
- **QC** - Quantum Computation
- **QI** - Quantum Information

Acknowledgements

Over the past four and half years there have been many people who have helped pave my way through graduate school. Without their help and kindness I would not have been able to come this far.

First and foremost, I would like to thank my thesis advisor Prof. Dmitri Averin for all the many years of support that he has given to me. I've always appreciated his patience and his help whenever I encountered one of the numerous bumps along the road both in life and with research. He has always been there to help me get on the right path. It is both through his example and teaching that I learned what it takes to be a real scientist.

I would also like to express my sincere thanks to the members of my committee; Professors Vladimir Goldman, Ismail Zahed, and Leon Takhtajan. I appreciate them taking the time to read over my thesis and attend my dissertation defense. Also, I want to acknowledge Professor Goldman, Fernando Camino, and Wei Zhou for the many useful conversations I have had with them in the process of completing this work.

Finally, I am truly grateful for all the love and support my family has given me throughout the past ten years of my education. My parents have always been there to support my dreams and help me to achieve them. For that, I cannot possibly thank them enough. My wife, Megan, with her unending love and compassion has always given me the strength to keep going even in the most difficult times.

There are many others who have contributed to helping me get where I am today. Though their names may not be listed here, they have my deepest gratitude for all of their efforts.

List of Publications

M. H. S. Amin, D. V. Averin, and J. A. Nesteroff, "Decoherence in Adiabatic Quantum Computation", Physical Review A **79**, 022107 (2009)

D. V. Averin and J. A. Nesteroff, "Coulomb Blockade of Anyons", Physical Review Letters **99**, 096801 (2007)

D. V. Averin and J. A. Nesteroff, "Correlated transport of FQHE quasiparticles in a double-antidot system", Physica E **40**, 58 (2007)

Chapter 1

Introduction

Ever since its discovery in 1982 by Tsui, Störmer, and Gossard [1] the Fractional Quantum Hall Effect (FQHE) has become one of the cornerstones of condensed matter physics. The FQHE is found in low-temperature, 2-dimensional electron gas systems (2DEG). This effect refers to the simultaneous quantization of the Hall Resistance R_H in simple fractions of h/e^2 and vanishing of the magnetoresistance as shown in Fig. 1.1. What makes this effect so unique, lies in the fact that it arises due to non-perturbative many-body correlations of the electrons. Furthermore, this is in direct contrast to the underlying physics of its predecessor, the Integer Quantum Hall Effect (IQHE) [2] wherein one finds the formation of plateaus in the Hall Resistance occurring at $R_H = h/(je^2)$, where j is an integer. This can be explained by a non-interacting electron model whereby each of the plateaus correspond to the complete filling of j Landau levels. To gain insight into the reason for the strongly interacting nature of the FQHE, consider the case when only the lowest Landau-Level is completely filled, corresponding to the $j = 1$ IQHE. Further increasing the magnetic field implies that more states are made available then there are electrons. In this highly degenerate ground state, the interactions between electrons become important and the net result is a strongly correlated electron liquid. These correlations were explained by Laughlin's [3] variational wave function which incorporates the effects of electron-electron interaction. One of the most fascinating predictions to come from Laughlin's theory is that the low energy excitations or quasiparticles of primary quantum Hall liquids, where the filling factor is $\nu = 1/(2j + 1)$, have both fractional charge [3, 4] $e^* = \nu e$ and, even more unusual, fractional (or anyonic) exchange statistics [5, 6].

In 1995, one aspect of these quasiparticles, namely the fractional charge, was experimentally confirmed by Goldman and Su [7]. Their experiment utilized quantum antidots, which are lithographically defined potential hills in

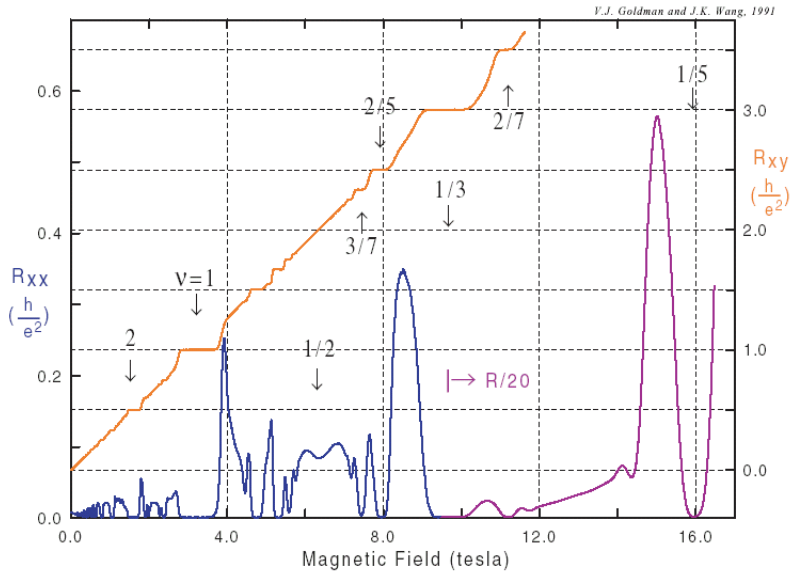

Figure 1.1: The Integer and Fractional Quantum Hall effects. Whenever the magnetic field is tuned such that the filling factor ν is either integral (IQHE) or fractional (FQHE) the Hall resistance $R_H = R_{xy}$ (shown in red) reaches a plateau with value $h/(e^2\nu)$. When the Hall Resistance is quantized the magnetoresistance R_{xx} vanishes. Figure courtesy of V. Goldman.

a 2DEG. In an antidot, the combined action of the electric and magnetic fields effectively localizes quasiparticles into orbits about the potential hill. By studying the tunnel conductance of a single antidot coupled to two opposing edge states in the limit in which the temperature is small compared to the energy gap of quasiaprticles on the antidot, which requires that the size of the antidot is small enough, they were able to deduce the charge of the quasiparticles. Subsequent experiments observed this charge fractionalization in shot noise measurements involving edge state tunnelling [8, 9].

The situation concerning the experimental confirmation of fractional exchange statistics of quasiparticles is somewhat more uncertain. Currently, experiments [10, 11] demonstrating the unusual flux periodicity of the conductance of a quasiparticle interferometer can be interpreted as a manifestation of fractional quasiparticle exchange statistics [12, 13]. However, this is not universally accepted [14, 15].

On a separate but equally intriguing path of development, there has been interest for some time in the implementation of quantum computation (QC) based on anyonic exchange statistics [16–19]. In this "topological" QC two or

more particles possessing anyonic exchange statistics are intertwined with one another. Braiding the particles translates into unitary transformations of the system wave function, which are then used as gate operations to implement quantum logic.

A practical implementation of this form of QC was proposed [20] using antidots operating in the primary FQHE regime as qubits. Here, a single FQHE qubit consists of two antidots with the basis states being defined as a single quasiparticle localized on one antidot or the other. In order to perform gate operations structures containing multiple antidots are required, where intertwining particles can be accomplished through an adiabatic transfer of a quasiparticle from one antidot to another.

The aforementioned uses of antidots illustrate their versatility in both charge transport experiments and quantum computation and information. Reflecting this "duality", this thesis is comprised of two parts. In the first part, we investigate the conductance of quasiparticle transport in structures involving multiple antidots. Up until now, only *single* antidot transport has been studied from both an experimental [7, 21–23] and theoretical [24, 25] perspective, where multi-antidot transport has remained an open question. Thus, in Chapter 2, we present a model for correlated quasiparticle transport in a serially coupled double-antidot. It is shown that the strongly correlated nature of the edge states to which this system is coupled is exhibited in the DC conductance peaks. However, the anyonic statistics of quasiparticles on the antidots does not manifest itself in this system. In Chapter 3, we extend our model of multi-antidot transport to systems consisting of three antidots in which the effects of the fractional exchange statistics of the quasiparticles enter directly into the tunnel conductance. We propose an experimentally viable setup which should allow for the unambiguous determination of the fractional exchange statistics of quasiparticles.

The second half of the thesis is dedicated to an exploration of some possible applications involving the use of antidots in Quantum Information. The goal of Chapter 4 is to analyze the use of the Quantum Antidot Electrometer (QAE) as a measurement device for a single FQHE qubit in the framework of linear measurement theory [26, 27]. The emphasis here is on showing how the Luttinger liquid effects from the edge states determine the measurement characteristics of this detector. Chapters 5 and 6 investigate two interesting aspects of quantum measurement involving antidots as qubits.

The final chapter of the thesis examines two interrelated topics. The first concerns adiabatic quantum computation (AQC), a paradigm of QC wherein a system of qubits is initially prepared in the ground state of some known and relatively simple Hamiltonian. Quantum computations are performed then by

evolving system Hamiltonian slowly enough so that it remains in the ground state throughout the duration of the computation. The structure of the total Hamiltonian is such so that at the end of the computation the ground state of the system represents the solution to some complex computational problem. The main advantage of performing QC this way is that adiabatic evolution implies that there is some measure of protection against environmentally induced decoherence. However, in cases where the decoherence is caused by low frequency noise, which is typical for implementations with solid state flux qubits, this protection as we shall show is not complete.

Our model for evaluating the performance of AQC in a noisy environment concerns the dynamics of the system in the vicinity of the anti-crossing between the two lowest energy levels of the system Hamiltonian and is thus mapped onto the Landau-Zener problem in the presence of an environment. A secondary focus of this chapter examines the behavior of Landau-Zener transitions in the presence of a simple environment made up of a single Harmonic oscillator. Besides serving as an aid to understanding the modifications to LZ transitions in two level systems coupled to environments, such a model can also be realized in current experiments involving coupled qubit-oscillator systems [28–30]. We show that non-trivial modifications to the LZ transition probability occur when the oscillator is prepared in a thermal state, which is realizable in current experiments [30]. Furthermore, these modifications are most pronounced when the thermal occupancy of the oscillator states is large.

The outline for the remainder of this chapter is as follows. In the next section, we present an overview of the FQHE as well as the hydrodynamic theory of the edge states, and conclude with a discussion of antidots and the quantum antidot electrometer. In Section 1.2, we briefly discuss quantum information theory including the use of antidots as qubits and conclude with an introduction to the concept of AQC.

1.1 The Fractional Quantum Hall Effect

As pointed out earlier, both the IQHE and FQHE occur in systems in which electrons are confined to move in two dimensions. The physics of a non-interacting 2DEG with a magnetic field B applied perpendicular to it can be described in terms of Landau-Levels (LL). Assuming the electrons are free to move within the x-y plane and the magnetic field points in the z-direction, the single particle energies for the N-th LL (neglecting spin) are given by

$$E_N = E_z + \hbar\omega_o(N + 1/2) \tag{1.1}$$

where, $\omega_o = eB/m^*$ is the cyclotron frequency, m^* is the effective mass of the electrons, and E_z is the energy in the z-direction. Each LL has a large degeneracy associated with it. The degeneracy per unit area of a level is given by $D = B/\phi_o$, with $\phi_o = h/e$ being the quantum of magnetic flux. From this, one can define the filling factor $\nu = hn_d/(eB)$ which is the ratio of the electron concentration n_d to the number of states per unit area. By increasing the magnetic field, the number of states available in the LL increases and, since the electron concentration is independent of the magnetic field, ν decreases. When the field is tuned such that only the lowest LL is filled, a further increase of B implies that there are more states available than there are electrons to fill them. This produces qualitatively new electron-electron correlations.

The above discussion implies that to understand the underlying physics of the FQHE, where $\nu < 1$, one needs to take into account the effect of many-body interactions in a non-perturbative manner. In his seminal work [3], Laughlin was able to find the ground states for primary FQHE liquids with $\nu = 1/(2j+1)$ and $j = 1, 2, ...$ which are given via the "Laughlin" wave function, which in its unnormalized form is,

$$\psi_j(z_k) = \prod_{k<l}(z_k - z_l)^{1/\nu} e^{-\sum_k^N \frac{|z_k|^2}{4}}. \tag{1.2}$$

Although, strictly speaking, this is an approximate wave function describing electrons with *short-range* interactions. Nevertheless, Eq. (1.2) provides excellent agreement when compared to the exact ground state wave function found from numerical finite size studies and to experimental results.

One of the most fascinating predictions afforded by the Laughlin wave function is that the low-energy excitations or quasiparticles of the ground state of primary quantum Hall liquids have both fractional charge and fractional exchange statistics. The former property can be seen by considering the wave function for a "quasihole" excitation located at a point z_o in the liquid, which is given by

$$\psi(z_o) = \prod_i (z_i - z_0)\psi_j(z_i). \tag{1.3}$$

The interpretation of the above equation is that it describes a small depletion region formed in the quantum hall liquid. The charge of this quasiparticle was determined to be equal to $e^* = \nu e$ [3, 5].

In order to determine the exchange statistics of the particles, Arovas *et al.* [5] calculated the phase accumulated by the wave function, when one quasiparticle is adiabatically encircled by another. Consider the Laughlin wave

function for two quasiholes located at points z and z',

$$\psi(z', z) = \prod_i (z_i - z')(z_i - z)\psi_j(z_i). \tag{1.4}$$

In the case when z is fixed, adiabatically bringing z' around a closed loop (enclosing the particle at z) implies that the wave function (1.4) becomes,

$$\psi[z'(t), z] = \psi[z', z]e^{i\phi}. \tag{1.5}$$

The phase acquired by the wave function corresponds to the adiabatic, or Berry's phase, this is given by,

$$\phi = i \oint < \psi[z'(t), z]|\frac{d}{dt}|\psi[z'(t), z] > dt \tag{1.6}$$

and $\phi = \phi_{AB} + \gamma$. The first part, ϕ_{AB} is the Aharonov-Bohm (AB) phase acquired by the quasiparticle as it encircles an area enclosing the magnetic field B with vector potential $\overrightarrow{A}$ or,

$$\phi_{AB} = \frac{e^*}{\hbar} \oint \overrightarrow{A} \cdot dl = \frac{2\pi e^* \Phi}{e\phi_o} \tag{1.7}$$

where ϕ_o is the flux quantum and Φ is the enclosed flux. The part $\gamma = 2\pi\nu$ is the change of phase ϕ due to the presence of the second quasiparticle. Therefore, the exchange statistics of these particles can be found by considering only half a revolution of z' thereby implying that,

$$\psi(z', z) = e^{-i\pi\nu}\psi(z, z') \tag{1.8}$$

where $\theta = \pi\nu$ and the sign of the exponent is dependent on the direction in which z' was rotated. Thus, Eq. (1.8) shows that for the exchange statistics of quasiparticles of primary FQHE liquids can be fractional (i.e. $\theta = \pi/m$, $m = 3, 5, ...$). Note that all of the above arguments hold for quasielectrons as well. The fact that these particles can exhibit fractional exchange statistics is a direct result of the two dimensional nature of this system. In fact, the very notion that particles in two dimensions could possess statistics that are between fermions ($\theta = \pi$) and bosons ($\theta = 0, 2\pi$) had been predicted from general considerations [31, 32]. One way to understand the unusual exchange statistics of these particles is to think of the quasiparticle located at z to be an infinitely small flux tube with flux ϕ_o. When the charge e^*, located at z', is rotated around the particle the total AB phase picked by the wave function is $2\pi\nu$. Therefore, the exchange statistics of the quasiparticles can be thought

of as the exchange of a particle of charge e^* and a flux tube [32].

1.1.1 Edge States and the Chiral Luttinger Liquid

We now turn our attention to a different aspect of the FQHE, namely the properties of edge states. The liquid is confined by some potential which produces an electric field $\overrightarrow{E}$ at the edge as shown in Fig. 1.2a. For the sake of

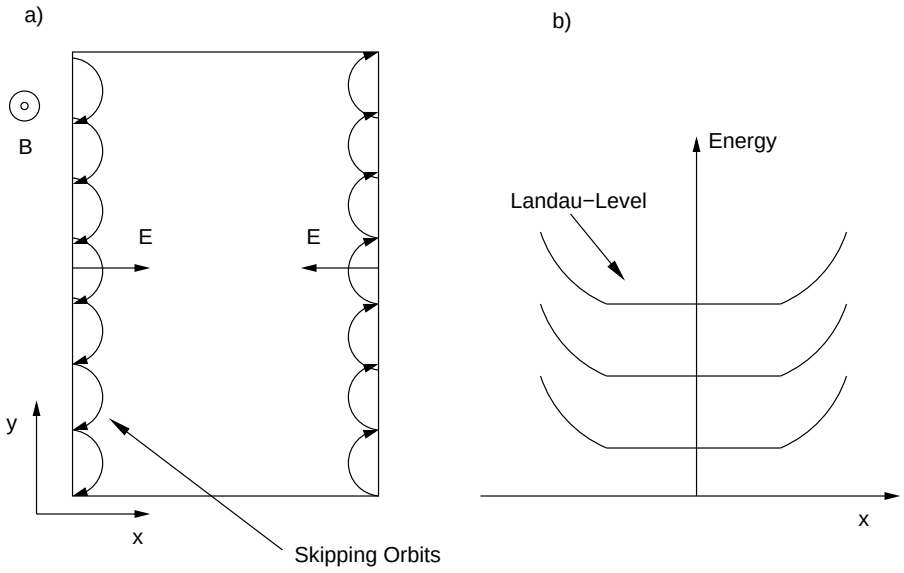

Figure 1.2: (a) Schematic of a Quantum Hall sample. The electric field due to the confinement potential points inward and the combined action of the electric and magnetic field cause the electrons to execute skipping orbits along the edge. (b) In the quantum mechanical picture, the Landau levels bend upward near the edge of sample causing the electrons to acquire a net velocity that depends on which side of the sample the electron is on.

simplicity, consider the case of the IQHE. The confining potential causes the energy of the Landau Levels to acquire a spatial dependence [33], the behavior of which is schematically represented in Fig. 1.2b. From a semiclassical viewpoint, the combined action of the electric and magnetic fields implies that the electrons near the edges of the sample skip off of the wall created by the confinement potential and acquire a velocity whose magnitude is given by $v = E/B$, where $E = |\overrightarrow{E}|$. Therefore, the effect of the confinement potential is to create a persistent current which flows along the sample boundary. Furthermore, the direction or *chirality* of this current is fixed by the sign of the magnetic field

and, due to the strength of the magnetic field, electron transport along the edges can be considered as quasi-one dimensional.

In the FQHE regime, Wen [34–38] suggested the Chiral Luttinger Liquid (CLL) theory which is an effective low energy description of the edge states. In this description, the underlying assumption is that the strongly correlated nature of the electron system extends all the way to edge states. To see this one can use the following heuristic argument. Consider the Laughlin wave function given in Eq. (1.2) and confine the electron coordinate to a one-dimensional circle of radius R which one can imagine to be the edge of the sample. Thus, $z_k = Re^{i\phi_k}$ where ϕ_k is the angular coordinate along the disk of the circle. The wave function describing the outside edge of the circle is then given by,

$$\psi_j \sim \prod_{k<l} (e^{i\phi_k} - e^{i\phi_l})^{1/\nu}. \tag{1.9}$$

What is important to notice is the wave function that it resembles, up to a normalization constant, is the same ground state wave function of the Calogero-Sutherland model which describes interacting one dimensional electrons[1].

One of the main characteristics of the Luttinger (or Tomonaga-Luttinger) model is that the low energy excitations of the electron gas are described in terms of bosonic excitations. Due to the fact that the electron dispersion relation is linearized about the two Fermi points $\pm k_f$, the model describes both left and right moving electrons. However, because of the chirality of the FQHE liquid, edge state electrons propagate in opposite directions on opposing sides of the sample. Furthermore, tunnelling between these states is exponentially suppressed as a function of the distance between them. Thus, backscattering between opposing edge states is negligible unless they are brought into close proximity with one another.

In the hydrodynamic formulation of CLL[2], the edge excitations of an FQHE droplet exist in the form of surface wave, that propagates in only one direction, as shown schematically in Fig. (1.3). Since the FQHE liquid is both incompressible and irrotational, the dynamics of the wave can be described by the classical wave equation,

$$\partial_t \rho(x) = u \partial_x \rho(x) \tag{1.10}$$

[1]The direct correspondence between the Laughlin wave function and Calogero-Sutherland model, especially in the comparison of the electron correlation functions of the two models, requires a more subtle argument than that presented here and is discussed at length in [39].

[2]The main focus of this work will be on CLLs of primary Quantum Hall Liquids, however the theory has been extended to more generic types FQHE states see, for example Ref. [38].

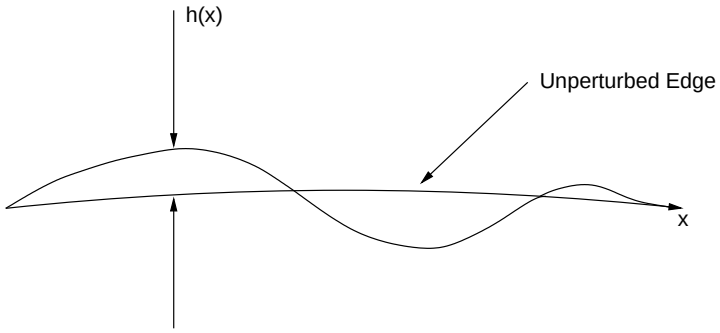

Figure 1.3: Surface wave formation at the boundary of an FQHE liquid: here $h(x)$ is the displacement of the edge of the liquid and x is the coordinate along the edge.

where $u = E/B$ is the propagation velocity of the wave and $\rho(x)$ is the density at the position x along the edge. The vertical displacement of the edge of the liquid is,

$$h(x) = n_d^{-1}\rho(x) = \frac{\rho(x)}{\nu D} \tag{1.11}$$

where, D as before is defined as the degeneracy of the LL per unit area. Finally, the Hamiltonian for the wave is given by,

$$H = \frac{e}{2}\int dx V(x)\rho(x) = \frac{\pi\hbar u}{\nu}\int dx \rho^2(x), \tag{1.12}$$

where $V(x) = Eh(x)$ is the linearized potential along the edge. The transformation of Eqs. (1.10) and (1.12) into momentum space gives

$$\dot{\rho}(k_n) = -iuq_n\rho(k_n), \tag{1.13}$$

$$H = \frac{hu}{\nu}\sum_{n=1}^{\infty}\rho(k_n)\rho(-k_n), \tag{1.14}$$

where we have used

$$\rho(x) = \frac{1}{\sqrt{L}}\sum_{n=1}^{\infty} e^{-ik_n x}\rho(k_n), \tag{1.15}$$

with L being the length of the edge and $k_n = 2\pi n/L$. In order to quantize the theory, it is necessary to compare Eqns. (1.13) and (1.14) with canonical

equations of motion for a coordinate $q(k_n)$ and momentum $p(k_n)$,

$$\dot{q}(k_n) = \frac{\partial H}{\partial p(k_n)} \tag{1.16}$$

$$-\dot{p}(k_n) = \frac{\partial H}{\partial q(k_n)}. \tag{1.17}$$

A comparison with (1.13) and (1.14) allows the identification $q(k_n) = \rho(k_n)$ and,

$$p(k_n) = \frac{ih}{\nu k_n}\rho(-k_n), \tag{1.18}$$

and finally to quantize we employ $[q(k_n), p(k_n)] = i\hbar$ which gives,

$$[\rho(k_n), \rho(-k_{n'})] = \frac{\nu q}{2\pi}\delta_{k_n,-k_{n'}}. \tag{1.19}$$

The above equation implies that the low energy gapless excitations of the edge states are bosonic in nature. The fermion field operators on an edge l can be defined through standard bosonization techniques as,

$$\tilde{\psi_l}(x,t) = \frac{1}{\sqrt{2\pi\alpha}}\xi_l e^{\frac{i}{\sqrt{\nu}}\phi_l(x,t)}. \tag{1.20}$$

which destroys an electron at a point x on edge l. The chiral boson fields ϕ_l describe edge fluctuations, $1/\alpha$ is the momentum cut-off of these fluctuations, and is related to the electron density at the edge: $\rho_l(x,t) = (\sqrt{\nu}/2\pi)\partial\phi_l(x,t)/\partial x$. The fields ϕ_l can be decomposed in the standard way into the individual "magneto-plasmon" oscillator modes

$$\phi_l(x,t) = \sum_{n=1}^{\infty}\frac{1}{\sqrt{n}}\left[a_n(t)e^{ik_n(x+i\alpha)} + H.c.\right]. \tag{1.21}$$

Another excitation supported by the edge states is given by the operator,

$$\psi_l(x,t) = \frac{1}{\sqrt{2\pi\alpha}}\tilde{\xi}_l e^{i\sqrt{\nu}\phi_l(x,t)}. \tag{1.22}$$

which destroys a quasiparticle of charge e^* at a point x on edge l. Here the "Klein factors" $\tilde{\xi}_l$ account for the mutual statistics of the quasiparticles on different edges. The operator defined in (1.22) destroys a particle of charge e^* at the position x. On the same edge, the quasiparticle operators satisfy the

exchange relations

$$\psi_l(x)\psi_l^\dagger(x') = e^{i\pi\nu\,\mathrm{sgn}(x-x')}\psi_l^\dagger(x')\psi_l(x), \tag{1.23}$$

which show that for $\nu = 1$ the quasiparticles are fermions while for $\nu = 1/(2n+1)$ and $n > 1$ the operators have anyonic exchange statistics.

One of the most interesting predictions of this theory concerns the unusual low temperature behavior of the tunnel density of states (DOS). Consider, for example, the DOS for *adding* a particle at a point x on the edge at energy E,

$$f_\nu(E) = \int_{-\infty}^{\infty} dt e^{-iEt/\hbar}\langle\psi(x,t)\psi^\dagger(x,0)\rangle, \tag{1.24}$$

where the correlator of the field operator at zero temperature is given by

$$\langle\psi(x,t)\psi^\dagger(x,0)\rangle = \langle\psi^\dagger(x,t)\psi(x,0)\rangle = \frac{1}{2\pi\alpha}\left(\frac{\alpha}{\alpha+iut}\right)^g. \tag{1.25}$$

The substitution of (1.25) into (1.24) reveals that $f_\nu(E) \sim E^{g-1}\theta(E)$. For electrons, $g = 1/\nu$, implies that the tunnel density of states vanishes as the energy lowers. This type of behavior in the DOS is one of the hallmarks of Luttinger liquids. Physically, this result is due to the existence of strong inter-particle correlations and creates a dynamic energy barrier for the addition or removal of particles. One avenue in which to experimentally probe the behavior of the DOS is through transport measurements. However, experiments to date [40–43] have shown some discrepancies between the theoretical predictions of the current and differential conductance (see, e.g. [44]) and observation. Overall, the experiments involving non-resonant tunnelling between $\nu = 1/3$ edge states [40–42], of primary interest in this work, seem to provide some evidence of CLL behavior in the edge states. On the other hand, for cases concerning resonant tunnelling [43, 45] and for filling factors other than $\nu = 1/3$ the evidence is more ambiguous.

1.1.2 Antidots

As mentioned earlier, a quantum antidot (QAD) is a small lithographically defined potential hill (or depletion region) formed in a 2DEG. The electric field from the potential acts in concert with the external magnetic field to trap quasiparticles into localized edge states that orbit about the antidot.

Quantitatively, the spectrum of these energy levels is quite complex even when assuming a simple model for the antidot potential [21, 46]. However, the general features of this spectrum can be understood by considering a smooth

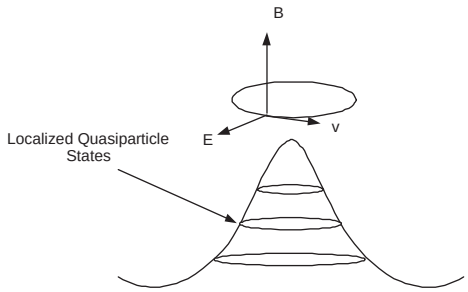

Figure 1.4: Schematic of a quantum antidot. The combination of the electric field, from the potential hill, and the magnetic field traps quasiparticles into localized edge states.

potential as a perturbation [21]. Taking the case of the lowest LL, the introduction of the QAD potential implies that the degeneracy of this state is broken and the LL is split into single particle states as illustrated in Fig. 1.4. From a semiclassical viewpoint [7, 21], the quantization of these bound states satisfies the Born-Sommerfeld quantization condition,

$$BS_m = m\phi_o, \tag{1.26}$$

where S_m is the area of the orbital. This condition implies that each state on the antidot encloses m flux quanta.

When the antidot is placed between two opposite edge states, it becomes possible to resonantly tunnel from one edge to the other through the localized states that exist on the antidot. Tunnelling between the edges and the antidot occur when the edge states are close enough to the antidot bound states such that quasiparticle backscattering is significant enough to cause a quasiparticle to be transferred between the two systems.

One application of resonant tunnelling in antidots is the Quantum Antidot Electrometer [7, 21, 22]. A schematic of such a setup is shown in Fig. 1.5. Here the edges are brought into the proximity of the antidot due to negatively biased gate electrodes which deplete the electron gas around them. Applying a bias to the system shifts the chemical potentials of the edges relative to the antidot states. In the low temperature limit, when the temperature is smaller than the energy splitting between consecutive states on the antidot, the quasiparticles can transit from one edge to another whenever the antidot state lies in between the chemical potentials of the edges. In this regime, the transport phenomena in occurring in antidots are very similar to those associated with the Coulomb blockade in tunnelling of individual electrons [47], despite the fact

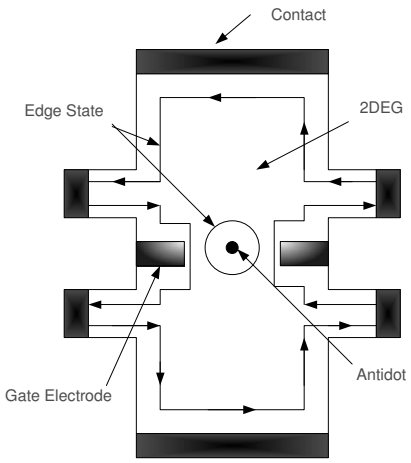

Figure 1.5: Schematic of the Quantum Antidot Electrometer. The edge state tunnelling in this device is controlled by negatively biased gate electrodes.

that the mechanism of quasiparticle localization on an antidot is microscopically quite different from the corresponding features of electron localization in quantum dots. For instance, in close analogy to the Coulomb-blockade oscillations of the conductance in a the quantum dot [48], the antidot exhibits periodic conductance oscillations with each period corresponding to addition of one quasiparticle to the antidot [7, 21–23]. The position of the energy levels of the antidot are controlled through a global back-gate potential. However, conductance oscillations can also be observed by changing the magnetic field. In this case, the position of the energy levels with changing magnetic field is modified so as to ensure that the quantization condition (1.26) is satisfied. By determining the period of the conductance oscillations as both a function of magnetic field and back gate voltage, it is possible to measure the charge of the quasiparticles.

1.2 Quantum Information

The field of Quantum Information (QI) deals with both the processing (Quantum Computation) and the extraction (Quantum Measurement) of information in quantum mechanical systems. The fundamental building block of any QI processing system is the qubit or quantum bit. Similarly to its classical counterpart the qubit consists of two computational basis states, $|0, 1\rangle$. The main difference between the classical and quantum versions of the bit lies in

the fact that the later can exist in a superposition of the two states, whereas the former can be in either one state *or* the other.

In Quantum Computation (QC), logical gate operations consist of unitary transformations on the qubit wave function. As first pointed out by Deutsch [49], the advantage that a Quantum Computer has over a classical one rests in its ability to exploit the inherit superposition of qubit states and act on these states all at once. This so-called *quantum parallelism* implies that for certain classes of problems, quantum computers will out perform classical computers [50]. Examples of these types include problems involving prime factorization and search [51–53].

One of the biggest obstacles to overcome in implementing any scheme of QC is the issue of environmentally induced decoherence. The entanglement of the qubit with some external environment causes a loss of phase coherence between the amplitudes of the qubit basis states. The result is a degradation of the quantum computer's overall performance. In reality, a complete isolation of a quantum system from the environment is impossible and thus decoherence is an ever present problem in QC applications. As such, one of the aims in developing a practical QC scheme is to minimize the effects of decoherence as much as possible. One such approach to achieving this is AQC [54–58], a topic which will be touched upon at the end of this section.

At the terminus of a quantum computation it is necessary to perform a measurement of the qubit system wave function. As is well known, any attempt to measure a quantum system necessarily disrupts it. The simplest model describing Quantum Measurement involves the process of wave function collapse [59, 60]. In this process, the state of the measured system is instantaneously localized into one of the basis states of the observed quantity. This inherently destroys any phase coherence that may exist between the wave function amplitudes of the measured system in other bases. Such a form of measurement is known as projective.

In a larger sense, the act of quantum measurement relays information about the state of the quantum system to the macroscopic world. Therefore, in order to extract information out of a quantum system it is necessary to entangle the system of interest with a macroscopic measurement device. Thus, the act of measuring a quantum system and obtaining information about the state of that system implies that the measured system will undergo decoherence which is caused by the coupling to the detector. This back-action dephasing is a necessary and unavoidable part of the measurement process.

In terms of the above discussion projective, or strong, measurements decohere the measured system instantaneously. On the opposite side of the spectrum are weak measurements. For this type of measurement the detector

is coupled only weakly to the measured system. The system is then continuously measured and information about its state is obtained via the detector gradually over time. Back-action dephasing due to the detector still takes place when utilizing a weak measurement scheme, however the resulting wave function collapse is not instantaneous. In this case, it makes sense to define a rate at which information about the states of the measured system is acquired by the detector. However, quantum mechanics places a limit on this information acquisition rate. The best one can do is retrieve information from the measured system at the same rate as the detector back-action destroys it. Such a measurement is known as quantum limited.

For the rest of this section, we discuss in more detail the various aspects of quantum information used in the thesis. Next, we will detail the use of the quantum antidot as a qubit. In Section 1.2.2 we examine in more detail quantum measurement, particularly in the context of mesoscopic devices. Finally, we will conclude with a brief introduction to AQC.

1.2.1 Quantum Antidots as Qubits

As mentioned at the beginning of this chapter, a practical way of implementing topological QC utilizing the anyonic exchange statistics of FQHE quasiparticles is via antidots [20]. The schematic of an FQHE qubit is illustrated in Fig. 1.6a. To form a qubit, two antidots are placed within close

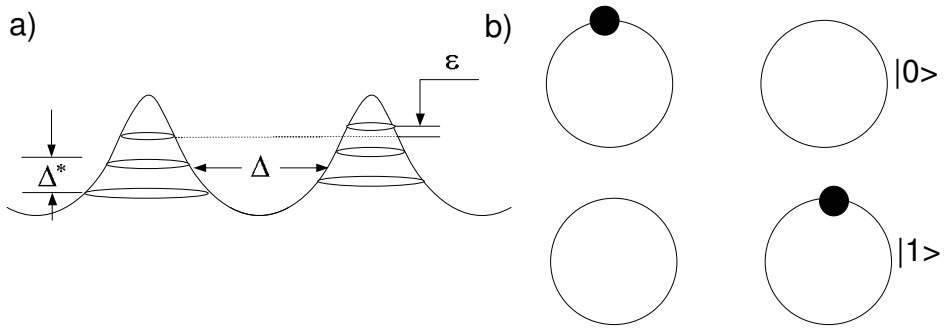

Figure 1.6: (a) An FQHE qubit consisting of two antidots with tunnel energy Δ, bias energy ϵ and energy gap between localized quasiparticle states Δ^*. (b) The basis states of this qubit correspond to a quasiparticle being localized on one antidot or the other.

proximity to one another to allow quasiparticle tunnelling between them. It

is assumed that the largest energy scale in the system is the energy gap Δ^* between the localized quasiparticle states on the antidots which is also less than the quasiparticle excitation gap. This assumption means that the qubit basis states are defined by a quasiparticle localized on one antidot or the other, as shown in Fig. 1.6b.

In order to perform gate operations with this type of qubit, one exploits the anyonic nature of the quasiparticles whereby exchanging quasiparticles translates into unitary transformations of the qubit wave function. To do this requires an array of multiple antidots with quasiparticles being transferred from one antidot to another adiabatically. For example, in the case shown in Fig. 1.6a, quasiparticle transfer between the antidots is accomplished by changing the gate bias ϵ so that the time rate of change $\dot{\epsilon}$ is much smaller than the energy gap between the eigenstates of the system.

However, as with any type of qubit there are always sources of decoherence. In the particular case of FQHE qubits, decoherence stems from two different mechanisms. One the one hand, Coulomb interaction between the localized charge hopping between the antidots and the gate electrodes causes energy dissipation due to the finite resistance of the metallic electrodes. One the other, the charge on the antidot is coupled via Coulomb interaction to the density fluctuations from the edge state. Such types of interactions are described by a Hamiltonian of the form shown in (1.12). Qualitatively, decoherence via the edge states is caused by dissipation through the chiral plasmon modes, see Eq. (1.21). This is similar to decoherence described by the well known spin-boson model (see e.g. [61]). We will discuss this point in more detail in the next Chapter.

1.2.2 Mesoscopic Measurements

The term mesoscopic refers to systems that have particle numbers and length scales which are somewhere in between the microscopic and the more familiar macroscopic world. The advent of solid state quantum information processing has motivated studies into mesoscopic structures for use as both measurement devices (detectors) and qubits. Particular examples of mesoscopic detectors include, Quantum Point Contacts [62, 63], Single Electron Transistors (SETs) [64, 65], superconducting SETs [27], and dc-SQUIDs [27, 66] to name but a few.

Given the multitude of mesoscopic detectors available, it is helpful to have a means by which to assess their measurement characteristics. Within the context of continuous weak measurements such an assessment is possible [26, 27, 67]. In the case where the detector is measuring a qubit, a generic

description of the combined system is given by the Hamiltonian,

$$H = H_d + H_q + CQ\sigma_z \tag{1.27}$$

where, $H_{d,q}$ are the Hamiltonians of the detector and qubit, respectively. The last term describes the coupling of the two systems with coupling strength C. Here, Q is some quantity associated with the detector. For example, in the case of an SET detector this might represent the amount of excess charge on the island. If the coupling strength between the two systems is weak enough and the detector remains in a stationary state, the output of the detector I (again, in the case of a SET, this would represent the tunnelling current) is only slightly perturbed by the coupling to the qubit. So, to first order in the coupling, the detector output is given by

$$\langle I \rangle = I_o + C\lambda\langle\sigma_z\rangle, \tag{1.28}$$

where $I_o = \mathrm{Tr}[I\rho_o]$ is the output of the detector in the absence of the qubit and ρ_o is the stationary density matrix of the detector. Similarly, $\langle\sigma_z\rangle = \mathrm{Tr}[\sigma_z\rho_q]$ where ρ_q represents the qubit's density matrix. Finally, the quantity, λ is known as the linear response coefficient and is given by,

$$\lambda = \frac{4\pi}{\hbar}\,\mathrm{Im}\,S_{IQ}, \tag{1.29}$$

where,

$$S_{IQ} = \frac{1}{2\pi}\int d\tau\Theta(\tau)\langle I(0)Q(\tau)\rangle, \tag{1.30}$$

represents the cross-correlation between the input and output of the detector. Note that $\langle ...\rangle = \mathrm{Tr}[...\rho_o]$ and the time dependence of the both quantities is governed by the detector Hamiltonian in (1.27). In deriving this, it was assumed that the response time of the detector is much faster than the dynamics of the qubit [26, 27, 67]. The meaning behind Eq. (1.28) is that the detector acts as a linear amplifier. In other words, the relatively small signal associated with the qubit is taken in at the input Q of the amplifier and then transferred to the output having been multiplied by a gain $C\lambda$.

In order to characterize the measurement efficiency of the detector it is necessary to take into account its noise properties. First, consider the fluctuations of the detector input Q. For weak detector-qubit coupling the fluctuations in Q cause the suppression of the phase coherence between the basis state amplitudes of the qubit. This decoherence rate can be found via lowest-order

perturbation theory in the detector-qubit coupling,

$$\Gamma_d = \frac{\pi C^2}{\hbar^2} S_Q, \tag{1.31}$$

where

$$S_Q = \frac{1}{2\pi} \int d\tau \langle \delta Q(\tau) \delta Q(0) \rangle \tag{1.32}$$

is the zero frequency spectral density of the noise associated with Q and $\delta Q(t) = Q(t) - \langle Q \rangle$. Thus, Eq. (1.31) represents the back-action dephasing of the detector on the qubit. The assumption of instantaneous detector response implies that the amplifier's input noise is effectively δ-correlated [26, 27] meaning that its spectral density is white.

The other quantity needed for understanding of the measurement process is the measurement time of the detector. As one can see by inspection of Eq. (1.28), the detector produces two different output currents depending on the state of the qubit which differ by $\Delta I = 2C\lambda$. In the presence of noise, a finite time is required to distinguish between these states. This is given by,

$$\tau_m = \frac{8\pi S_I}{C^2 \lambda^2}, \tag{1.33}$$

where, S_I is the same as Eq. (1.32) with Q replaced by I and represents the detectors output noise. As was mentioned earlier, quantum mechanics sets a definite restriction on the rate at which information is extracted from the qubit versus the rate with which the system's coherence is destroyed. Since for low frequencies all of the noise spectra discussed above are constant, one can obtain the inequality, $S_I S_Q \geq |S_{IQ}|$ [26, 27] which implies,

$$2\tau_m \Gamma_d \geq 1. \tag{1.34}$$

The meaning of this inequality is that the best one can do, when weakly measuring a quantum system, is to extract information at the same rate as the coherence is destroyed by the back-action dephasing of the detector. Another figure of merit for gauging the efficiency of quantum detectors is the energy sensitivity [26, 27], which is given by

$$\varepsilon = \frac{4\pi}{|\hbar\lambda|} \left[S_I S_Q - (\mathrm{Re}\, S_{IQ})^2 \right]^{1/2}. \tag{1.35}$$

Employing the Schwartz Inequality once again means that $\varepsilon \geq \hbar/2$. Such detectors in which $2\tau_m \Gamma_d = 1$ are known as ideal or quantum limited. Equality in the relation (1.34) also implies that the energy sensitive is equal to $\hbar/2$. In

this case, the detector does not add anymore dephasing to the qubit than is required to extract information from the system.

1.2.3 Adiabatic Quantum Computation

Adiabatic Quantum Computation [54–58] offers the possibility of reducing the effects of decoherence by performing computations in the ground state of a system of qubits. As suggested by its name, AQC relies heavily on the adiabatic evolution of a quantum system in order to keep the system as much as possible in its ground state during the overall time of the computation. The main advantage of this scheme is that if the energy gap between the ground and first excited state is large enough it provides some measure of protection against decoherence.

This ground-state evolution is a consequence of the slow evolution of the Hamiltonian. The question is what are the conditions under which this can occur? The answer is provided by the Adiabatic Theorem [68]. Let $H(t)$ be some time dependent Hamiltonian. Next, assume that the Hamiltonian varies over some time interval $t \in [t_i, t_f]$ and a definite energy gap, $E_1(t) - E_0(t)$, exists between the instantaneous ground state energy $E_0(t)$ and the first excited state $E_1(t)$. The condition for adiabatic evolution, that the transition probability between the two states is small, is then given by [68]

$$g_m^2 \gg \max_{t_i \le t \le t_f} \langle \psi_1(t) | \frac{\partial H}{\partial t} | \psi_0(t) \rangle \qquad g_m = \min_{t_i \le t \le t_f} [E_1(t) - E_0(t)] \tag{1.36}$$

where $\psi_{0,1}(t)$ are the instantaneous ground and first excited eigenstates of $H(t)$ and we have set $\hbar = 1$. This condition can be understood as follows. Imagine transforming $H(t)$ into the basis of its instantaneous eigenstates $|\psi_k(t)\rangle$, where k is an index that labels the states. The result is that the Hamiltonian will consist of two parts, a diagonal matrix consisting of the energies $E_k(t)$ plus an additional term that generates transitions between different states. In the case of the two lowest-lying energy states, the condition (1.36) means that if the system is prepared in the ground state $\psi_0(t)$, then over the entire time interval the transitions to the excited state are negligible.

The implementation of AQC begins by specifying an initial Hamiltonian, H_i and preparing the system in its ground state $|\psi(t_i)\rangle$ at some initial time t_i. Next, the system is evolved in time until $t = t_f$ according to the Hamiltonian,

$$H(t) = [1 - s(t)]H_i + s(t)H_f \tag{1.37}$$

where $s(t)$ vanishes at $t = t_i$ and is equal to 1 when $t = t_f$. Thus, $H(t)$ interpo-

lates between the initial Hamiltonian and the final H_f which is chosen in such a way that its ground state $|\psi(t_f)\rangle$ represents the solution to the computational problem. A successful result implies that the evolution is done slow enough that $H(t)$ remains as close as possible to its ground state throughout the entire evolution, that is, the condition (1.36) is met. Here, quantum computation is performed through the unitary evolution of the ground state wave function. Due to the ground state evolution of AQC it is expected that this scheme of QC provides a measure of protection against environmental decoherence. In Chapter 7 of this thesis, we study its stability with respect to decoherence induced by low frequency noise.

Part I

Antidot Transport

Chapter 2

Correlated FQHE quasiparticle transport in a double-antidot system

The focus of the chapter is to explore quasiparticle transport in a system consisting of two tunnel coupled antidots. Since Quantum antidots formed in a 2D electron system offer a possibility of localizing and controlling the transport of individual quasiparticles [7, 21–23], such control made possible the first direct observation of the fractional quasiparticle charge in tunnelling through an antidot [7, 21]. This observation was later extended to the regime of ballistic quasiparticle transport [8, 9, 69]. The goal of the work [70] presented in this chapter is to develop a theory of correlated quasiparticle transport in a double-antidot system. As pointed out in Chapter 1, the double-antidot system was discussed previously [20] as a qubit, information in which is encoded by individual quasiparticles. Such qubit is similar to superconducting charge qubits [71–73] which are based on the dynamics of individual Cooper pairs. As in the case of Cooper pairs [74, 75], the transport measurements on the quasiparticle qubit can be done more easily than direct measurements of the qubit dynamics. Transport measurements would constitute the first step towards experimental development of the FQHE qubits. More generally, understanding the transport properties of multi-antidot systems, in particular the role of Coulomb interaction for localization of individual quasiparticles, and the significance of the edge-state decoherence, should also be important for other, more complicated types of suggested FQHE qubits [76, 77] which also require control over individual quasiparticles.

In the next section we will begin with a discussion of the model for a double antidot system including transport between the edges and the antidot. Included in this section will be a detailed discussion of the effects of deco-

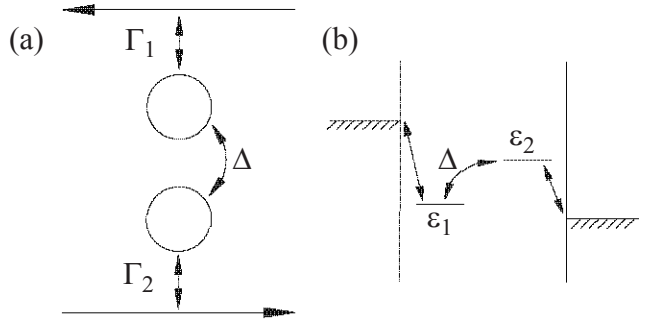

Figure 2.1: Quasiparticle tunnelling in the double-antidot system: (a) the real-space geometry (not to scale) of quasiparticle transfer between the opposite edges of the FQHE liquid; (b) energy diagram of the transfer.

herence induced by the edge states on quasiparticle transport between the antidots. The remainder of the chapter is dedicated to calculating the tunnel rates and conductance of the system in the limits of both strong and weak edge state induced decoherence.

2.1 Model

The system we consider consists of two antidots in series between two opposite edges of a primary quantum Hall liquid with the filling factor $\nu = 1/(2m+1)$ (Fig. 2.1a). The antidots are tunnel-coupled to each other and to the edges, which play the role of quasiparticle reservoirs. The quasiparticle current through the antidots is driven by the transport voltage V applied between the edges. The focus of this work is on the regime when all relevant energies are smaller than the energy gap Δ^* of the antidots (see below), and the transport can be described completely in terms of the transfer of individual quasiparticles. This regime is relevant, e.g., for the operation of this system as a qubit. The main elements of the model of the double-antidot system in this case can be outlined as follows.

2.1.1 Antidots

An antidot formed at a point ζ in a primary quantum Hall liquid with the filling factor $\nu = 1/(2m+1)$ can be described as a collection of n quasi-hole excitations created at this point. Microscopically, the unnormalized wave

function of this configuration is [3, 4]:

$$\psi(\{z_j\}) = \prod_j (z_j - \zeta)^n \psi_m(\{z_j\}) \,, \tag{2.1}$$

where $\psi_m(\{z_j\})$ is Laughlin's wave function, given in Eq. (1.2), of the unperturbed quantum Hall liquid and, in the standard notations, the antidot position ζ in the two-dimensional plane and the electron. The number n of the quasiholes is related to the geometric radius R of the antidot: $R \simeq \sqrt{2n}\ell$, where ℓ is the magnetic length.

In what follows, we make use only of the general qualitative features of the wave function (2.1). For instance, in agreement with the typical experimental situation (see, e.g., [7, 21]), we assume that the antidot is relatively large: $n \gg 1$. This means that addition or removal of individual quasiparticles (here and below, this term will be used to describe processes with varying n: $n \to n \pm 1$), does not change the antidot parameters noticeably. Indeed, the variation of the antidot radius in this case is $\delta R \propto \ell/\sqrt{n}$ and is small not only on the scale of R, but, more importantly, on the scale of the magnetic length ℓ.

The general form of the antidot energy E_n as a function of n is determined by the interplay of Coulomb interaction and an external potential used to create the antidot. However, for large n, and in some small range of variation of n around the minimum of E_n, one can always approximate this dependence as quadratic. This defines the characteristic energy gap $\Delta^* \equiv \partial^2 E_n/\partial n^2$ which gives the energy interval of variation of the chemical potential μ of the system between the successive additions of individual quasiparticles to the antidot. For the system shown in Fig. 2.1a, the antidots exchange quasiparticles with the edges, and μ is defined by the edge chemical potential. In the situation of the antidot, when all the energies are dominated by the Coulomb repulsion, the energy gap Δ^* for changing the number of quasiparticles is approximately related to the energy gap for the antidot excitations at fixed n: $\Delta^* \simeq \hbar u/2\pi R$, where u is the velocity of the excitations encircling the antidot. In general, e.g. in the case of quantum dots, the two types of energy gaps can be very different.

We assume that the gap Δ^* is sufficiently large for both antidots of the double-antidot system, so that in the reasonably large range of variation of μ both antidots are characterized by some well-defined numbers n_l, $l = 1, 2$, of the quasiparticles. In this regime, the non-vanishing conductance of the double-antidot system requires that μ is close to resonances in the both antidots. At resonance, $E_{n_l} \simeq E_{n_l+1}$, and each antidot can in principle be in one of two states which differ by the presence or absence of one "extra" quasiparti-

cle. The resulting four double-antidot states are relevant for the quasiparticle transport. We will use the notation for these states that gives the number of extra quasiparticles on each antidot

$$|ij\rangle \equiv |n_1 + i, n_2 + j\rangle\,, \quad i, j = 0, 1\,, \tag{2.2}$$

and talk about the "first" and the "second" quasiparticle on the antidots disregarding the background n_l quasiparticles. Counting the antidot energies E_n from the energy of the state with no extra quasiparticles, we can parameterize the energies ϵ_{ij} of the four states as

$$\epsilon_{00} = 0\,, \quad \epsilon_{11} = 2\epsilon + U\,, \quad \epsilon_{10} = \epsilon - \delta\,, \quad \epsilon_{01} = \epsilon + \delta\,. \tag{2.3}$$

Here U is the interaction energy between the extra quasiparticles on the two antidots while ϵ and δ give the energies ϵ_l (Fig. 2.1b) of the single-quasiparticle states localized at the two antidots, $\varepsilon_{1,2} = \epsilon \mp \delta$. The energies ϵ and δ are defined relative to the common chemical potential of the edges for vanishing bias voltage V between them. A non-vanishing bias voltage shifts the energies (2.3). Experimentally, the antidot energies are controlled by the back-gate voltage or magnetic field [7, 21, 22]. The degree to which these fields couple to the energy difference δ depends on the degree of asymmetry between the two antidots. In the following, we present the results for quasiparticle conductance of the system as a function of ϵ for fixed δ, as would be appropriate for identical antidots. These results can be generalized to non-identical antidots by taking a "cross-section" in the space of ϵ and δ along the direction appropriate for a given degree of the antidot asymmetry.

If the two antidots are sufficiently close, so that the distance between their edges is on the order of magnetic length ℓ, the quasiparticle states localized around them overlap and hybridize. This effect can be accounted for by the tunnel coupling $-\Delta$ of the antidots. The phases of the antidot states can always be chosen to make Δ real. This coupling affects only the singly-occupied states $|10\rangle$ and $|01\rangle$. The single-quasiparticle part of the Hamiltonian is then:

$$H = \epsilon - \delta\sigma_z - \Delta\sigma_x\,, \tag{2.4}$$

where σ's are the Pauli matrices. Equation (2.4), together with the part of Eq. (2.3) describing states with zero and two quasiparticles, gives the main part of the antidot energy controlling the quasiparticle transport. In what follows, we assume that all contributions to this energy and the temperature T are small;

$$\Delta, \varepsilon_l, U, T \ll \Delta^*. \tag{2.5}$$

In this regime, tunnelling through the antidots can be discussed in terms of correlated transfer of individual quasiparticles. Since the gap, Δ^*, is dominated by Coulomb interaction, i.e. has the same origin as the quasiparticle interaction energy U, the most restrictive part of the assumption (2.5) is the condition on U. This condition can still be satisfied due to the difference between stronger quasiparticle repulsion on the same site and weaker repulsion on different sites.

2.1.2 Antidot-edge tunnelling

Similarly to the tunnel coupling between the antidots, if the edges of the FQHE liquid are not far from the antidots on the scale of the magnetic length ℓ, there is a non-vanishing amplitude for quasiparticle tunnelling between the edge and the nearest antidot. The tunnelling between the lth edge and antidot can be described quantitatively with the standard tunnel Hamiltonian

$$H_T^{(l)} = T_l \psi_l^\dagger \xi_l + h.c.\,, \tag{2.6}$$

where $\psi, \psi^\dagger$ and $\xi, \xi^\dagger$ are the creation/ahhihalation operators for quasiparticles at, respectively, the edges and the antidots. Denoting the position along the edge as x and taking the tunnelling points for both edges to be at $x = 0$, the edge quasiparticle operators ψ_l can be expressed in the standard bosonisation approach as [34]

$$\psi_l(t) = (1/2\pi\alpha)^{1/2} \tilde{\xi}_l e^{i\sqrt{\nu}\phi_l(0,t)}\,. \tag{2.7}$$

Here the "Klein factors" $\tilde{\xi}_l$ account for the mutual statistics of the quasiparticles in different edges, ϕ_l are the chiral bosonic fields which describe the edge fluctuations propagating with velocity u, and $1/\alpha$ is their momentum cut-off as given in Eq. (1.21). The edge fluctuations result in the fluctuations of electron density at the edge: $\rho_l(x,t) = (\sqrt{\nu}/2\pi)\partial\phi_l(x,t)/\partial x$. For our approach, we limit this discussion to a perturbative treatment of the antidot-edge tunnelling (2.6). In this case, the statistical Klein factors in (2.7) for the edge operators would cancel out in the perturbation expansion and can be omitted.

The quasiparticles at the antidots should be described in general by the expressions similar to Eq. (2.7). The condition (2.5) of the large antidot energy gap Δ^* ensures, however, that the fluctuations of the edges around the antidots are suppressed, i.e. the magneto-plasmon oscillations are not excited out of their ground state $|0\rangle$. In this regime of the "quantized" edge, the general quasiparticle operators (2.7) reduce to just the statistical Klein factors up to a normalization constant. Indeed, as one can see directly from Eq. (1.21) by

bringing the ϕ-part of (2.7) into the normal form,

$$\langle 0|e^{i\sqrt{\nu}\phi}|0\rangle/(2\pi\alpha)^{1/2} = (\pi R)^{-1/2}\,. \tag{2.8}$$

Including this normalization constant in the tunnel amplitude T_l, we see that the operators ξ_l for quasiparticles at the antidots consist solely of the Klein factors. The appropriate set of properties of the quasiparticle Klein factors ξ depends on the specific geometry of each edge-state tunnelling problem. Non-trivial examples of this can be found in [78–83]. As follows from the discussion in the preceding Section, in tunnelling between the quantum antidots, the operators ξ_l should account for the "hardcore" property of the quasiparticles; in the given range of external parameters only one extra quasiparticle can occupy one antidot. In general, these operators should also describe the anyonic exchange statistics of the FQHE quasiparticles [84], but the geometry of the double-antidot system (Fig. 2.1a) does not permit quasiparticle exchanges, and the exchange statistics of the tunnelling particles is irrelevant. Since the hardcore property makes the quasiparticle occupation factors equivalent to those of the fermions, and the actual exchange statistics is irrelevant, the antidot quasiparticle operators $\xi, \xi^\dagger$ can be treated as fermions. Together with Eqs. (2.7) and (1.21) for the edge quasiparticles, this defines completely the tunnel Hamiltonian (2.6).

2.1.3 Edge-state decoherence

Tunnelling of charged quasiparticles through the antidot system couples to all gapless charged excitations that exist in the system. In the case of the FQHE liquid, excitations in the bulk of the liquid are suppressed by the energy gap, and only the edges support gapless excitations. In contrast to all other possible mechanisms of decoherence (e.g., plasmons in metallic gates, or charged impurities in the substrate) the edges play the role of reservoirs in transport measurements and as a matter of principle can not be removed from the antidots. In this Section, we estimate the strength of this unavoidable edge-state decoherence for quasiparticle tunnelling through the double-antidot system.

The spectrum of the gapless edge excitations of one edge consists of magnetoplasmon oscillations (1.21) with the Hamiltonian:

$$H_0 = (hu/L)\sum_{n=1}^{\infty} n a_n^\dagger a_n\,. \tag{2.9}$$

We assume that the antidot system is symmetric, and a quasiparticle sitting on

the first antidot creates a potential $V_l(x)$ along the lth edge. The quasiparticle dynamics governed by the Hamiltonian (2.4) is coupled then to the fluctuations of electron densities $\rho_l(x)$ at the edges through the interaction Hamiltonian

$$H_{int} = \frac{1}{2}\sigma_z e \int dx V(x)(\rho_1(x) - \rho_2(x))\,, \tag{2.10}$$

where $V(x) = V_1(x) - V_2(x)$ is the change of the potential along the edges due to quasiparticle transfer between the antidots. Since the edge-antidot distance and the distance between the antidots are on the order of antidot radius R, this radius sets the range of the potential $V(x)$. The edge velocity u can be expected to be similar for the external edges and the antidots. This means that the condition (2.5) of the large energy gap implies that the characteristic wavelength of the edge excitations which can exchange energy with the quasiparticles on the antidots is much larger than the range of the potential $V(x)$: $\hbar u/\epsilon \gg \hbar u/\Delta^* \simeq R$. The interaction energy (2.10) can be expressed then as

$$H_{int} = \frac{e}{2}\sigma_z(\rho_1(0) - \rho_2(0)) \int dx V(x)\,, \tag{2.11}$$

where, as follows from Eq. (1.21), the densities ρ_l are

$$\rho_l(0) = \frac{i\sqrt{\nu}}{L}\sum_{n=1}^{\infty}\sqrt{n}(a_n - a_n^\dagger)\,. \tag{2.12}$$

The strength of interaction (2.11) can be characterized by the typical transition rate Γ_d between the eigenstates of the antidot Hamiltonian (2.4) induced by the edges. Straightforward calculation of the "Golden-rule" rate using Eqs. (2.9), (2.11), and (2.12) gives:

$$\Gamma_d = \frac{\nu^3}{4\pi\hbar}\alpha^2\kappa^2|\langle\sigma_z\rangle|^2\frac{\Delta E}{1 - e^{-\Delta E/T}}\,, \tag{2.13}$$

where ΔE is the energy difference between the two states, $\langle\sigma_z\rangle$ is the matrix element of σ_z between them. The dimensionless factor κ characterizes the overall "intensity" of the antidot-edge potential,

$$\kappa \equiv \left(\frac{\nu e}{4\pi\varepsilon\varepsilon_0}\right)^{-1}\int dx V(x)\,. \tag{2.14}$$

The precise form of the potential $V(x)$ and the value of κ depend on the details of configuration of the metallic gates that define the edges and screen

the antidot-edge interaction. However, normalized as in Eq. (2.14), κ should be on the order of 1. For instance, assuming as a crude model of the system electrostatics that the antidot-edge interaction is confined to the interval $d \simeq 2R$ in which the edge is a tunnel-limited distance ℓ away from the antidot, one can estimate κ as $(2/\pi)\ln(2R/\ell)$, i.e., $\kappa \simeq 2$ for realistic $R/\ell \simeq 10$.

The factor α in (2.13) is the "fine structure constant" of the edge excitations,

$$\alpha \equiv \frac{e^2}{4\pi\varepsilon\varepsilon_0\hbar u}\,, \tag{2.15}$$

and is the main parameter controlling the strength of decoherence Γ_d through the velocity u of the edge excitations. The dielectric constant ε is fixed by the material (GaAs) of the structure, $\varepsilon \simeq 10$, and in the realistic range of possible velocities u, $10^4 \div 10^5$ m/s [22], α should vary in the range between 2 and 20. In the most relevant case of the FQHE liquid with the filling factor $\nu = 1/3$, and for the edge-antidot coupling intensity estimated above, the quality factor $\Delta E/\hbar\Gamma_d$ of the quasiparticle dynamics changes then roughly between 0.1 and 10. This means that in the case of strong edge confinement that produces large velocity u, the quasiparticle dynamics on the antidots can be quantum-coherent provided that all other decoherence mechanisms are sufficiently weak. In the opposite case of smooth confinement with low velocity u, the already unavoidable edge-state decoherence is strong enough to completely suppress the coherence of the quasiparticle states on different antidots, and quasiparticle transfer processes between them are incoherent.

2.2 Tunnelling rates

As was mentioned above, the discussion in this work is limited to the regime in which the transport through the double-antidot system can be interpreted as the correlated transfer of individual quasiparticles. Besides the condition (2.5) on antidot energies, this also requires that the antidots are coupled only weakly to the edges, so that the edge-antidot tunnelling can be treated as a perturbation leading to an incoherent transfer of individual quasiparticles. The quasiparticle transport through the antidots is governed then by the kinetic equation similar to that for Coulomb-blockade transport in quantum dots with discrete energy spectrum [85–87]. This Section calculates the relevant tunnelling rates in the two limits of strong and weak edge-state decoherence.

2.2.1 Strong decoherence

If the edge-state decoherence is sufficiently strong, the quasiparticle transfer between the antidots can be treated as incoherent and described by the sequential tunnelling rate obtained by perturbation theory in the tunnel amplitude Δ. To calculate this rate, it is convenient to express the density operators ρ_l of the two edges through one effective density ρ which satisfies the same relation (2.12): $\rho_1(0)-\rho_2(0) = \sqrt{2}\rho(0)$, so that the edge-antidot coupling (2.11) is:

$$H_{int} = \hbar u\, \nu \frac{\kappa\alpha}{\sqrt{2}}\, \rho(0)\, \sigma_z\,. \tag{2.16}$$

Next, one can perform a unitary transformation which converts the fluctuations of the energy of the quasiparticle basis states $|10\rangle\,, |01\rangle$ induced by (2.16) into a fluctuating phase of the tunnelling matrix elements of the tunnelling part of the Hamiltonian (2.4),

$$-\Delta\sigma_x \;\; \rightarrow -\Delta \sum_{\pm} \sigma_{\pm} e^{\pm i\sqrt{g}\phi(0,t)}, \quad g = \frac{\nu^3\kappa^2\alpha^2}{2\pi^2}\,, \tag{2.17}$$

where $\phi(x,t)$ is the bosonic field given by same the Eq. (1.21). Then, the rate Γ_Δ of the *anidot-antidot* tunnelling can be expressed in the lowest non-vanishing order in the amplitude Δ as:

$$\Gamma_\Delta = 2\Delta^2 \mathrm{Re} \int_{-\infty}^{0} dt e^{iEt} \langle e^{i\sqrt{g}\phi(0,t)} e^{-i\sqrt{g}\phi(0,0)} \rangle\,, \tag{2.18}$$

where $\langle ... \rangle$ is the average over the equilibrium fluctuations of ϕ and $E = \pm 2\delta$ is the energy difference (depending on the direction of tunnelling) between the quasiparticle states localized on the antidots. The standard evaluation of Eq. (2.18) (see, e.g., [88, 89]) gives,

$$\Gamma_\Delta(E) = \gamma f_g(E)\,, \quad \gamma \equiv 2\pi\Delta^2/\omega_c\,, \tag{2.19}$$

$$f_g(E) \equiv \frac{1}{2\pi\Gamma(g)} (2\pi T/\omega_c)^{g-1} \left|\Gamma(g/2 + iE/2\pi T)\right|^2 e^{-E/2T}\,,$$

where $\Gamma(z)$ is the gamma-function and $\omega_c = \hbar u/2\alpha$ is the cut-off energy of the edge excitations. The function $f_g(E)$ gives the energy dependence of the tunnelling rate (see Fig. 2.2) and is defined to coincide with the Fermi distribution function for $g = 1$. The power g determines the behavior of the transition rate at large energies $|E| \gg T$: $\Gamma_\Delta(E) \propto E^{(g-1)}$ on the "allowed" side of the transition ($E < 0$), and $\Gamma_\Delta(E) \propto E^{(g-1)} e^{-E/T}$ on the "forbidden"

side ($E > 0$), when the transition has to overcome the energy barrier E. This asymptotic behavior of the tunnelling rates, together with Eq. (2.19), is valid at $|E| \ll \omega_c$.

The rates Γ_l, $l = 1, 2$, of the *antidot-edge* tunnelling are obtained through a similar calculation starting with the tunnel Hamiltonian (2.6). They are given by the same expression (2.19):

$$\Gamma_l(E) = \gamma_l f_\nu(E)\,, \quad \gamma_l \equiv 2\pi|T_l|^2/\omega_c\,. \tag{2.20}$$

In general, the long-range Coulomb interaction should generate corrections to g which move it away from the "quantized" value $g = \nu$ [90–92]. However, in contrast to the quasiparticle tunnelling between the antidots, which is changed qualitatively by decoherence created by the Coulomb interaction with the edge, the Coulomb corrections for the antidot-edge tunnelling are expected to be small and will be neglected in this work.

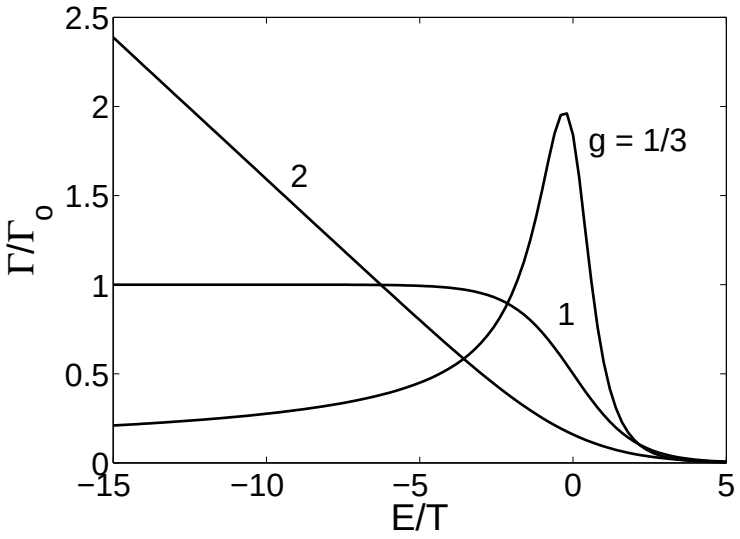

Figure 2.2: Energy dependence of the antidot-antidot (2.19) and antidot-edge (2.20) tunnelling rates. The normalization factor is $\Gamma_0 = \gamma(2\pi T/\omega_c)^{g-1}$.

Thus, in the regime of strong edge-state decoherence, the overall transport of quasiparticles through the double-antidot system can be described as a combination of successive antidot-edge transitions (2.20) and incoherent transitions (2.19) between the antidots.

2.2.2 Weak decoherence

For sufficiently strong edge-state confinement, the edge-induced relaxation rate (2.13) will be smaller than the antidot energies. If other decoherence mechanisms, including the decoherence created by incoherent antidot-edge tunnelling are also weak on the scale of the antidot energies,

$$\Gamma_d, \Gamma_l \ll \Delta, \delta, U, T, \tag{2.21}$$

the quasiparticle dynamics on the antidots is quantum-coherent. It is characterized by the stationary eigenstates $|k\rangle$, $k = 1, 2$, of the double-antidot Hamiltonian (2.4):

$$H|k\rangle = (\epsilon + (-1)^k \Omega)|k\rangle, \;\; \Omega \equiv (\delta^2 + \Delta^2)^{1/2},$$

$$|k\rangle = c_{1k}|10\rangle + c_{2k}|01\rangle, \tag{2.22}$$

for which the probabilities λ_{lk} of finding the quasiparticle on the lth antidot are:

$$\lambda_{lk} = |c_{lk}|^2 = [1 + (-1)^{l+k}\delta/\Omega]/2\,. \tag{2.23}$$

In the coherent regime (2.21), the double-antidot system can be viewed as a quasiparticle qubit [20]. The current through the qubit is described in terms of tunnelling to/from the eigenstates (2.22). The corresponding tunnelling rates are found from the tunnel Hamiltonian (2.6), in which, as was discussed in Sec. 2.1.2, the quasiparticle creation/annihalation operators $\xi, \xi^\dagger$ act as fermions. This means that the tunnel matrix elements for the quasiparticles can be calculated in the standard way. In particular, for each eigenstate (2.22), the matrix element is independent of the occupation factor of the other eigenstate. Explicitly, the tunnelling rate Γ_{lk} from the lth edge into the state $|k\rangle$ is

$$\Gamma_{lk} = 2|T_l|^2 |\langle k|\xi_l^\dagger|0\rangle|^2 \mathrm{Re} \int_{-\infty}^{0} dt e^{iEt} \langle \psi_l^\dagger(t)\psi_l(0)\rangle\,. \tag{2.24}$$

Here $|0\rangle$ denotes the empty eigenstate and E is the appropriate tunnelling energy which includes in general the eigenenergies (2.22) and the interaction energy U. The quasiparticle matrix elements are $|\langle k|\xi_l^\dagger|0\rangle|^2 = \lambda_{lk}$, and thus,

$$\Gamma_{lk}(E) = \lambda_{lk}\Gamma_l(E), \tag{2.25}$$

where the rates $\Gamma_l(E)$ are given by Eq. (2.20). In the practically important case of FQHE liquid with $\nu = 1/3$, the energy dependence of the transition rates (2.25) is illustrated by the $g = 1/3$ curve in Fig. 2.2. The peak of the tunnelling rate at $\epsilon \simeq 0$ is the consequence of the Luttinger-liquid correlations

of the edge quasiparticles. Conductance calculations presented in the next Section show that this peak manifests itself as additional resonant features of the qubit conductance.

2.3 Conductance of the double-antidot system

In both situations of strong and weak decoherence, the conductance associated with tunnelling of individual quasiparticles through the double-antidot system can be calculated by solving the kinetic equation for quasiparticle occupation probabilities of the antidot states. Similarly to the case of tunnelling through one antidot [7, 21–25], the conductance as a function of the common energy ϵ of the antidot states should exhibit the resonant tunnelling peaks. For the double-antidot system, the peak structure is, however, more complicated, reflecting the transition between the low-temperature regime in which each peak corresponds to addition of one quasiparticle to the system of antidots, and a possible "large-temperature" regime, when the single-quasiparticle peaks are merged, and each conductance peak is associated with addition of two quasiparticles. In this Section, we calculate the corresponding conductance line shapes. Quantitatively, these line shapes are determined by the interplay between the quasiparticle repulsion energy U on the two antidots and tunnel coupling Δ between them. The calculations below are focused mostly on the more typical case of large repulsion energy $U \gg \Delta \simeq \delta$.

2.3.1 Strong decoherence

For strong edge-state decoherence, coherent mixing of the quasiparticle states on the two antidots is suppressed, and the quasiparticle dynamics is described by kinetic equations for the occupation probabilities p_{ij} of the states $|ij\rangle$ (2.2) localized on the antidots. The probabilities evolve due to incoherent jumps of quasiparticles at the rates Γ_Δ (2.19) and Γ_l (2.20) between these states. The stationary quasiparticle current I through the antidots is found in this regime from the balance of the forward/backward transition across any of the three tunnel junctions of the system, e.g., from the transitions between the antidots:

$$I = e\nu[p_{10}\Gamma_\Delta(2\delta) - p_{01}\Gamma_\Delta(-2\delta)]\,. \tag{2.26}$$

In general, the quasiparticle current I can be calculated by the direct numerical solution of the kinetic equation. The results of such solution for the linear conductance $G = dI/dV|_{V=0}$ are shown in Fig. 2.3 (in all numerical results presented below we take $\nu = 1/3$). Qualitative behavior of the system can be

understood by analyzing the limits where the simple analytical expressions for the conductance can be obtained.

The first limit is $\Gamma_\Delta \ll \Gamma_l$, where the antidot-antidot tunnelling is the bottleneck for the current flow. In this case, to the zeroth-order approximation in Γ_Δ, the current is vanishing, and one can use in Eq. (2.26) the equilibrium probabilities $p_{ij} = (1/Z)e^{-\epsilon_{ij}/T}$, $Z = \sum_{ij} e^{-\epsilon_{ij}/T}$, obtaining for the conductance

$$G = \frac{(e\nu)^2\gamma}{T} \frac{f_g(2\delta)e^{\delta/2T}}{e^{-\epsilon/T} + e^{-(\epsilon+U)/T} + 2\cosh(\delta/T)} \,. \tag{2.27}$$

Equation (2.27) describes the "coalesced" conductance peak that corresponds to the addition of two quasiparticles to the antidots. At large temperatures, $T \geq U$, the peak has a usual thermally-broadened shape with width proportional to T. At $T \ll U$, however, the peak shape (2.27) is quite unusual: the conductance is constant between the point $\epsilon \simeq 0$, when the first quasiparticle is added to the antidots, and the point $\epsilon \simeq -U$ of addition of the second quasiparticle, forming the plateau of width U – see Fig. 2.3. The conductance plateau remains flat until the temperature is lowered to $T \simeq U/\ln[\Gamma_l(U)/\Gamma_\Delta]$, when the thermal suppression of the antdot-edge tunnelling rate makes it comparable to Γ_Δ at the center of the plateau, $\epsilon \simeq -U/2$, despite the fact that the two rates are very different at $\epsilon \simeq 0$. In this temperature range, a dip develops in the center, which separates the plateau into two peaks, one at $\epsilon \simeq 0$ and the other at $\epsilon \simeq -U$, with decreasing temperature (Fig. 2.3). Each peak corresponds to addition of one quasiparticle to the double-antidot system. Note that the resonant peaks occur when the gate bias energy ϵ is equal to "minus energy" of the antidot state, so that the total energy of the state relative to the chemical potential of the edges is zero.

The shape of such single-quasiparticle peaks can be described in the opposite limit of strong antidot-antidot tunnelling $\Gamma_\Delta \gg \Gamma_l$. In this limit, the general kinetic equations for three probabilities p_{00}, p_{10}, p_{01} relevant at $\epsilon \simeq 0$, e.g.,

$$\dot{p}_{00} = \Gamma_1(-\epsilon_1)p_{10} + \Gamma_2(-\epsilon_2)p_{01} - [\Gamma_1(\epsilon_1) + \Gamma_2(\epsilon_2)]p_{00}, \tag{2.28}$$

and similar equations for the other probabilities, can be reduced to two equations for the effective two-state system. The strong antidot-antdot tunnelling that couples the singly-occupied states $|10\rangle, |01\rangle$, maintains the relative equilibrium between them: $p_{10}/p_{01} = e^{-2\delta/T}$, making it possible to treat these two states as one. The effective transition rates between this state and the state $|00\rangle$ are obtained as the weighted average of the transition rates in starting kinetic equations, e.g. (2.28). The standard calculation of the current through a two-state system gives then the resonant peak of the double-antidot conductance at $\epsilon \simeq 0$ (associated with addition of the first quasiparticle to the

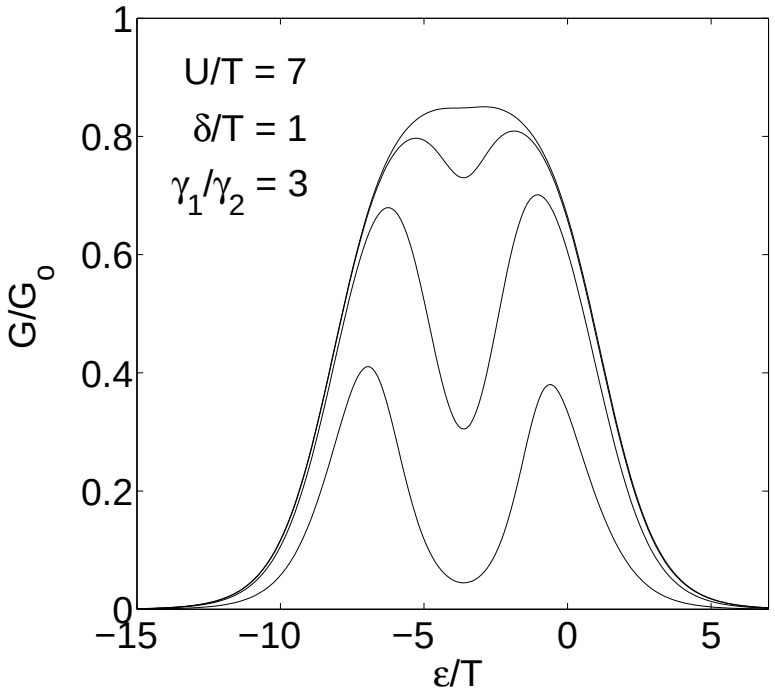

Figure 2.3: Conductance of the double-antidot system in the regime of overdamped quasiparticle transport. Conductance is normalized to $G_0 = (e\nu)^2\Gamma_\Delta(2\delta)/T$. Different curves correspond to different ratios of the antidot-antidot and antidot-edge tunnelling rates. From top to bottom: $\Gamma_\Delta(2\delta)/\Gamma_2(0) = 10^{-4}, 10^{-3}, 10^{-2}, 10^{-1}$.

antidots),

$$G = \frac{(e\nu)^2\Gamma_1(\epsilon_1)\Gamma_2(-\epsilon_2)f(2\delta)/T}{\Gamma_1(\epsilon_1)+\Gamma_2(\epsilon_2)+\Gamma_1(-\epsilon_1)f(-2\delta)+\Gamma_2(-\epsilon_2)f(2\delta)}\,, \tag{2.29}$$

where $f(E) = f_1(E)$ is the Fermi distribution function. For instance, if the two antidot states are aligned, $\delta = 0$,

$$G = \frac{(e\nu)^2}{T}\frac{\gamma_1\gamma_2}{\gamma_1+\gamma_2}\frac{f_\nu(\epsilon)}{1+2e^{-\epsilon/T}}\,. \tag{2.30}$$

The conductance peak at $\epsilon \simeq -U$ associated with the addition of the second quasiparticle is given by an expression similar to Eq. (2.29) with an appropriate shift of energy $\epsilon \to \epsilon + U$. In particular, for $\delta = 0$, this expression

reduces to

$$G = \frac{(e\nu)^2}{T} \frac{\gamma_1\gamma_2}{\gamma_1+\gamma_2} \frac{f_\nu(\epsilon+U)}{2+e^{-(\epsilon+U)/T}} \,. \tag{2.31}$$

The conductance peak (2.30) is asymmetric around $\epsilon = 0$, since in the tunnelling dynamics underlying this peak, only one quasiparticle can tunnel off the antidots, while there are two available states for tunnelling onto the antidots. Still, the "quasiparticle-quasihole" symmetry makes the two peaks, (2.30) and (2.31), at $\delta = 0$ symmetric images of each other with respect to a "mirror" reflection $\epsilon + U/2 \to -(\epsilon + U/2)$. For $\delta \neq 0$, the condition $\Gamma_\Delta \gg \Gamma_l$ is violated at sufficiently low temperatures $T \ll \delta$, and Eq. (2.29) becomes invalid. In this case, the antidots are effectively out of resonance, and conductance peaks are suppressed exponentially with temperature at all gate bias energies ϵ.

2.3.2 Weak decoherence

If the edge-state decoherence is sufficiently weak and allows for quantum-coherent transfer of quasiparticles between the two antidots, the kinetic equation for quasiparticle transport should be written not in the basis of states, (2.2), but in the basis of the hybridized states (2.22). As follows from the estimates of the edge-state decoherence in Sec. 2.1.3, even in this regime, the edge-induced relaxation rate Γ_d (2.13) should be strong enough, $\Gamma_d \gg \Gamma_l$, to maintain the equilibrium distribution of quasiparticles over the antidot states in the process of tunnelling. This means that if $E_k^{(n)}$ is the energy of the state $|k\rangle$ when there are n quasiparticles on the antidots, the probability that this state is occupied is $\rho_k(n) = (1/Z_n)e^{-E_k^{(n)}/T}$, $Z_n = \sum_k e^{-E_k^{(n)}/T}$. The quasiparticle tunnelling is reduced then to the dynamics of the total number n of quasiparticles on the antidots, described by the probability distribution $p(n)$. The rates of tunnelling transitions $n \to n \pm 1$ in this dynamics are:

$$\Gamma^\pm(n) = \sum_{l=1,2} \Gamma_l^\pm(n), \quad \Gamma_l^\pm(n) = \sum_{kq} \rho_k(n)\Gamma_l(k,q,n,n\pm 1) \,. \tag{2.32}$$

where the partial transitions rates $\Gamma_l(p,k,n,n\pm1)$ from the state p of n quasiparticles into the state k of $n \pm 1$ quasiparticles are given by the appropriate tunnelling rates (2.25) between the lth edge and antidot. The solution of the simple kinetic equation

$$\dot{p}(n) = \sum_\pm \left[\Gamma^\mp(n\pm1)p(n\pm1) - \Gamma^\pm(n)p(n)\right] \,, \tag{2.33}$$

gives then the stationary quasiparticle current through the system:

$$I = \nu e \sum_n \left[\Gamma_1^+(n) P(n) - \Gamma_1^-(n-1) P(n-1) \right] . \tag{2.34}$$

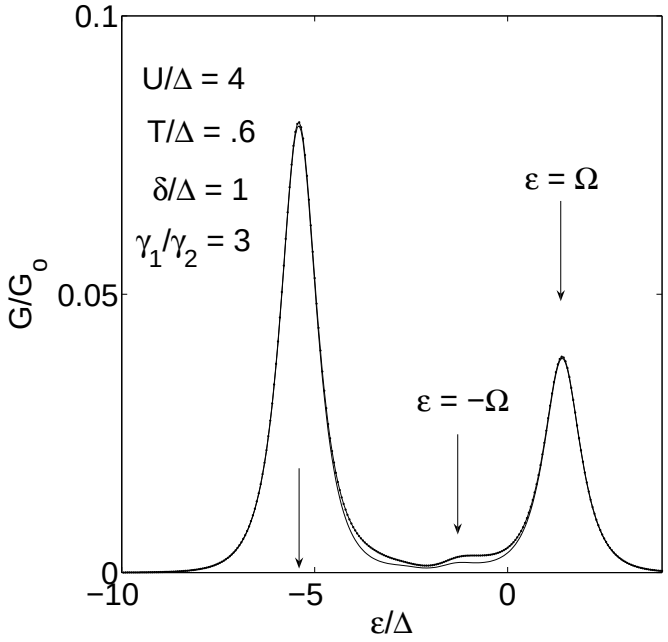

Figure 2.4: Conductance of the double-antidot system in the regime of the underdamped quasiparticle dynamics. Conductance is plotted in units of $G_0 = (e\nu)^2 \Gamma_1(0)/\Delta$. The curves show the two main resonant conductance peaks at $\epsilon = \Omega$ and $\epsilon = -(U + \Omega)$, and a weak kink at $\epsilon = -\Omega$ that is made visible by the Luttinger-liquid singularity in the tunnelling rates. The upper and lower curves are, respectively, the conductance with and without equilibration on the antidots.

Equation (2.33) shows that the stationary probability distribution $p(n)$ satisfies the "detailed balance" condition $p(n)\Gamma^+(n) = p(n+1)\Gamma^-(n+1)$ even in the presence of the non-vanishing bias voltage V. Using this condition, and expanding both $p(n)$ and the tunnelling rates $\Gamma(n)$ to first order in V, one

finds the linear conductance G of the quasiparticle qubit,

$$G = \eta \frac{(e\nu)^2}{T} \sum_n w_n \frac{\Gamma_1^+(n)\Gamma_2^+(n)}{\Gamma_1^+(n) + \Gamma_2^+(n)} \,. \tag{2.35}$$

Here $w_n = Z_n/Z$ is the equilibrium probability to have n quasiparticles on the antidots, $Z = \sum_n Z_n$, and the factor η gives the fraction of the voltage V that drops across the edge-antidot junctions. Equation (2.35) can be understood in terms of forward jumps of quasiparticles in the left junction contributing to the current only if they are followed by the forward jumps in the right junction. As an example, at temperatures $T \ll U$, and $\epsilon \simeq -\Omega$ one can limit the sum in Eq. (2.35) to one term $n = 0$. The conductance G is then,

$$G = \frac{(e\nu)^2}{T} \frac{\eta}{1 + 2e^{-\epsilon/T}\cosh(\Omega/T)} \cdot$$

$$\frac{\sum_{q,k} \Gamma_{1q}(\epsilon + (-1)^q\Omega)\Gamma_{2k}(\epsilon + (-1)^k\Omega)}{\sum_{l,m} \Gamma_{lm}(\epsilon + (-1)^m\Omega)} \,, \tag{2.36}$$

where the tunnelling rates Γ_{qk} are defined in Eq. (2.25).

For comparison, one can calculate the conductance in the same regime $T \ll U$, $\epsilon \simeq -\Omega$, but without equilibration on the antidots, i.e. assuming that the edge-state decoherence is very weak, $\Gamma_d \ll \Gamma_l$. As before, the antidots can be occupied in this regime at most by one quasiparticle at a time, and straightforward solution of the kinetic equation describing the occupation of individual energy eigenstates due to transitions (2.25) gives the conductance,

$$G = \frac{(e\nu)^2}{T} \frac{\Delta^2}{2\Omega^2} \frac{\eta\gamma_1\gamma_2}{1 + 2e^{-\epsilon/T}\cosh(\Omega/T)} \cdot$$

$$\sum_{\pm} \frac{f_\nu(\epsilon \pm \Omega)}{\gamma_1(1 \mp \delta/\Omega) + \gamma_2(1 \pm \delta/\Omega)} \,. \tag{2.37}$$

Equation (2.37) describes the resonant conductance peak that corresponds to the addition of the first quasiparticle to the antidot. The second quasiparticle peak at $\epsilon = -(U + \Omega)$ is described by the similar expression. At low temperatures, $T \ll \Omega$, only the lowest energy eigenstate with energy $-\Omega$ contributes to the conductance (2.37). In this case, the equilibration on the antidots does not have any effect, and Eqs. (2.36) and (2.37) coincide. As one can see from Fig. 2.4, which plots the conductance obtained by numerical solution of the full kinetic equation, the difference between the two regimes, with and without relaxation, remains very small even at moderate temperatures. At larger

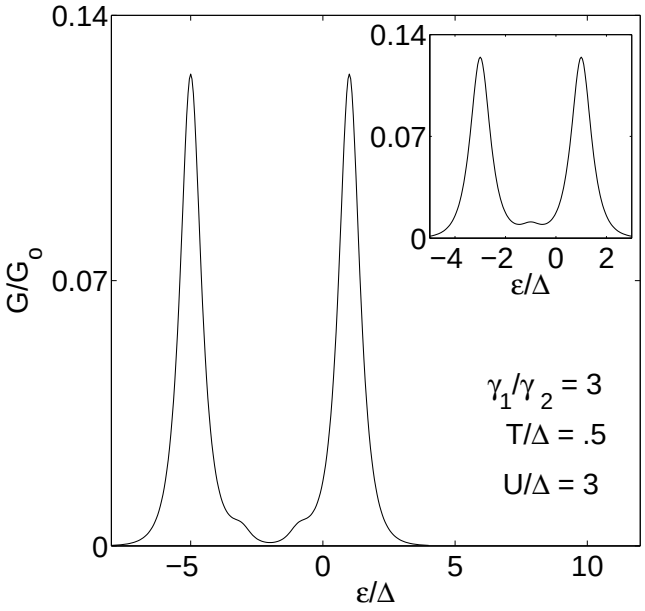

Figure 2.5: Conductance of the symmetric ($\delta = 0$) antidot qubit exhibiting two resonant conductance peaks at $\epsilon = \Delta$ and $\epsilon = -(U+\Delta)$. Both peaks have kinks at $\epsilon = -\Delta$ and $\epsilon = -(U-\Delta)$ caused by the Luttinger-liquid singularity in the tunnelling rates. The inset shows the conductance for the special value of interaction energy $U = 2\Delta$, when the two kinks coincide producing very small but visible additional conductance peak. Conductance is normalized as in Fig. 2.4.

temperatures, $\Omega \ll T \ll U$, and $\delta = 0$, Eq. (2.37) reduces to Eq. (2.30) for the conductance in the overdamped regime. The only difference between the two results is the factor η in Eq. (2.37) which implies that the part of the applied bias voltage that drops across the region of the quantum-coherent quasiparticle dynamics does not contribute to the linear conductance.

Besides the two main resonant peaks, the curves in Fig. 2.4 exhibit also a small kink at $\epsilon \simeq -\Omega$. This kink appears at the intermediate temperatures and is the result of the transfer of the first quasiparticle added to the antidots not through the more probable ground state of the qubit but through the excited state with energy Ω. One could see, however, by plotting the conductance of the double-antidot system for tunnelling electrons (the tunnelling rates given by the $g = 1$ in Fig. 2.2) that the contribution of the excited state to the conductance is not sufficient by itself to produce such a kink. The kink in

the conductance appears only when the contribution from the excited state is amplified by the Luttinger-liquid singularity in the quasiparticle tunnelling rate (seen in the $g = 1/3$ curve in Fig. 2.2 as a peak at zero energy). It becomes somewhat more pronounced in the conductance peaks of the "symmetric" qubit with $\delta = 0$ shown in Fig. 2.5. In this case, the kinks appear on both peaks: at $\epsilon = -\Delta$ and $\epsilon = -(U - \Delta)$. The second kink is due to transport through the ground state of the qubit in the regime when the main contribution to conductance comes from the excited state. As shown in the inset in Fig. 2.5, at the special value of the interaction energy $U \simeq 2\Delta$, the two kinks coincide and form a weak additional peak of the qubit conductance.

2.4 Conclusion

We have calculated the linear conductance G of the double-antidot system in the regime of weak quasiparticle tunnelling through the antidots. Depending on the strength of the edge-state decoherence, the tunnelling can be coherent or incoherent. In the incoherent regime, the two resonant conductance peaks that correspond to the two antidot states are spaced by the quasiparticle interaction energy U. In the coherent regime, this spacing is increased to $U + 2\Omega$, where 2Ω is the gap between the energy eigenstates of the double-antidot system. This regime of quasiparticle dynamics is also characterized by the Lorentzian dependence of the system conductance, $G \propto (1 + \delta^2/\Delta^2)^{-1}$, on the energy difference δ between the antidots. In the quantum-coherent regime, the double-antidot system can be used as a quasiparticle qubit.

Chapter 3

Transport in Multi-Antidot Systems

In the last chapter we discussed transport in a system consisting of two sequentially tunnel coupled antidots. However, due to the geometry of that particular setup, the exchange statistics of the quasiparticles did not influence the conductance. More specifically, the particular geometry that was considered did not allow for the possibility for quasiparticles to be exchanged. Here, we consider [84] the situation when quasiparticles can tunnel between multiple antidots. The main motivation for this is to explore how the anyonic exchange statistics of the enter into the conductance of these systems and to propose a method to determine the exchange statistics of these particles. As mentioned in Chapter 1, recent experiments [10, 11] demonstrating unusual flux periodicity of conductance of a quasiparticle interferometer can be interpreted as a manifestation of the fractional statistics [12, 13], this interpretation is not universally accepted [14, 15]. There is a number of different theoretical proposals (see, e.g., [80, 81]) suggesting more complicated tunnel structures where the statistics should manifest itself through noise properties. Partly due to complexity of noise measurements, such experiments have not been performed successfully up to now. Here, we show that coherent quasiparticle dynamics in multi-antidot structures should provide clear signatures of the quasiparticle exchange statistics in dc transport properties. Most notably, in tunneling through a line of three antidots, statistics should manifest itself directly as a non-vanishing resonant peak of the tunnel conductance which would vanish if the tunneling particles had fermionic exchange statistics.

In the next section we start by discussing the general model of a multiple anti-dot system and also introduce the concept of hard-core anyons. The section will then conclude with a method for calculating the matrix elements of the tunnel Hamiltonian between states of one and two quasiparticles occupying

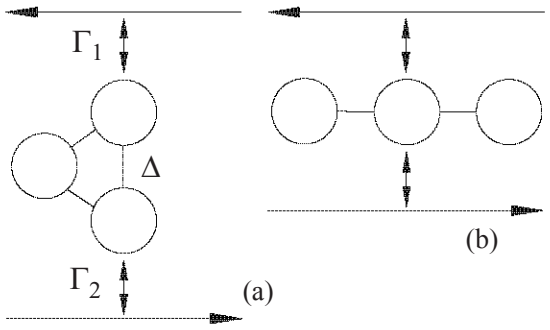

Figure 3.1: Tunneling of anyonic quasiparticles between opposite edges of an FQHE liquid through triple-antidot systems with quasi-1D dynamics of anyons: (a) loop with periodic boundary conditions; (b) open interval. Quasiparticles tunnel between the edges and the antidots with characteristic rates $\Gamma_{1,2}$. The antidots are coupled coherently by tunnel amplitudes Δ.

the antidot system, which is used to determine the conductance. In the last section we explicitly evaluate the conductance for a system consisting of a line of antidots and discuss its relevance to the measurement of the anyonic exchange statistics of the quasiparticles.

3.1 Model

As mentioned earlier, the overall goal of this work is to extend the theory developed in chapter 2 to structures where the statistics of the quasiparticles *does* indeed affect the conductance. The two simplest structures that exhibit this property consist of three antidots and have quasi-1D geometry with either periodic or open boundary conditions (Fig. 3.1). Below, we focus mostly on the conductance of these structures, although the main elements of our approach are valid for more general 1D systems of anyons. A technical issue that needed to be resolved is to calculate the tunnel conductance of these structures is that the second-quantized field operators of anyons defined through the Wigner-Jordan transformation [93–96], are not fully sufficient in the situations of tunnelling. As we show below, to obtain correct matrix elements for anyon tunneling, one needs to keep track of the appropriate boundary conditions of the anyonic wavefunctions which are not accounted for in the field operators.

Specifically, we consider the antidots coupled by tunneling among themselves and to two opposite edges of the quantum Hall liquid (Fig. 3.1). The edges play the role of the quasiparticle reservoirs with the transport voltage

e^*V applied between them. To focus the discussion on the regime of coherent transport of individual quasiparticles we assume that the antidot-edge coupling is weak and can be treated as a perturbation. Quasiparticle transport through the antidots is governed then by the kinetic equation similar to that for Coulomb-blockade transport of electrons through quantum dots with a discrete energy spectrum [85–87] and was discussed in the previous chapter. In addition, coherent quasiparticle dynamics requires that the relaxation rate Γ_d created by direct Coulomb antidot-edge coupling is weak. As was discussed previously, this condition should be satisfied if the edge-state confinement, which determines the velocity of the edge propagation, is sufficiently strong [70]. The model presented here follows along the same lines as in Chapter 2 namely that we assume all quasiparticle energies on the antidots, tunnel amplitudes Δ, temperature T, Coulomb interaction energies U between quasiparticles on different antidots, are much smaller than the energy gap Δ^* for excitations on each antidot. This condition ensures that the state of each antidot is characterized completely by the occupation number n of the relevant quantized state localized at this antidot. In any given range of the backgate voltage or magnetic field (which produces the overall shift of the antidot energies - see, e.g., [7, 21–23]), there can be at most one quasiparticle on each antidot, $n = 0, 1$. This "hard-core" property of the quasiparticles means that they behave as fermions in terms of their occupation factors, despite the anyonic exchange statistics. All these assumptions can be summarized as: $\Gamma_d, \Gamma_j \ll \Delta, U, T \ll \Delta^*$.

Under these conditions, the antidot tunneling is dominated by the quasiparticle energies on the antidots. The quasi-1D geometry of the antidot systems we consider makes it possible to introduce quasiparticle "coordinate" x numbering successive antidots; e.g., $x = -1, 0, 1$ for systems in Fig. 3.1. The quasiparticle Hamiltonian can be written then in the second-quantized form as

$$H = \sum_x [\epsilon_x n_x - (\Delta_x \xi^\dagger_{x+1} \xi_x + h.c.)] + \sum_{x<y} U_{x,y} n_x n_y \,, \tag{3.1}$$

where ϵ_x are the energies of the relevant localized states on the antidots (taken relative to the common chemical potential of the edges at $V = 0$), Δ_x is the tunnel coupling between them, $U_{x,y}$ is the quasiparticle Coulomb repulsion, and $n_x \equiv \xi^\dagger_x \xi_x$. From the point of view of the standard edge-state tunneling theory, the quasiparticle operators $\xi^\dagger_x, \xi_x$ in (3.1) can be understood as the Klein factors left in the standard operators for the edge-state quasiparticles when all the edge magneto-plasmon modes are suppressed by the gap Δ^* as pointed out in the discussion in Section 2.1.2. In 1D structures, the Wigner-Jordan transformation expresses them in terms of the Fermi operators c_x in a

way that produces the necessary exchange statistics $\pi\nu$ [93]:

$$\xi_x = e^{i\pi(\nu-1)\sum_{z<x} n_z} c_x \,,\ \xi_y \xi_x = \xi_x \xi_y e^{i\pi\nu sgn(x-y)}, \tag{3.2}$$

with similar relations for $\xi^\dagger$.

3.1.1 Hard-core Anyons

Anyonic exchange statistics creates an effective interaction between the quasiparticles which can be understood as the Aharonov-Bohm (AB) interaction between a flux tube "attached" to one of the particles and the charge carried by another. Quasiparticle transport in antidots is also affected by their Coulomb interaction U. In the *antidot loop* (Fig. 2.1a), however, the Coulomb interaction is constant $U_{x,y} = U$, and the interaction term in the Hamiltonian (3.1) reduces to $Un(n-1)/2$, with $n = \sum_x n_x$ – the total number of the quasiparticles on the antidots. In this case, the Coulomb interaction contributes to the energy separation between the group of states with different n, but does not affect the level structure for given n, which is determined by the "single-particle" part of the Hamiltonian (3.1). The hard-core property of quasiparticles limits n to the interval $[0, 3]$. For $n = 0$ and $n = 3$, the system is in the "empty" and "completely filled" state with respective energies $E_0 = 0\,, E_3 = \sum_x \epsilon_x + 3U$. The spectrum E_{1k} of the three $n = 1$ states $|1k\rangle = \sum_x \phi_k(x)\xi_x^\dagger|0\rangle$, is obtained as usual from the Hamiltonian (3.1). In the case of the uniform loop, $\epsilon_x = \epsilon$, $\Delta_x = \Delta$, with an external AB phase φ, one has $\phi_k(x) = e^{ikx}/L^{1/2}$ and

$$E_{1k} = \epsilon - \Delta\cos k\,,\ k = (2\pi m + \varphi)/L\,, \tag{3.3}$$

where $m = 0, 1, 2$, and the length of the loop is $L = 3$.

Anyonic statistics of the quasiparticles can be seen in the $n = 2$ states, $|2l\rangle = (1/\sqrt{2})\sum_{xy}\psi_l(x,y)\xi_y^\dagger\xi_x^\dagger|0\rangle$. The fermion-anyon relation (3.2) suggests that the structure of stationary two-anyon wavefunctions should coincide up to the exchange phase with that for free fermions:

$$\psi_l(x,y) = \frac{e^{i\pi(1-\nu)sgn(x-y)/2}}{\sqrt{2}} \det\begin{pmatrix} \phi_q(x) & \phi_q(y) \\ \phi_p(x) & \phi_p(y) \end{pmatrix}. \tag{3.4}$$

Here ϕs are the single-particle eigenstates of the Hamiltonian (3.1). (The states (3.4) are numbered with the index l of the third "unoccupied" eigenstate of (3.1) complementary to the two occupied ones q, p.) The boundary conditions for the ϕs are affected by the exchange phase in Eq. (3.4). To find them, we temporarily assume for clarity that coordinates x, y are continuous and

lie in the interval $[0, L]$. Subsequent discretization does not change anything substantive in this discussion. The 1D hard-core particles are impenetrable and can be exchanged only by moving one of them, say x, around the loop from $x = y + 0$ to $x = y - 0$ (Fig. 3.2a). Since the loop is imbedded in the underlying 2D system, such an exchange means that the wavefunction acquires the phase factor $e^{i\pi\nu}$, in which the sign of ν is fixed by the properties of the 2D system, e.g. the direction of magnetic field in the case of FQHE liquid. Next, if the second particle is moved similarly, from $y = x + 0$ to $y = x - 0$, the wavefunction changes in the same way, for a total factor $e^{i2\pi\nu}$. Equation (3.4) shows that only one of these changes can agree with the 1D form of the exchange phase. As a result, the wavefunction (3.4) satisfies different boundary conditions in x and y:

$$\psi_l(L, y) = \psi_l(0, y)e^{i\varphi},\ \psi_l(x, L) = \psi_l(x, 0)e^{i(\varphi+2\pi\nu)}. \tag{3.5}$$

Conditions (3.5) on the wavefunction (3.4) mean that the single-particle functions ϕ in (3.4) satisfy the boundary condition that correspond to the effective AB phase $\varphi' = \varphi + \pi - \pi\nu$, i.e. the addition of an extra quasiparticle to the loop changed the AB phase by $\pi - \pi\nu$, where $-\pi\nu$ comes from the exchange statistics and π from the hard-core condition. This gives the energies of the two-quasiparticle states (3.4) as $U + E_{1q} + E_{1p}$, where, if the loop is uniform, the single-particle energies are given by Eq. (3.3) with $\varphi \to \varphi'$. In this case, $\sum_k E_{1k} = 0$, and the energies E_{2l} of the two-quasiparticle states can be written as:

$$E_{2l} = 2\epsilon + U - \Delta\cos l\,,\ l = (2\pi m' + \varphi - \pi\nu)/3\,, \tag{3.6}$$

where $m' = 0, 1, 2$.

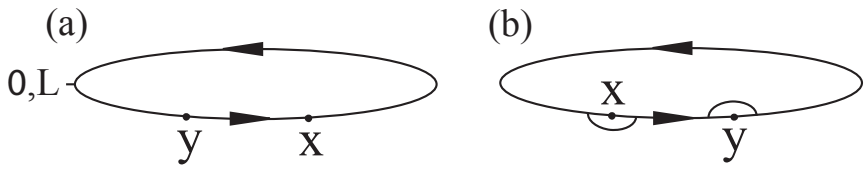

Figure 3.2: Exchanges of hard-core anyons on a 1D loop: (a) real exchanges by transfer along the loop embedded in a 2D system; (b) formal exchanges describing the assumed boundary conditions (3.5) of the wavefunction.

3.1.2 Tunnel Matrix Elements

One of the consequences of the above discussion is that the sign of ν in the 1D exchange phases of Eqs. (3.2) and (3.4) can be chosen arbitrarily for a given fixed sign of the 2D exchange phase. Reversing this sign only exchanges the character of the boundary conditions (3.5) between x and y. This fact has simple interpretation. Although the 1D hard-core anyons can not be exchanged directly, formally, coordinates x and y in Eq. (3.4) are independent and one needs to define how they move past each other at the point $x = y$. Depending on whether the x-particle moves around y from below or (as in Fig. 3.2b) from above, its trajectory does or does not encircle the flux carried by the y particle, and the boundary condition for x is or is not affected by the statistical phase. The choice made for x immediately implies the opposite choice for y (Fig. 3.2b), accounting for different boundary conditions (3.5). This interpretation shows that in calculation of any matrix elements, the participating wavefunctions should be taken to have the same boundary conditions. While this requirement is natural for processes with the same number of anyons, it is less evident for tunneling that changes the number of anyons in the system. Indeed, the most basic, tunnel-Hamiltonian, description of tunneling into the point z of the system leads to the states

$$\xi_z^\dagger|1k\rangle = (1/\sqrt{2})\sum_{xy}\psi_k(x,y)\xi_y^\dagger\xi_x^\dagger|0\rangle\,, \tag{3.7}$$

$$\psi_k(x,y) = [\phi_k(x)\delta_{y,z} - e^{i\pi(1-\nu)sgn(x-y)}\delta_{x,z}\phi_k(y)]/\sqrt{2}\,.$$

One can see that Eq. (3.7) automatically implies specific choice of the boundary conditions which physically corresponds to the tunneling anyon not being encircled by anyons already in the system. This means that in the calculation of the tunnel matrix elements with the states (3.4), one should always pair the coordinate of the tunneling anyon with the discontinuous one in (3.5). With this understanding, the tunnel matrix elements are obtained as

$$\langle 2l|\xi_z^\dagger|1k\rangle = \sqrt{2}\sum_x \psi_l^*(x,z)\phi_k(x)\,. \tag{3.8}$$

For instance, in the case of uniform loop with states (3.3) and (3.6), we get up to an irrelevant phase factor

$$\langle 2l|\xi_z^\dagger|1k\rangle = (2/3)\cos[(k-l)/2]\,. \tag{3.9}$$

Specific anyonic interaction between quasiparticles can be seen in the fact that the matrix elements (3.9) do not vanish for any pair of indices k, l. In the

fermionic case $\nu = 1$, one of the elements (3.9) always vanishes for any given k, since the two-particle state after tunneling necessarily has one particle in the original single-particle state. By contrast, the tunneling anyon can shift existing particle out of its state.

The matrix elements involving empty or fully occupied states coincide with those for fermions. Taken together with Eqs. (3.8) and (3.9) for transitions between the partially filled states, they determine the rates $\Gamma_j(E) = \gamma_j f_\nu(E)|\langle\xi_z^\dagger\rangle|^2$ of tunneling between the jth edge and the antidots, where γ_j is the overall magnitude of the tunneling rate, and $f_\nu(E)$ is given by Eq. (2.20). Similarly to what was done in chapter 2 the rates $\Gamma_j(E)$ can be used in the kinetic equation to calculate the conductance of the antidot system. Anyonic statistics of quasiparticles affects the position and amplitude of the resonant peaks of conductance through the shift of the energy levels by quasiparticle tunneling (described, e.g., by Eq. (3.6)) and through the kinetic effects caused by the anyonic features in the matrix elements (3.8). In the case of the antidot loop (Fig. 3.1a), however, effects of statistics are masked by the fact that the external AB flux φ through the loop is essentially random, since the antidot area is much larger than the area of the loop and φ can not be controlled by variations of external magnetic field on the relevant scale of one period of conductance oscillations. Below, we present the results for conductance for the similar case of a *line of antidots* (Fig. 3.1b), the conductance of which is insensitive to the AB phase, and shows effects of fractional statistics in the tunneling matrix elements.

3.2 Conductance of the Antidot Line Junction

As before, the quasiparticle Hamiltonian is given by Eq. (3.1). In this geometry, the interaction energy $U_1 \equiv U_{1,0} = U_{0,-1}$ between the nearest-neighbor antidots is in general different from the interaction $U_2 \equiv U_{1,-1}$ between the quasiparticles at the ends. The localization energies on the antidots can be written as $\epsilon_j = \epsilon + x\delta + 2\lambda|x|$. We consider first the unbiased line, $\delta = 0$. At low temperatures, $T \ll \Delta, U$, only the ground states of n quasiparticles with energies E_n participate in transport: $E_0 = 0$, $E_1 = \epsilon + \lambda - \omega$, $E_2 = 2\epsilon + 3\lambda - \bar{\omega} + (U_a + U_b)/2$, and $E_3 = 3\epsilon + 2U_a + U_b + 4\lambda$, where $\omega = (\Delta_1^2 + \Delta_2^2 + \lambda^2)^{1/2}$ and $\bar{\omega}$ is given by the same expression with λ replaced by $\bar{\lambda} = \lambda - (U_1 - U_2)/2$. In this regime, the linear conductance G consists of three resonant peaks, with each peak associated with addition of one more

quasiparticle to the antidots,

$$G = \frac{(e\nu)^2}{T} \frac{\gamma_1\gamma_2}{\gamma_1+\gamma_2} \frac{a_n f_\nu(E_{n+1}-E_n)}{1+\exp[-(E_{n+1}-E_n)/T]}\,, \tag{3.10}$$

where $a_n \equiv |\langle n+1|\xi_0^\dagger|n\rangle|^2$. The amplitudes a_0, a_2 are effectively single-particle, and thus, independent of the exchange statistics: $a_0 = (\omega+\lambda)/2\omega$, and $a_2 = (\bar{\omega}-\bar{\lambda})/2\bar{\omega}$. By contrast, the amplitude a_1 of the transition from one to two quasiparticles is multi-particle, and is found from Eqs. (3.4) and (3.8) to be strongly statistics-dependent,

$$a_1 = \frac{\Delta_1^2\Delta_2^2}{(\omega+\lambda)\omega(\bar{\omega}-\bar{\lambda})\bar{\omega}} \cos^2(\pi\nu/2)\,. \tag{3.11}$$

In particular, a_1 vanishes in the case of electron tunneling ($\nu = 1$), but is non-vanishing in the case of fractional statistics, e.g., for $\nu = 1/3$, when $\cos^2(\pi\nu/2) = 3/4$. We illustrate this in Fig. 3.3 which shows the tunnel conductance G of the antidot system. This was obtained by solving the kinetic equation in the case of weak edge state induced relaxation similarly to what was done in section 2.3.2. Qualitatively, the vanishing amplitude a_1 for electrons can be understood as a result of destructive interference between the two terms in the wavefunction which correspond to different ordering of the added/existing electron on the antidot line. Fractional statistics of quasiparticles makes this destructive interference incomplete. Finite bias $\delta \neq 0$ along the antidot line suppresses this interference making the effect of the statistics smaller. One can still distinguish the fractional statistics by looking at the dependence of the amplitude of the middle peak of conductance on the bias δ shown in the right inset in Fig. 3.3.

3.3 Conclusion

In conclusion, we have developed a model of coherent transport of anyonic quasiparticles in systems of multiple antidots. In antidot loops, addition of individual quasiparticles shifts the quasiparticle energy spectrum by adding statistical flux to the loop. In the case without loops, energy levels are insensitive to quasiparticle statistics, but the statistics still manifests itself in the quasiparticle tunneling rates and hence dc tunnel conductance of the antidot system.

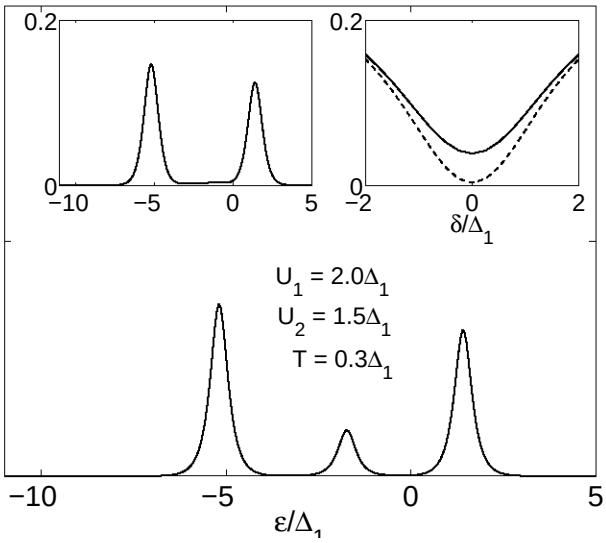

Figure 3.3: Linear conductance G of the antidot line in a $\nu = 1/3$ FQHE liquid (Fig. 3.1b) as a function of the common antidot energy ϵ relative to the edges. In contrast to electrons ($\nu = 1$, left inset), tunneling of quasiparticles with fractional exchange statistics produces non-vanishing conductance peak associated with transition between the ground states of one and two quasiparticles. The maximum of this peak is shown in the right inset ($\nu = 1/3$ – solid, $\nu = 1$ – dashed line) as a function of the bias δ. The curves are plotted for $\Delta_1 = \Delta_2$, $\lambda = 0$, $\gamma_1 = \gamma_2$; conductance is normalized to $G_0 = (e\nu)^2\Gamma_1(0)/\Delta_1$.

Part II

Quantum Information

Chapter 4

Quantum Measurement with an Antidot Electrometer

Quantum computing based on quasiparticles of the fractional quantum Hall effect represents both an exciting application of quantum antidots and a viable alternative to other current approaches in QC. The motivation for this chapter is the following: in utilizing this particular scheme of quantum computation one needs to read out the final qubit state. As discussed below, the most natural solution to the problem of measuring FQHE qubits is to employ the quantum antidot electrometer (QAE) as a measurement device, as it operates in the exact same low temperature and high magnetic field conditions as FQHE qubits. This chapter is dedicated to an analysis of the QAE, operated as a linear amplifier, as a quantum detector for FQHE based qubits.

As shown in chapter 1, the characteristics of a quantum detector operating as a linear amplifier can be given in terms of its transport properties. In order to discuss transport, we model the QAE in the spirit of chapters two and three. Here again, we consider the experimentally relevant regime when both the temperature T and the bias e^*V are much less than the energy gap between single quasiparticle states on the antidot. This means that there can only be either $n = 0$ or 1 additional quasiparticles on the antidot. This also implies that the bosonic excitations of the edge states encircling the antidot are completely suppressed. Taken as a whole, these assumptions mean that the problem consists of a single resonant energy level ϵ coupled to two opposing edges states with chemical potentials $\mu_{1,2}$, as shown in Fig. 4.1. The tunnelling between the lth edge and antidot can be described quantitatively with the standard tunnel Hamiltonian

$$H_T^{(l)} = T_l \psi_l^\dagger \xi + h.c.\,, \tag{4.1}$$

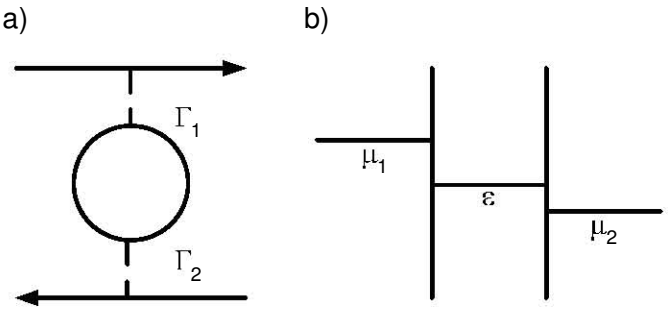

Figure 4.1: (a) Geometry of the QAE with the quasiparticle transfer rates $\Gamma_{1,2}$ between the edge states and antidot (b) Energy diagram with $\mu_{1,2}$ being the chemical potentials of the edge states and ϵ is the energy of the resonant level.

where $\psi, \psi^\dagger$ and $\xi, \xi^\dagger$ are the creation/annihalation operators for quasiparticles at, respectively, the edges and the antidot. In the regime when $\Gamma_j \ll T$, individual quasiparticle transport occurs via correlated tunnelling between the edges and antidot.

The simplest setup for which the QAE can be used as a detector is when the resonant energy level is sensitive to the state of the qubit. This can be accomplished if the QAE is coupled to the qubit electrostatically so that variations in the qubit's state cause the potential (and hence ϵ) to vary yielding an output current I from the detector which depends on the state of the qubit. In a case of a weakly coupled detector, when the variations of the energy level are small on the scale of e^*V and Γ_j and its response faster than the qubit dynamics, we can analyze the QAE from the viewpoint of linear amplifier theory [26, 27].

It is interesting to point out the similarities between the QAE acting as a detector and the single electron transistor (SET) which has been used as a detector for solid state QC [64, 65, 97–99]. The SET consists of a small metallic island tunnel coupled to two electrodes which serve as electron (Fermi-Liquid or FL) reservoirs. The SET is operated in the limit where the energy to add an electron to the island, or charging energy E_C, is larger than the temperature and the resistances of the tunnel junction between the island and electrodes are greater than h/e^2. When the bias energy eV is above the Coulomb Blockade threshold eV_t but less than E_C electron transport can occur via correlated sequential tunnelling through a single resonant level. The tunnel current I can be controlled by an external bias V_g capacitively coupled to the island. The use of the SET as a detector relies on making V_g (and therefore I) sensitive

to the state of the qubit. All this makes the principle of operation of the SET and QAE as detectors quite similar. The main new element is that in this case the role of the electrodes for tunnelling of quasiparticles is played by the edge states and therefore the Chiral Luttinger Liquid (CLL) properties of the edge states come in play. Therefore, this affords us the opportunity to explore how the strongly interacting nature of the edge states affects the measurement characteristics of the QAE.

The main quantities needed to analyze the QAE as a linear quantum detector are the zero frequency spectral densities of the charge S_Q and current S_I noise, the current charge cross correlation noise S_{IQ} and the linear response coefficient λ. Previous studies have focused on transport through a single antidot coupled between two CLL edge states [24, 25] as well as the resonant level model considered here [88]. The current noise characteristics have also been studied previously [100] for quantum dots coupled to non-chiral Luttinger Liquid leads as well as antidots operated in the FQHE regime [101, 102]. However, the Luttinger Liquid effects on the other transport properties mentioned above have remained unexplored. In the next section we will detail the calculations of the noise characteristics of the QAE and section 4.3 we will assess its measurement efficiency in various limiting cases.

4.1 Noise Calculation

In what follows, we calculate the noise characteristics utilizing the sequential tunnelling approximation. The starting point for the calculation is the kinetic equation for the occupancy of the resonant level,

$$\dot{\rho_0} = -\Gamma_+(\epsilon)\rho_0 + \Gamma_-(\epsilon)\rho_1 \tag{4.2}$$

$$\dot{\rho_1} = \Gamma_+(\epsilon)\rho_0 - \Gamma_-(\epsilon)\rho_1 \tag{4.3}$$

where $\rho_{0,1}$ are the occupation probabilities of the antidot and $\Gamma_\pm(\epsilon)$ are the rates of quasiparticle transfer onto or off of the antidot calculated to lowest order perturbation theory in the tunnel Hamiltonian (4.1). These are given similar to before as,

$$\Gamma_\pm(\epsilon) = \sum_{j=1,2} \Gamma_j^\pm(\epsilon)\,, \quad \Gamma_j^\pm(\epsilon) = \gamma_j f_\nu(\pm(\epsilon - \mu_j)). \tag{4.4}$$

where $f_\nu(E)$ and γ_j are given by Eqs. (2.19) and (2.20), respectively. This approximation is valid as long as $\gamma_j(\omega_c/2\pi T)^{1-\nu} \ll T$ [88]. From here on out we will change the notation of the energy of the resonant level so that

$\epsilon \to \epsilon - (\mu_1 + \mu_2)/2$ which then gives $\epsilon - \mu_{1,2} = \epsilon \mp e^* V/2$. In the subsequent discussions we will detail the calculations of the noise and transport properties discussed above.

In the case of the QAE detector, the energy of the resonant level ϵ depends on the state of the qubit. More specifically this implies that the qubit-detector interaction can be modelled in the same way as was discussed in Chapter 1,

$$H_{int}(t) = CQ(t)\sigma_z \tag{4.5}$$

where, C is the interaction strength, $Q = e^* n$ counts the excess charge on the antidot, and σ_z is the Pauli matrix.

The origin of the back-action dephasing for the QAE can be seen by inspecting (4.5). Fluctuations of the occupancy of the resonant level cause the off-diagonal matrix elements of the density matrix describing the qubit to decay. In the limit of weak detector-qubit coupling the back-action dephasing rate can be found to lowest order in (4.5) and is given by,

$$\Gamma_d = \pi C^2 S_Q, \tag{4.6}$$

where,

$$S_Q = \frac{(e^*)^2}{2\pi} \int d\tau \langle \delta n(\tau) \delta n(0) \rangle \tag{4.7}$$

is the zero frequency spectral density of the charge noise, $\delta n(t) = n(t) - \langle n \rangle$, and $\langle ... \rangle = Tr[... \bar{\rho} \otimes \rho_E]$ with $\bar{\rho}$ and ρ_E being the equilibrium density matrices of the antidot (obtained from the stationary solution to the kinetic equation) and the edges, respectively. To calculate the spectral densities of the charge and current noise we follow the method given in [103, 104]. The result for the charge noise can be given in terms of the transition rates in Eq. (4.4),

$$S_Q = \frac{(e^*)^2}{2\pi} \frac{\Gamma_+(\epsilon)\Gamma_-(\epsilon)}{\Gamma_T^3} \tag{4.8}$$

where, $\Gamma_T = \Gamma_+(\epsilon) + \Gamma_-(\epsilon)$.

With the QAE acting as a detector, the output current I yields information about the state of the qubit. In this case, the measurement time, or time needed to distinguish between the two states is given by

$$\tau_m = \frac{8\pi S_I}{\lambda^2 C^2}, \tag{4.9}$$

here,

$$S_I = \frac{1}{2\pi}\int d\tau \langle \delta I(\tau)\delta I(0)\rangle. \tag{4.10}$$

Quantitatively, since the resonant level ϵ is modified depending on the state of the qubit, the linear response coefficient can be related to the output current as, $\lambda = e^*\delta I/\delta\epsilon$, where δA represents the variation of the quantity A.

The current through the antidot can be obtained from the solution to the kinetic equation and is given by,

$$I = e^*\left(\gamma_1^+ - \gamma_1^-\right), \tag{4.11}$$

where $\gamma_1^{+(-)} = \Gamma_1^{+(-)}(\epsilon)\Gamma_{-(+)}(\epsilon)/\Gamma_T$ and correspond to transitions which take a quasiparticle from edge 1(2) to edge 2(1) via the resonant level on the antidot. Using this we can then find the current noise which is given by,

$$S_I = S_0 - \frac{(e^*)^2}{\pi\Gamma_T}\left[(\gamma_1^+)^2 g(\epsilon - e^*V/2) + (\gamma_1^-)^2 g(e^*V/2 - \epsilon)\right] \tag{4.12}$$

where,

$$S_0 = \frac{(e^*)^2}{2\pi}\left(\gamma_1^+ + \gamma_1^-\right) \tag{4.13}$$

and, $g(x) = 1 + e^{x/T}$. In the limit of vanishing bias $e^*V \to 0$, Eq. (4.12) reduces down to,

$$S_I = \frac{T}{\pi}G(\epsilon) \tag{4.14}$$

where,

$$G(\epsilon) = \frac{(e^*)^2}{T}\frac{\gamma_1\gamma_2}{\gamma_1+\gamma_2}\frac{f_\nu(\epsilon)}{1+e^{-\epsilon/T}} \tag{4.15}$$

is the differential conductance. This result is simply a statement of the fluctuation-dissipation theorem.

Finally, we turn our attention to the calculation of the current - charge cross correlation,

$$S_{IQ} = -\frac{e^*}{2\pi}\int d\tau \left[\langle I(\tau)n(0)\rangle - \langle I\rangle\langle n\rangle\right]. \tag{4.16}$$

In a similar fashion to what was done for the other noise spectra the cross correlation noise can be written in terms of the charge noise,

$$\mathrm{Re}\, S_{IQ} = \left(\gamma_1^+ - \gamma_1^-\right)\left(\frac{\Gamma_+^2 - \Gamma_-^2}{\Gamma_+\Gamma_-}\right)S_Q \tag{4.17}$$

As discussed in Chapter 1, in terms of linear response theory the two figures of merit [27] that characterize the performance of the QAE as a quantum detector are the measurement efficiency which is given in terms of the properties as,

$$\eta = \frac{\lambda^2}{16\pi^2 S_I S_Q}, \tag{4.18}$$

and the energy sensitivity given by,

$$\varepsilon = \frac{4\pi}{|\lambda|}\left[S_I S_Q - (\mathrm{Re}\, S_{IQ})^2\right]^{1/2}. \tag{4.19}$$

In the next section we will present results for both the energy sensitivity and efficiency in two special cases.

4.2 Results

4.2.1 Low Temperature Limit

The most natural operational regime for the detector is in the low temperature limit. Here, the system is less susceptible to thermal transitions which can degrade its performance. In the case of the QAE, this low temperature regime corresponds to the large bias limit $e^*V \gg T$.

In order calculate the transport properties we will need the asymptotic forms of the tunnelling density of states,

$$f_\nu(E) \sim \frac{1}{\Gamma(\nu)}\left(\frac{E}{2\pi T}\right)^{\nu-1}\theta\left(-\frac{E}{2\pi T}\right) \tag{4.20}$$

where $\theta(x)$ is the Heaviside function. This shows that for filling fractions of primary quantum hall liquids, the tunnel density of states exhibits a power law decay for $E \gg T$, as mentioned in chapter 2.

Utilizing Eq. (4.20), the current can be found from Eq. (4.11),

$$I = \frac{e^*}{\Gamma(\nu)}\frac{\gamma_1\gamma_2(\bar{x}-\bar{\epsilon})^{\nu-1}(\bar{x}+\bar{\epsilon})^{\nu-1}}{\gamma_1(\bar{x}-\bar{\epsilon})^{\nu-1}+\gamma_2(\bar{x}+\bar{\epsilon})^{\nu-1}} \tag{4.21}$$

where $\bar{x} = e^*V/4\pi T$ and $\bar{\epsilon} = \epsilon/2\pi T$. We can then use this expression to write the current noise, given by Eq. (4.12), as

$$S_I = \frac{e^* I}{2\pi}\left[1 - \frac{2\gamma_1\gamma_2(\bar{x}-\bar{\epsilon})^{\nu-1}(\bar{x}+\bar{\epsilon})^{\nu-1}}{\left[\gamma_1(\bar{x}-\bar{\epsilon})^{\nu-1}+\gamma_2(\bar{x}+\bar{\epsilon})^{\nu-1}\right]^2}\right]. \tag{4.22}$$

The linear response coefficient can be found using (4.21),

$$\lambda = e^* \frac{dI}{d\epsilon} = (\nu - 1) \frac{e^*}{2\pi T} \frac{I}{(\bar{x}^2 - \bar{\epsilon}^2)^2} \left[\frac{\gamma_1 (\bar{x} - \bar{\epsilon})^\nu - \gamma_2 (\bar{x} + \bar{\epsilon})^\nu}{\gamma_1 (\bar{x} - \bar{\epsilon})^{\nu-1} + \gamma_2 (\bar{x} + \bar{\epsilon})^{\nu-1}} \right]. \quad (4.23)$$

Finally, using Eqns. (4.4) and (4.17) the low temperature charge noise and charge - current cross correlation spectrum are,

$$S_Q = \frac{(e^*)^2}{2\pi} \frac{\gamma_1 \gamma_2 (\bar{x} - \bar{\epsilon})^{\nu-1} (\bar{x} + \bar{\epsilon})^{\nu-1}}{(\gamma_1 (\bar{x} - \bar{\epsilon})^{\nu-1} + \gamma_2 (\bar{x} + \bar{\epsilon})^{\nu-1})^3} \quad (4.24)$$

and,

$$\mathrm{Re}\, S_{IQ} = \left[\gamma_1 (\bar{x} - \bar{\epsilon})^{\nu-1} - \gamma_2 (\bar{x} + \bar{\epsilon})^{\nu-1} \right] S_Q. \quad (4.25)$$

There are two interesting cases which yield rather simple results for the measurement efficiency and energy sensitivity. The first case is found by an inspection of the result for the current noise, Eq. (4.22). When the condition such that,

$$\gamma_1 (\bar{x} - \bar{\epsilon})^{\nu-1} = \gamma_2 (\bar{x} + \bar{\epsilon})^{\nu-1} \quad (4.26)$$

is met, the current shot noise is said to be reduced, i.e. S_I reaches a minimum value of $e^* I/(4\pi)$. Shot noise suppression has been recently studied in transport through antidots coupled to CLL edge states [100–102]. In the case of fermions, $\nu = 1$, suppression only occurs when the tunnel amplitudes between the edges and the antidots are the same (i.e. $\gamma_1 = \gamma_2$). However, in the case of CLL shot noise suppression can occur even when the tunnel amplitudes are asymmetric. One way to understand this behavior is to notice that the tunnel rate for CLL edge states are dependent on the energy difference (in the low temperature limit) between the chemical potential of the edge and the resonant level, for example $\gamma_1 (\bar{x} - \bar{\epsilon})$. Therefore, even if $\gamma_1 \neq \gamma_2$ the biases can be tuned in such a way that the tunnel rates then become symmetric.

The question now becomes, how does the condition of shot noise suppression affect the measurement characteristics of the QAE? For one, inserting Eq. (4.26) into the expression for the current-charge cross correlation noise (4.17) reveals that $\mathrm{Re}\, S_{IQ} = 0$. As can be seen from Eqs. (4.18) and (4.19) this means that $\eta = \varepsilon^{-2}$. This results in a simple expression for the measurement efficiency,

$$\eta = \frac{(1-\nu)^2}{2\pi^2} \left[\frac{\gamma_1}{T} \frac{\alpha_\nu^{\nu-2}}{\Gamma(\nu)} \right]^2 \left(\frac{e^* V}{4\pi T} \right)^{2\nu-4}, \quad (4.27)$$

where, $\alpha_\nu = 2R^{\frac{1}{1-\nu}} (1 + R^{\frac{1}{1-\nu}})^{-1}$ and $R = \gamma_2/\gamma_1$ describes the tunnel asymmetry between the two edges. For primary quantum hall liquids, the above equation reveals that η has a power law decay for increasing bias. Furthermore, due to

the constraints of the sequential tunnelling approximation namely, $\gamma_1 \ll T$, the detector will not reach the quantum limit, $\eta = 1$.

Another limit that needs to be mentioned is the situation when,

$$\gamma_1(\bar{x} - \bar{\epsilon})^\nu = \gamma_2(\bar{x} + \bar{\epsilon})^\nu, \tag{4.28}$$

here, as can be seen from Eq. (4.23), the linear response coefficient vanishes. From the point of view of operating the QAE as a quantum detector this implies that η vanishes and, consequently, ε diverges. Clearly, the QAE will not work as a linear amplifier whenever $\bar{\epsilon}$ is tuned such that the condition (4.28) is satisfied.

4.2.2 Symmetric Voltage Drop, $\epsilon = 0$

The next case to consider is when the resonant level is tuned (either by a back-gate voltage or magnetic field) in such a way that the voltage drop between ϵ and one edge is equal to the voltage drop between the level and the other edge, thus $\epsilon = 0$. It is interesting to analyze the back-action noise in the limit of large biases $e^*V \gg T, \gamma_j$, Utilizing the asymptotic properties of the Gamma function in the limit of $e^*V/T \to \infty$ we have,

$$S_Q = \frac{(e^*)^2}{2\pi} \frac{\gamma_1\gamma_2}{(\gamma_1+\gamma_2)^3} \Gamma(\nu) \left| \frac{e^*V}{2\pi T} \right|^{1-\nu}, \tag{4.29}$$

where the prefactor $(\omega_c/2\pi T)^{1-\nu}$ has been absorbed into the tunnel rates γ_j. In the case of $\nu = 1$, Eq. (4.29) is independent of the bias voltage [65]. However, for $\nu = 1/(2n+1)$ the above equation shows that the charge noise and thus the back action dephasing rate of the qubit vary as $V^{1-\nu}$. Thus, for filling fractions of primary quantum hall liquids, the dephasing rate of the qubit actually increases for larger biases in contrast to FL edge states.

One of the most striking examples of CLL behavior can be found in the response coefficient. In the limit where $\epsilon = 0$, an explicit expression for this can be found:

$$\lambda = G(x) \left(\frac{R-1}{R+1} \right) F_\nu(x), \tag{4.30}$$

where we have defined,

$$F_\nu(x) = 2\sinh^2\left(\frac{x}{2T}\right) \left[1 - \frac{2}{\pi} \coth\left(\frac{x}{2T}\right) \operatorname{Im}\psi\left(\frac{\nu}{2} + i\frac{x}{2\pi T}\right) \right], \tag{4.31}$$

with $\psi(z)$ being the digamma function and $x = e^*V$. Note also the appearance

of the conductance $G(x)$ in Eq. (4.30), this is reflective of the fact that λ is a conductance in the sense that it measures the variation of the current via respect to ϵ versus the differential conductance that measures the variation of the current to changes in the bias.

In the case when $\nu = 1$ (i.e. the edges are described by Fermi-Liquids) then,

$$\mathrm{Im}\,\psi\left(\frac{\nu}{2} + \frac{ix}{2\pi T}\right) = \frac{\pi}{2}\tanh\left(\frac{x}{2T}\right) \tag{4.32}$$

and implies that $F(x) = 0$, and therefore λ vanishes. It is also important to note that this result is independent of the tunnel rate asymmetry R. The physical picture for this result can be thought of as follows: the rates $\gamma_{+(-)}$ describe forward (backward) transition between the two edges whereas the response coefficient looks at the variations of these rates as the energy of the resonant level is varied. In the case of Fermi-Liquid edge states the variation of both the forward and backward transitions are the same. This situation also occurs in the case of symmetric junctions $R = 1$ and is independent of ν. However, if there is any asymmetry between the junctions at all then, in the case of edge states described by CLL, λ has the behavior illustrated in Fig. (4.2). The reason for this can be seen by considering the behavior of the current as a function of ϵ, as shown in Fig. (4.3). When, $R = 1$ the I exhibits a peak about $\epsilon = 0$, thereby causing λ to vanish. However, as R is increased the peak shifts and thus causing the response coefficient to be non-vanishing. For large bias voltages $e^*V \gg T$ the response coefficient decays due to the power law behavior of the transition rates and is given by,

$$\lambda = \frac{(e^*)^2}{2\pi T}\frac{\gamma_1\gamma_2}{\gamma_1+\gamma_2}\frac{1-\nu}{\Gamma(\nu)}\frac{R-1}{R+1}\left(\frac{x}{2\pi T}\right)^{\nu-2}, \tag{4.33}$$

whereas for small biases $e^*V \ll T$, λ vanishes as x^2. However, in between the two extremes, the detector's response obtains a maximum occurring at approximately $e^*V \sim 2T$. As before, we can analyze the current in the limit of large biases the result is,

$$I = e^*\frac{\gamma_1\gamma_2}{\gamma_1+\gamma_2}\frac{1}{\Gamma(\nu)}\left|\frac{x}{2\pi T}\right|^{\nu-1}. \tag{4.34}$$

The above equation shows that when $\nu \neq 1$, the current decays as a function of the applied bias [88] which reflects the underlying power law decay of the transition rates for CLL. Similarly, we can obtain the large bias result for the

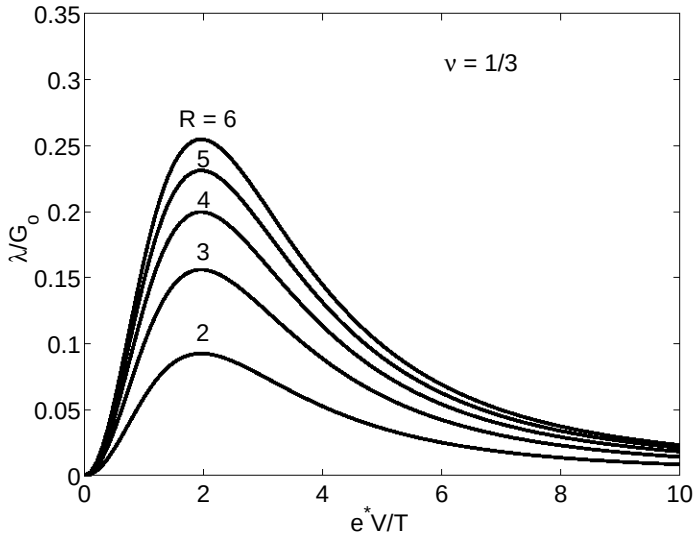

Figure 4.2: The linear response coefficient, in units of $G_o = (e^*)^2\Gamma_1^+(0)/T$, as a function of the applied bias for various values of the tunnel asymmetry parameter R.

current noise,

$$S_I = \frac{e^*I}{2\pi}\left[1 - \frac{2\gamma_1\gamma_2}{(\gamma_1+\gamma_2)^2}\right]. \tag{4.35}$$

This result has the same form as that of the shot noise for resonant tunnelling between two Fermi-Liquid leads [65, 100, 103]. Furthermore, Eq. (4.35) shows that for symmetric tunnel rates $\gamma_1 = \gamma_2$ the shot is suppressed to the value $F = 2\pi(S_I/e^*I) = 1/2$, where F is known as the Fano factor.

In the large bias regime one can obtain a relatively simple expression for the efficiency. Inserting, Eqs. (4.35), (4.33), (4.29) into Eq. (4.18) we have,

$$\eta = \left(\frac{1-\nu}{4\pi\Gamma(\nu)}\right)^2 \frac{(1-R)^2}{1+R^2}\left(\frac{x}{2\pi T}\right)^{2\nu-4}. \tag{4.36}$$

The above result shows that the measurement efficiency falls off for large biases as $\sim (x/2\pi T)^{2\nu-4}$ which implies that this is clearly not the proper regime to operate this as a quantum detector. As shown in Fig. (4.4), the behavior of η is similar to that of the response coefficient and shows that the detector obtains maximum efficiency for relatively small bias voltages, again $e^*V \sim 2T$. Also, due to the fact that η is proportional to the response coefficient this implies that the detector can only operate when there exists some tunnel asymmetry

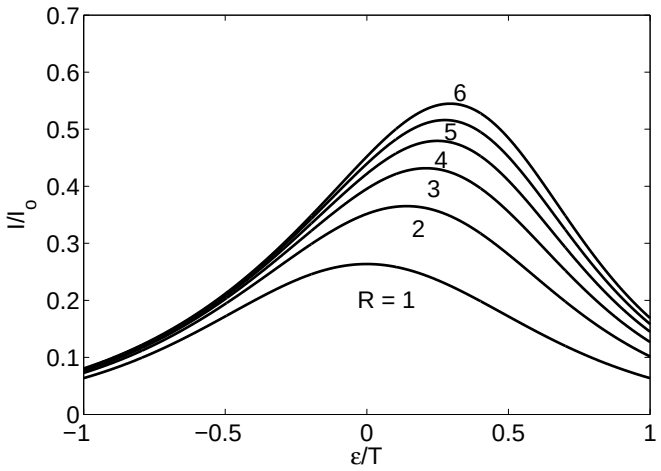

Figure 4.3: The current I, in units of $I_o = e^*\Gamma_1^+(0)$ as a function of the resonant level energy for various values of the tunnel asymmetry parameter R. The parameters for this plot are $T = e^*V$ and $\nu = 1/3$.

between the edges and the antidot, $R \neq 1$.

Similar to the measurement efficiency, an analytical result in the limit of large biases can be found for the energy sensitivity. For this we need the large bias limit of the current-charge noise spectrum, Eq. (4.17). This is given by,

$$\mathrm{Re}\, S_{IQ} = (\gamma_1 - \gamma_2)\, \frac{(e^*)^2}{2\pi} \frac{\gamma_1\gamma_2}{(\gamma_1+\gamma_2)^3}, \tag{4.37}$$

which is independent, in this limit, of the bias and therefore, the CLL behavior of the edges. This yields the energy sensitivity in the large bias limit,

$$\varepsilon = \frac{4\pi T}{\gamma_1} \frac{\Gamma(\nu)}{1-\nu} \frac{\sqrt{2R}}{R^2-1} \left(\frac{x}{2\pi T}\right)^{2-\nu}, \tag{4.38}$$

which diverges when $R = 1$ due to the fact that λ vanishes. This also shows that for large biases, the energy sensitivity scales as $x^{2-\nu}$ and thereby increases when operated in the FQHE regime. This is due solely to the large bias behavior of the response coefficient as both $\mathrm{Re}\, S_{IQ}$ and the product $S_I S_Q$ are independent of ν. The behavior of ε as a function of bias is shown in Fig. (4.5). As in the case of the measurement efficiency, the inverse of energy sensitivity also peaks in the intermediate bias range of $e^*V \sim 2T$. This behavior is again due to the CLL effects of the edges and largely controlled by the response

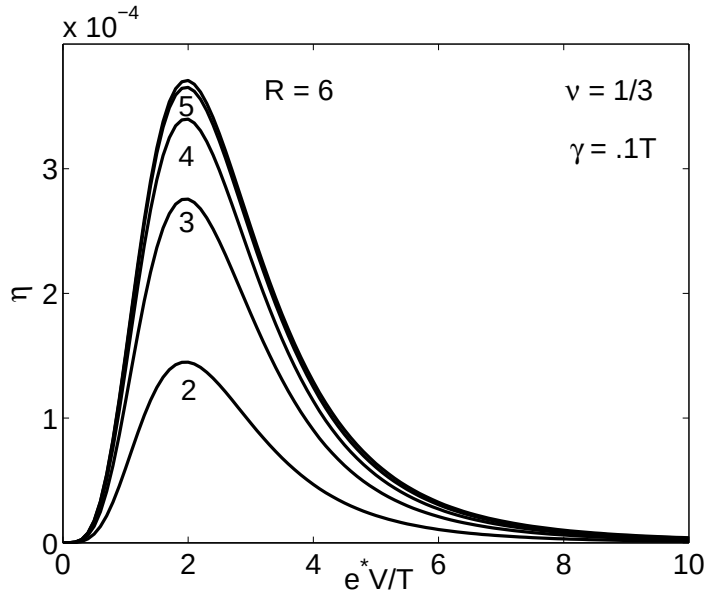

Figure 4.4: The measurement efficiency as a function of the applied bias for different values of the tunnel asymmetry. Note that $\gamma = \gamma_1 + \gamma_2$.

coefficient.

4.3 Conclusions

In conclusion, the measurement characteristics of QAE have been assessed in both the low-temperature (or large-bias) regime, and in case when $\epsilon = 0$. For low temperatures, the CLL properties of the edge states make it possible to tune the QAE (via the back gate voltage) in such a way to make the QAE a symmetric detector. At this bias point the shot noise is minimized. In the case when $\epsilon = 0$, it was shown that both the measurement efficiency and the energy sensitivity of the QAE peak when the bias is $e^*V \sim 2T$. Outside of this regime, η and ϵ exhibit ν dependent power law decays for large biases and vanish quadratically for small biases. The fact that the detectors characteristics peak when operating at this point is due to the CLL behavior of the edge states.

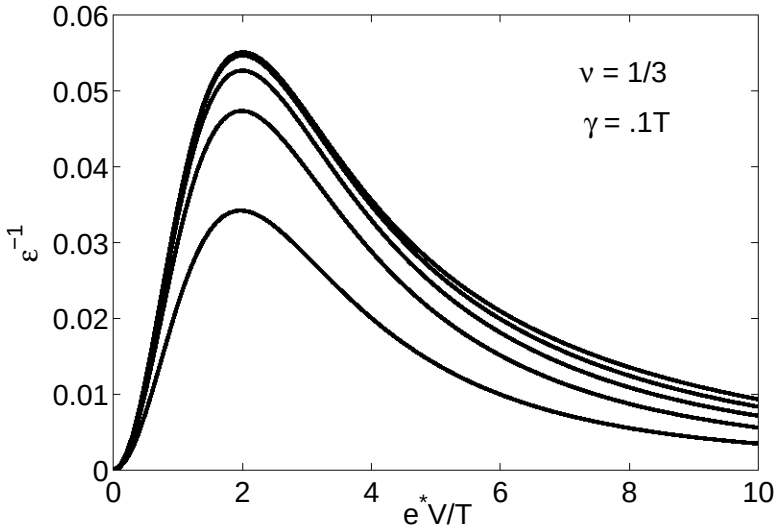

Figure 4.5: The inverse of the energy sensitivity $1/\varepsilon$ plotted as a function of bias. The curves from the bottom up represent the tunnel asymmetries $R = 2, 3, 4, 5, 6$.

Chapter 5

Parametric Oscillations in a Continuously Measured Double Qubit System

The properties of a QAE acting as a linear quantum detector were illustrated in the last chapter. In general, the operation of a linear detector can be summarized as follows: consider two reservoirs (made up of electrons, quasiparticles, cooper pairs, or magnetic flux quanta) coupled by a tunnel barrier. The flux of the particles between the reservoirs is controlled by measured quantum system. A qubit can be coupled to the detector in such a way that the tunnel barrier's amplitude is modulated by the state of the qubit, i.e. $t(\sigma_z)$, where σ_z is the basis-forming variable of the qubit. Since $\sigma_z^2 = 1$, the variation of the amplitude with the state of the qubit can be written as, $t(\sigma_z) = t_o + \delta\sigma_z$. In the case of continuous measurement of a qubit, the spectral density [27] of the detector exhibits a peak at the frequency corresponding to coherent oscillations between the two basis states of the qubit.

Recently, work has been done on so-called quadratic quantum measurements [105–107]. One particular realization of is provided by two qubits coupled to a single detector wherein the tunnel amplitude is modified according to,

$$t(\sigma_z^1, \sigma_z^2) = t_o + \delta_1\sigma_z^1 + \delta_2\sigma_z^2 + \lambda\sigma_z^1\sigma_z^2. \tag{5.1}$$

An example of such a setup is illustrated in Fig. (5.1). Concerning the output spectral density of the detector the second and third terms of the above equation result in spectral peaks at frequencies $\Omega_{1,2}$ and correspond to coherent oscillations in *individual* qubits. The addition of the non-linear coupling term λ gives rise to the existence of spectral peaks occurring at frequencies which are sums and differences of the single qubit resonance frequencies and can be

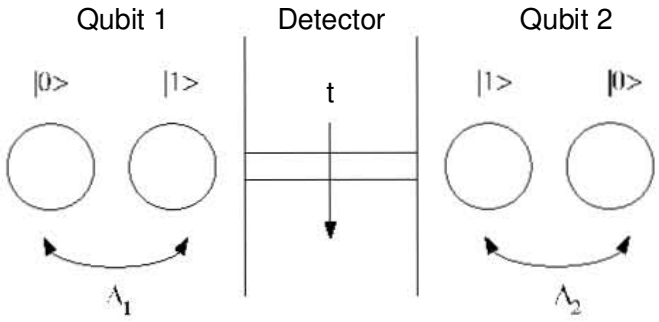

Figure 5.1: Schematic of a generic mesoscopic detector coupled to two qubits. The tunnel amplitude t between the two reservoirs of the detector is modulated by the location of the charges (or flux) in the qubits.

physically interpreted as mixing of oscillations in the qubits. In the case of two non-interacting qubits the Hamiltonian is given by

$$H_Q = \frac{1}{2} \sum_{j=1,2} \left(\epsilon_j \sigma_z^j + \Delta_j \sigma_x^j \right) \tag{5.2}$$

where Δ_j are the tunnel amplitudes between the basis states $\sigma_z|\pm\rangle = \pm|\pm\rangle$ of the qubits and ϵ_j are their biases. The above discussion implies that peaks in the detector output will occur at frequencies $\Omega_{1,2}$ and $\Omega_1 \pm \Omega_2$ with $\Omega_j = \pm \left(\epsilon_j^2 + \Delta_j^2\right)^{1/2}/2$ being the eigenenergies of the j-th qubit. Therefore, the non-linear coupling of the detector to the qubits implies that the oscillations of the two qubits are coupled together in the detector output.

We consider the question of what is the quantum mechanical analogue of the classical parametric interaction between two oscillators. This question can be addressed in the case whereby the oscillation frequency of one qubit is close to being twice that of the other, e.g. $\Omega_2 = \Omega_1/2$. Such a non-linear coupling of two modes of frequency Ω and 2Ω is encountered in classical parametric oscillators. However, the behavior of the two qubit system is quite different from its classical counterpart. The particular choice of parameters for the qubits implies that the spectral peak which represents oscillations occurring in the qubit with the smaller frequency and the peak for the collective oscillations in the two qubits at the frequency $\Omega_1 - \Omega_2$ will overlap. As we will show, not only are these peaks degenerate, but an interference between these two modes of oscillation is setup. This interference can be also controlled by the strength

of the non-linear coupling to the detector.

In the next section we will briefly outline the model used to describe quantum measurements of a coupled qubit system with a mesoscopic detector, a more detailed discussion can be found in Refs. [105, 106].

5.1 Model

Here, we consider the following system consisting of two non-interacting FQHE qubits (albeit the model can easily describe other types of charge or flux based qubits) whose Hamiltonian is given by (5.2). The qubits are continuously monitored by a mesoscopic detector whose tunnel amplitude is modulated by the states of the qubits as in Eq. (5.1). Specifically, this implies that the total Hamiltonian for the system is given by,

$$H = H_D + H_Q + H_T, \tag{5.3}$$

where H_D describes the detector and

$$H_T = t(\sigma_z^1, \sigma_z^2)\xi^\dagger + H.c \tag{5.4}$$

is the detector/qubit system interaction. In this case, particle transfer between the two reservoirs is described by the operator $\xi^\dagger$. This model is applicable to detectors where particles are transferred between reservoirs in a single step. Examples of detectors which fall into this class include, Quantum Point Contacts, DC Superconducting Quantum Interference Devices (SQUIDs), and SETs operating in the cotunnelling regime.

The overall goal is to describe the dynamics of the qubit system. This can be done by deriving the reduced density matrix for this system which is found in a compact form with the help of some assumptions concerning the detector. First, one assumes that the detector is *weakly* coupled to the qubit system and thus H_T can be treated to lowest order in perturbation theory. Furthermore, if the dynamics of particles tunnelling between the reservoirs of the detector is much faster than that of the qubit dynamics then this implies that the measurement dynamics are described by the correlators,

$$\gamma_+ = \int_0^\infty d\tau \langle \xi(\tau)\xi^\dagger(0)\rangle \qquad \gamma_- = \int_0^\infty d\tau \langle \xi^\dagger(\tau)\xi(0)\rangle \tag{5.5}$$

which also describe the rate of forward and backward transitions between the reservoirs of the detector i.e. $\Gamma_\pm = 2\,\mathrm{Re}\,\gamma_\pm$. Finally, it is important to point out that the fast dynamics of the detector also implies that the tunnel time

between the reservoirs is much smaller than the temporal evolution of the measured system. In the case of a Quantum Point Contact this tunnel time is set by the bias energy eV between the two reservoirs meaning and therefore should be much larger that the energy largest energy scale of the qubit-system for the correlators (5.5) to hold.

The evolution of the density matrix is most easily expressed in the limit where the detector induced dephasing rates are small in comparison to the eigen energies E_n of the qubit system (5.2). In this approximation scheme, the equations for the diagonal elements of the qubit system density matrix evolve as,

$$\dot{\rho}_{nn} = -\gamma \sum_{p \neq n} |\hat{t}_{np}|^2 \left(\rho_{nn} - \rho_{pp}\right), \tag{5.6}$$

where $\gamma = (\Gamma_+ + \Gamma_-)$ represents damping induced in the qubit system due to the coupling to the detector and n is the index of the eigenstate of the qubit system, $H_Q|n\rangle = E_n|n\rangle$. On the other hand, the off-diagonal elements of the density matrix behave according to,

$$\dot{\rho}_{nm} = -\left(i\omega_{nm} + \kappa_{nm}\right)\rho_{nm} + \sum_{(p,q)} \rho_{pq}\, \mathrm{Re}(\hat{t^\dagger}_{np}\hat{t}_{qm}), \tag{5.7}$$

where,

$$\kappa_{nm} = \frac{\gamma}{2}\left(\left|\hat{t}_{mm} - \hat{t}_{nn}\right|^2 + \sum_{p \neq m}\left|\hat{t}_{mp}\right|^2 + \sum_{p \neq n}\left|\hat{t}_{np}\right|^2\right) \tag{5.8}$$

is the dephasing caused by coupling to the detector, and $\omega_{nm} = E_n - E_m$. The summation in the third term of Eq. (5.7) is over the eigenstates of the qubit system satisfying the resonance condition $E_n - E_m = E_p - E_q$, such that $(n, m) \neq (p, q)$.

The important quantity we want to compute is the spectral density of the equilibrium current fluctuations of the detector-qubit system, $S(\omega)$ which are given by,

$$S(\omega) = S_o + 2\int_0^\infty dt \cos\omega t \left(\langle I(0)I(t)\rangle - \langle I\rangle^2\right), \tag{5.9}$$

where the current correlator is given by,

$$\langle I(0)I(t)\rangle = \mathrm{Tr}\left[Ie^{Lt}\left[I\rho_o\right]\right]. \tag{5.10}$$

Here, $I = (\Gamma_+ - \Gamma_-)\,\hat{t^\dagger}\hat{t}$ is the operator that describes the detector current due to the coupling to the qubits, ρ_o is the steady-state solution to Eqs. (5.6), and $e^{Lt}\left[I\rho_o\right]$ is the evolution operator for the density matrix of the reduced

detector-qubit system undergoing the evolution described by Eqs. (5.6) and (5.7). The first term in (5.9) represents the shot and thermal noise of tunnelling through the detector,

$$S_o = \gamma \,\mathrm{Tr}\left[t^\dagger t \rho_o\right]. \tag{5.11}$$

In the next section, we calculate the spectral density of the detector output specifically in the case when $\Omega_2 \approx \Omega_1/2$.

5.2 Results

Before delving into the peak structure of the output current spectrum we will give explicit expressions for the eigenvalues and eigenvectors of the two qubit Hamiltonian (5.2), as these will be needed for the calculations. In the case of $\epsilon_{1,2} = 0$ and $\Delta_2 = \Delta_1/2$, the energies and associated eigenvectors are,

$$E_{1,2} = \pm\frac{3\Delta_1}{4} \qquad |1,2\rangle = \frac{1}{2}\left[|\phi_1^+\rangle \mp |\phi_2^+\rangle\right] \tag{5.12}$$

$$E_{3,4} = \pm\frac{\Delta_1}{4} \qquad |3,4\rangle = \frac{1}{2}\left[|\phi_1^-\rangle \pm |\phi_2^-\rangle\right] \tag{5.13}$$

where we have defined $|\phi_1^\pm\rangle = (|++\rangle \pm |--\rangle)$ and $|\phi_2^\pm\rangle = (|+-\rangle \pm |-+\rangle)$.

In order to calculate the spectral density we note that the evolution of the current operator in the correlation function Eq. (5.10) is governed by the time evolution of the density matrix for the qubit system. Therefore, the matrix elements of the current operators obey the same dynamical equations as (5.6) and (5.7) with the initial condition,

$$I_{ij}(0) = I_{ij}\left[\rho_o\right]_{jj}. \tag{5.14}$$

The steady-state density matrix of the qubit system is found by solving for the stationary solution to the density matrix equations (5.6) and (5.7). As expected, the detector completely decoheres the system and therefore the off-diagonal elements vanish. Solving for the diagonal elements yields the stationary solution,

$$\rho_o = \hat{I}/4 \tag{5.15}$$

where $\hat{I}$ is the identity matrix. This implies that the detector acts as an infinite temperature heat bath and thus completely mixes the eigenstates of the qubit system.

5.2.1 Peak structure for $\omega = \Delta_1$ and $\omega = \Delta_1 + \Delta_2$

The first case to consider is the peak that occurs at the frequency $\omega \approx 3\Delta_1/2$. This corresponds to transitions between the states $|1\rangle$ and $|2\rangle$ and represents collective oscillations in the two qubits occurring at the frequency $\Delta_1 + \Delta_2$. Using (5.7) the matrix elements of the current operator evolve according to,

$$\dot{I}_{12}(t) = -(\kappa + i\Omega_+)I_{12}(t) \tag{5.16}$$

where, $\Omega_+ = 3\Delta_1/2$. The above equation shows that the matrix elements of the current operator between the two eigenstates exhibit damped oscillations at the frequency corresponding to transitions between parallel and anti-parallel configurations of the two qubits. The damping of these oscillations is due to the coupling of the qubit system to the detector. The spectral density at this frequency can be found by inserting the solution to Eq. (5.16) and its complex conjugate into the expression for the current noise Eq. (5.9) which gives,

$$S(\omega) = S_o + \frac{1}{4}\frac{2a_2^2\kappa}{(\omega - 3\Delta_1/2)^2 + \kappa^2}, \tag{5.17}$$

where $a_2 = 2(\Gamma_+ - \Gamma_-)\,\mathrm{Re}(t_0\lambda^* + \delta_1\delta_2^*)$ represents the amplitude of collective qubit oscillations [105, 106] and $\kappa = \Gamma(|\delta_1|^2 + |\delta_2|^2 + |\lambda|^2)$. Therefore, we see from the above equation that the spectral peak located at $3\Delta_1/2$ is described by a simple Lorentzian with amplitude $a_2/2\kappa$ and width given by κ.

The spectral peak at $\omega \approx \Delta_1$ can be found in a similar way to the previous case. Here, however, the energy spectrum of the qubit system is such that transitions between states 1 and 4 as well as 3 and 2 all occur at the same frequency, namely Δ_1. Thus, the density matrix equations can be found to be,

$$\dot{I}_{14}(t) = -(\kappa + \imath\Delta_1)I_{14} + \Gamma|\delta_2|^2 I_{32} \tag{5.18}$$

$$\dot{I}_{32}(t) = -(\kappa + \imath\Delta_1)I_{32} + \Gamma|\delta_2|^2 I_{14}. \tag{5.19}$$

We find that the spectral density is,

$$S(\omega) = S_o + \frac{1}{4}\frac{4a_{11}^2\kappa_1}{(\omega - \Delta_1)^2 + \kappa_1^2}, \tag{5.20}$$

where $\kappa_{1,2} = \Gamma\left(\lambda^2 + \delta_{1,2}^2\right)$ is the width of the peak and $a_{11} = 2(\Gamma_+ - \Gamma_-)\,\mathrm{Re}(t_o\delta_1^* + \lambda\delta_2^*)$. This peak represents oscillations which occur between the basis states of the qubit with the larger energy splitting. At resonance, the peak has an amplitude given by a_{11}^2/κ_1.

5.2.2 Peak structure for $\omega = \Delta_1/2$

We now turn our attention to the final peak in the output spectrum of the detector. Here, there are three separate energy intervals which satisfy the resonance condition equality, $E_i - E_j = \Delta_2 = \Delta_1/2$. We can then write the evolution equations for the matrix elements of the current operator as,

$$\begin{aligned}
\dot{I}_{34} &= -(\imath\Delta_2 + \kappa)I_{34} + \Gamma\,\mathrm{Re}(\lambda^*\delta_2)I_{42} + \Gamma\,\mathrm{Re}(\lambda^*\delta_2)I_{13} && (5.21)\\
\dot{I}_{42} &= -(\imath\Delta_2 + \kappa)I_{42} + \Gamma\,\mathrm{Re}(\lambda^*\delta_2)I_{34} + \Gamma|\delta_1|^2 I_{13} && (5.22)\\
\dot{I}_{13} &= -(\imath\Delta_2 + \kappa)I_{13} + \Gamma\,\mathrm{Re}(\lambda^*\delta_2)I_{34} + \Gamma|\delta_1|^2 I_{42}, && (5.23)
\end{aligned}$$

where $\Gamma = (\Gamma_+ + \Gamma_-)$. The equations for the resonance condition, $E_i - E_j = -\Delta_1/2$, are the complex conjugates of the previous equations. As was done in all other cases, the output spectrum can be obtained by finding the solution to Eqns. (5.21)-(5.23) combined with the above stated initial conditions into the expression for the current density. Instead of presenting the full result we will instead, for the sake of clarity, discuss a few particular limiting cases. The first case concerns the limit where the non-linear coupling of the qubits to the detector λ vanishes. By inspection of the dynamical equations one sees that these are of the same form as those contributing to the spectral peak at $\omega \approx \Delta_1$, see Eqns. (5.18) and (5.19). Therefore, the peak at $\omega \approx \Delta_1/2$ corresponds to coherent oscillations between the basis states of the smaller qubit and has the same form as (5.20),

$$S(\omega) = S_o + \frac{1}{4}\frac{4a_{12}^2\kappa_2}{(\omega - \Delta_1/2)^2 + \kappa_2^2}, \tag{5.24}$$

with $a_{12} = 2\,(\Gamma_+ - \Gamma_-)\,\mathrm{Re}[t_0^*\delta_2 + \lambda^*\delta_1]$ representing the amplitude of oscillations in the smaller qubit.

The next limit to explore is the case where the linear coupling of the larger qubit to the detector vanishes, $\delta_1 \to 0$. By inspection of the dynamical equations one sees that here both collective oscillations between the two qubits and oscillations occurring in the qubit of smaller frequency are directly coupled to one another. This coupling of the two oscillatory modes has interesting consequences for the composition of the spectral peak. In particular, the solutions to Eqs. (5.21)-(5.23) are given by,

$$\begin{aligned}
I_{34}(t) &= \frac{e^{-i\Delta_2 t}}{8}\left[\sqrt{A_1}e^{-\gamma_1 t} + \sqrt{A_2}e^{-\gamma_2 t}\right] && (5.25)\\
I_{42}(t) &= \frac{e^{-i\Delta_2 t}}{4\sqrt{8}}\left[\sqrt{A_1}e^{-\gamma_1 t} - \sqrt{A_2}e^{-\gamma_2 t}\right], && (5.26)
\end{aligned}$$

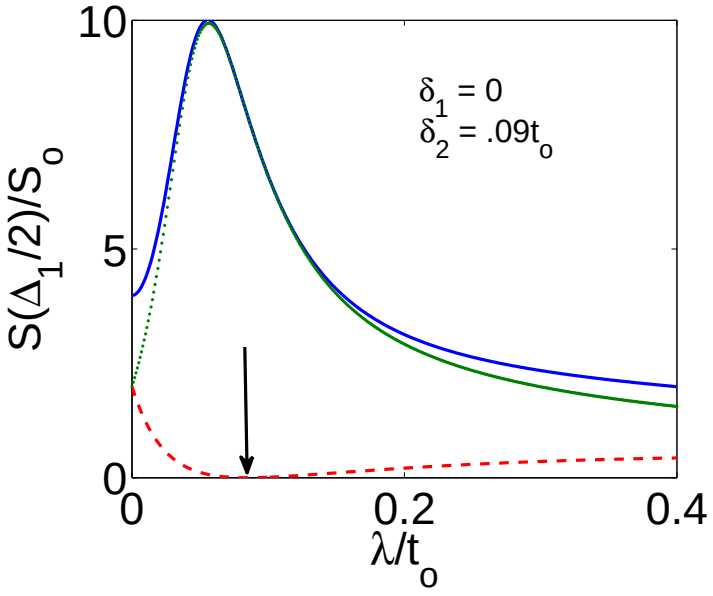

Figure 5.2: The maximum of the detector output spectrum (solid line) at $\omega \approx \Delta_1/2$ as a function of λ. This has two contributions: one corresponding to constructive interference between collective and single qubit oscillations with amplitude $A_1/(4\gamma_1)$ (dotted) and the other represents destructive interference (dashed) having an amplitude $A_2/(4\gamma_2)$. The arrow indicates the point at which A_2 vanishes.

and $I_{13}(t) = I_{42}(t)$. Here, we have defined

$$A_m = \left[a_2 + (-1)^{m+1}\sqrt{2}a_{12}\right]^2 \qquad \gamma_m = \kappa + (-1)^m\alpha, \tag{5.27}$$

with $\alpha = \sqrt{2}\Gamma\,\mathrm{Re}(\lambda\delta_2^*)$. The time dependence of the current matrix elements shows that oscillations between the parallel and antiparallel configurations of the two qubits, $I_{34}(t)$ as well as single qubit transitions, $I_{42}(t)$ and $I_{13}(t)$ have the same frequency. However, the main difference between the two modes lies in the fact that they decay at different rates, as can be seen by inspecting the bracketed expressions of Eqs. (5.25) and (5.26) and that their amplitudes are different. Using these expressions we then find that the resulting spectral peak is given by

$$S(\omega) = S_o + \frac{1}{4}\sum_{m=1,2}\frac{A_m\gamma_m}{(\omega - \Delta_1/2)^2 + \gamma_m^2}. \tag{5.28}$$

Here, we see a rather unique situation with has thus far not been encoun-

tered in any of the other peaks which we have studied. While the spectral peak consists of two overlapping Lorentzians, the amplitudes of those peaks exhibit, constructive A_1 and destructive A_2 interference between the single qubit and collective oscillations. This effect can be traced back to the coupling of these modes found in the time evolution of the matrix elements of the current operator.

An interesting consequence of this interference between the two oscillatory modes is that by varying either δ_2 or λ, the strength of the interference can be controlled. In order to study this behavior we will look at the peak's maximum, $S(\Delta_1/2)$. Here we assume that the detector is ideal which implies that $\Gamma_- = \arg(t_0\lambda) = \arg(t_o\delta_2) = 0$. First, consider the case when $\lambda = 0$. Here, both amplitudes are the same $A_m = 2a_{12}^2$ and therefore the maximum is given by $4S_o$. This result is characteristic of ideal linear detectors and represents the maximum signal to noise ratio allowed by quantum mechanics. For finite λ the two contributions to the spectral peak behave quite differently, as illustrated in Fig. (5.2).

Let us first look at the case where the $m = 2$ contribution vanishes. Here, this implies by an inspection of Eq. (5.27) that $a_2 = \sqrt{2}a_{12}$. When the detector is ideal this occurs whenever the strength of the non-linear coupling to the detector is such that $\lambda_1 = \sqrt{2}\delta_2$. This condition also implies that the maximum of the $m = 1$ term in Eq. (5.28) reaches a height of $2a_{12}^2/\gamma_1$, where $\gamma_1 = \Gamma(\delta_2^2)$. The reason for this is directly related to the modal interference. In the absence of this, the degeneracy of the single qubit and difference frequencies implies that the peak should obtain a maximum height of $6S_o$, which is the sum of the linear and non-linear contributions. However, the interference between these two modes adds an additional factor of $2\sqrt{2}a_2a_{12}/\gamma_1$ whose height when $\lambda = \lambda_1$ is given by $2S_o$.

Finally, as shown in Fig. (5.2) the peak height can be made even larger and maximizes at a value of approximately $10S_o$. To understand the origin for this we note that the dominant contribution to the maximum stems from the $m = 1$ term in Eq. (5.28). Maximizing this with respect to λ we find that $S(\Delta_1/2) = 10S_o$ which occurs at $\lambda_2 = 4\delta_2/(3\sqrt{2})$. More insight into the reason for this peak height can be gained by investigating the evolution of the current matrix elements, Eq. (5.25) and (5.26). The assumption that A_2 is vanishingly small implies that all matrix elements have the same damped oscillatory behavior given by γ_1. However, this particular choice of λ means that $\gamma_1 = 10\kappa_2/18$. The important point to note is that the damping rate of these oscillations is nearly two times smaller than in the previous case. This implies that the width of the spectral peak when λ is chosen to be λ_2 should narrower than at λ_1, as is shown in Fig. (5.3). Furthermore, one

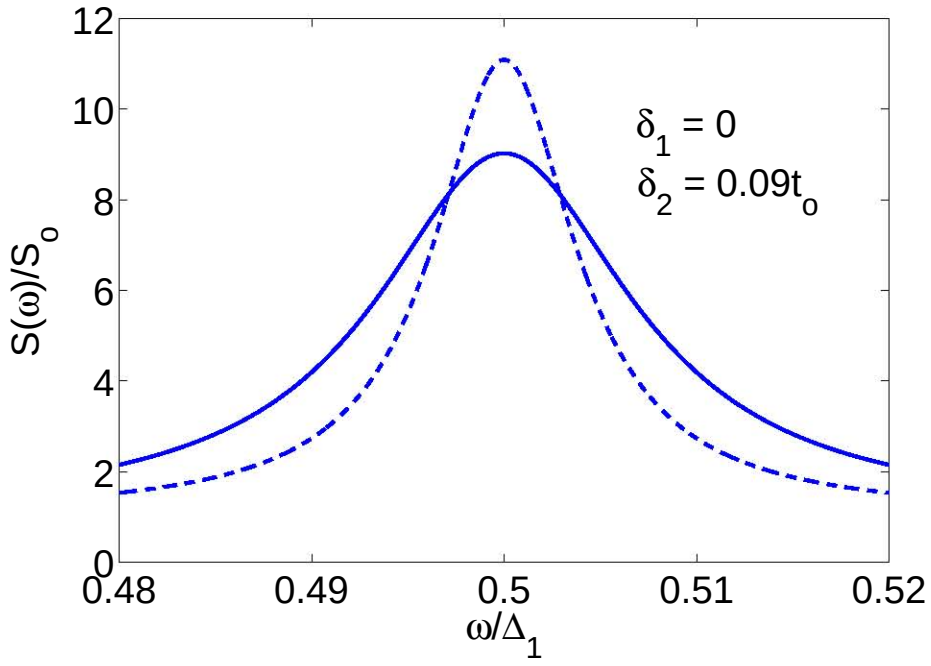

Figure 5.3: The spectral peak for $\lambda = \lambda_1$ (solid) and $\lambda = \lambda_2$ (dashed) about $\omega = \Delta_1/2$.

would expect that based on this fact alone the peak height at λ_2 should be approximately $16S_o$. However, tuning the non-linear coupling to this point reduces the amplitude by about two-thirds of its height at λ_1.

The last case to explore is the influence of a non-vanishing linear coupling to the larger qubit δ_1. A solution of the dynamical equations reveals that the spectral peaks can be written in the same form as Eq. (5.28) with the amplitudes and widths of the Lorentzians given by,

$$A_m = a_2^2 + 2a_{12}^2 + (-1)^{m+1} 2\sqrt{2} a_2 a_{12} \cos(\theta) \tag{5.29}$$

$$\gamma_m = \kappa - \beta + (-1)^m \Omega \tag{5.30}$$

where we have defined $2\beta = \Gamma|\delta_1|^2$, $\Omega = \sqrt{\alpha^2 + \beta^2}$, and $\cos(\theta) = \alpha/\Omega$. Qualitatively, the main effect of finite δ_1 is reduce the overall coupling between the single qubit and collective oscillations. As a result maximum height that the spectral peak can obtain is reduced with increasing δ_1 as illustrated in Fig. (5.4).

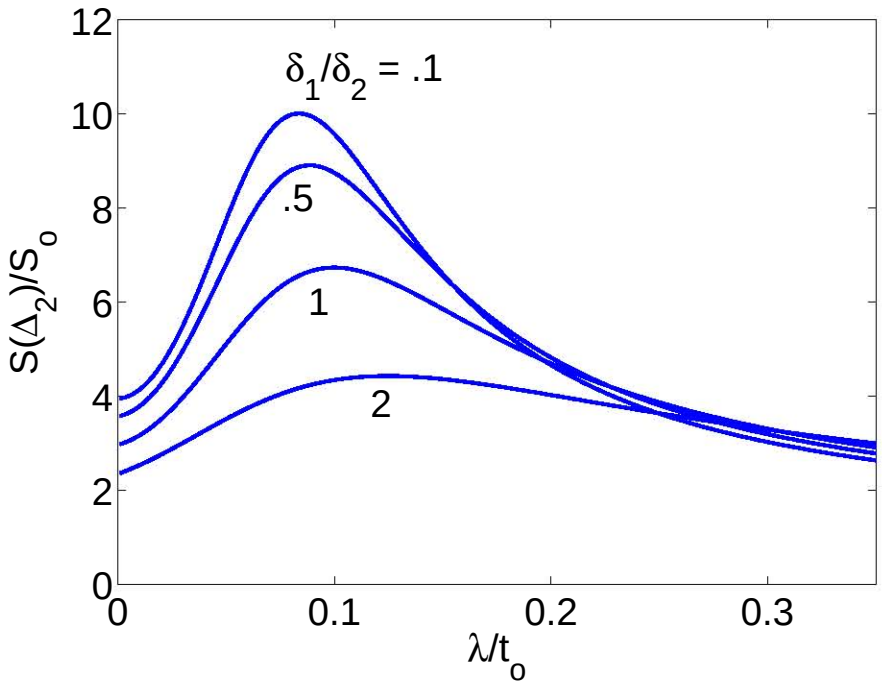

Figure 5.4: $S(\Delta_2)$ in units of S_o for various values of δ_1. Here, we assume that as before $\delta_2 = .09t_o$.

5.3 Conclusions

In this chapter we have studied a system of two non-interacting, unbiased, qubits coupled non-linearly to an ideal detector. The focus of the analysis was on the regime in which the tunnel amplitude between the basis states of one qubit is twice that of the other. This particular bias point allows for the coherent coupling of two distinct oscillatory modes: ones which occur between the basis states of the "weaker" qubit with the smaller oscillation frequency and that which represents collective oscillations between the qubits occurring at the difference frequency, $\Delta_1 - \Delta_2$. Furthermore, we have shown that the strength of the non-linear coupling between the detector and qubit system controls both the interference between the modes and their damping rate. When this interference is maximized, the spectral peak at $\omega \approx \Delta_1/2$ has a maximum peak height of approximately $10S_o$, which is well above the quantum limited detection threshold for linear detectors.

Chapter 6

Tunnelling without Tunnelling: Wave Function Reduction in a Mesoscopic Qubit

In Chapter 4, the implementation of a Quantum Antidot electrometer as a readout device for qubits based on antidots was discussed. In what follows we demonstrate that the developed theory of a Quantum Detector can be used to study the some of the unusual properties of the quantum measurement process. In particular, we consider the following question: Can a quantum mechanical particle tunnel through an infinitely high barrier? From the point of view of unitary evolution based on the Schrödinger equation the immediate answer to this question is no. However, a careful consideration of the situation reminds us that this is not the only way in which a quantum mechanical system can evolve. The probabilistic nature of the wave function implies that evolution can also take place via "wave function reduction".

In its most basic form, wave function reduction is the random process of realizing one specific outcome of a measurement and was initially envisaged as completely suppressing quantum coherences described by the wave function. It was understood, however, later (see, e.g, [108–111]) that this is not true in the case of "morally best" [109–111] or, in more modern and descriptive language, quantum-limited measurements, in which the wave function of the measured system changes coherently for any given outcome of the measurement. These changes can contradict the Schrödinger equation despite the fact that the measurement process as a whole is governed by this equation. They can be described formally as generic "quantum operations" within the approach based on positive operator-valued measures (POVM) [112]. All "counter-intuitive" quantum-mechanical phenomena arise from such an evolution of the wave function in the measurement process. The best known

example is given by the EPR correlations [113] which violate the principle of "no action at-a-distance" as quantified by the Bell's inequalities [114]. From the perspective of the wave-function reduction, the EPR correlations appear for a specific random outcome of the local spin measurement. On average, the measurement does not create action-at-a-distance in a sense that the correlations do not violate the relativistic causality.

More recently, the process of wave-function reduction was described quantitatively [62, 115] for mesoscopic solid-state qubits measured with practical scattering detectors [116]. This process underlies "temporal" Bell inequalities [117–120] which characterize quantum uncertainty in the qubit state in the process of coherent quantum oscillations between the two macroscopically distinct configurations.

The purpose of this work is to suggest a sequence of quantum transformations and the corresponding Bell-type inequality which would demonstrate this uncertainty in a more direct way, by violating intuition which is based on wave evolution governed by the Schrödinger equation. For mesoscopic structures with their small geometric dimensions, violation of this intuition provides, arguably, more dramatic illustration of the wave-function reduction than the non-locality of conventional Bell's inequalities discussed, e.g., in [121–123].

6.1 Model

We begin by considering a single qubit with the two basis states given by $|j\rangle$, with $j = 1, 2$ coupled to a detector, a typical setup of this is shown in Fig. 1. These states differ by some amount of magnetic flux or an individual elementary charge (i.e. electron, Cooper-pair, or an FQHE quasiparticle), which are localized on either side of a tunnel barrier. The barrier couples these states and has a tunnel amplitude $\Delta > 0$. When the qubit operates at its resonance point, where the relative bias ϵ between the two basis states vanish, the Hamiltonian describing this system is then given by

$$H = -v\sigma_z - \Delta\sigma_x \tag{6.1}$$

where, $\sigma_{x,z}$ are the Pauli matrices. The additional bias energy v represents the low frequency noise inherent in both charge and flux qubits. We model this noise by assuming that v is a random variable that is Gaussian distributed with amplitude v_o and stationary in time.

Initially, due to assumed weak, but unavoidable, relaxation processes the

qubit is in the ground state of (6.1),

$$\rho = \begin{pmatrix} |c_1|^2 & c_1 c_2 \\ c_2 c_1 & |c_2|^2 \end{pmatrix}, \tag{6.2}$$

where, the probability amplitudes $c_{1,2}$ are given by the relations $c_{1,2}^2 = (1 \pm v/\Omega)/2$, with $\Omega^2 = v^2 + \Delta^2$. The transformation cycle begins by rapidly raising the tunnel barrier, $\Delta \to 0$, so that the qubit is "frozen" in the state (6.2).

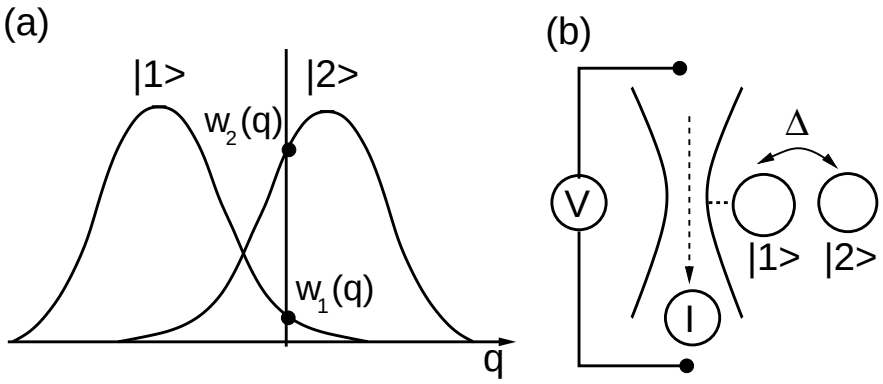

Figure 6.1: (a) The probability distributions $w_j(q)$ of a given detector output q, when the qubit is in the state $|j\rangle$, $j = 1, 2$. (b) A schematic of one particular way of realizing a qubit measurement using a QPC detector. The two qubit states $|j\rangle$ are localized on the opposite sides of a tunnel barrier and, in general, are coherently coupled by tunnelling across this barrier with coupling strength Δ. The flow of the current I through the QPC is driven by the applied voltage V and plays the role of the detector output. Transfer of the qubit charge between the states $|j\rangle$ changes the scattering amplitudes for the QPC electrons incident on the constriction.

The next step in the process is to perform a partial measurement of the σ_z operator on the initial state (6.2), which we will describe next.

6.1.1 Wave Function Reduction

Quantitatively, we can describe this process from the point of view of conditional evolution of the wave function. This involves specifying the probability $w_j(q)$ of obtaining an output q from the detector when the state of the qubit is $|j\rangle$. In the simplest case, these probabilities can be assumed to be two Gaussian peaks of width σ that are separated by a distance $2\Delta q$. Increasing the separation of the peaks results in a stronger measurement. The result of

the measurement yields some information about the state of the qubit and is then used to update the probability amplitudes of the initial wave function [62, 115],

$$c_j(q) \to \frac{c_j\sqrt{w_j(q)}}{\sqrt{w_1(q)|c_1|^2 + w_2(q)|c_2|^2}}. \tag{6.3}$$

The above equation shows that specifying the detector output increases the degree of localization in the σ_z basis because of information provided by the measurement; a process which is distinctly different from that of the unitary Schrödinger-equation-based evolution. It is important to note that the above evolution leaves the system in a pure state even though the detector, as a matter of principle, introduces back-action dephasing to the system. In the case of a quantum-limited, detector this dephasing arises due to the averaging over all possible measurement outcomes.

For non-ideal detectors additional dephasing is introduced into the system causing further loss of information. Taking into account the detector non-ideality, one can write the state of the qubit after measurement as

$$\overline{\rho} = \begin{pmatrix} \overline{\rho}_{11}(q) & \overline{\rho}_{12}(q)e^{-\gamma+2\imath v\tau_m/\hbar} \\ \overline{\rho}_{12}(q)e^{-\gamma-2\imath v\tau_m/\hbar} & \overline{\rho}_{22}(q) \end{pmatrix}, \tag{6.4}$$

where, $\overline{\rho}_{jj}(q) = |c_j(q)|^2$ and $\overline{\rho}_{12}(q) = \overline{\rho}_{21}(q) = c_1(q)c_2(q)$. The degree of the detector non-ideality is characterized by the parameter γ which vanishes for an ideal detector. The phase factor in the off-diagonal elements takes into account the evolution of the system under the influence of the noise for a period of time τ_m before, during, and after the measurement.

The aim of the remaining steps of the cycle is to reverse the shift in the tunnel amplitudes caused by the partial measurement. This is accomplished by creating a non-vanishing tunnel amplitude for some appropriate period of time. In other words, realizing a fraction of the regular coherent oscillations in which the charge or flux oscillates between the qubit basis states.

6.1.2 Transformation Cycle

Consider, first, the case of vanishing noise $v = 0$ and an ideal detector. Here, the transformation is complete in the sense that the state of the qubit after measurement (6.4) will be returned to its initial form (6.2). The most direct way to implement this is if the qubit structure is such that the tunnel amplitude $\Delta'(t)$ can acquire a non-vanishing phase (e.g. in superconducting qubits, where the tunnel amplitude is controlled via quantum interference, can have any complex value). A transformation from the state (6.4) directly to

(6.2) can be readily accomplished by making $\arg \Delta' = \pi/2$. In the diagram (Fig. 2a) in which the qubit states are represented in the language of spin-1/2, such a tunnel amplitude corresponds to a rotation about the y axis. The diagram shows then directly that the angle of rotation turning $\overline{\rho}$ into ρ should have the magnitude:

$$\int |\Delta'(t)| dt/\hbar = (\pi/2 - \theta)/2 \ , \qquad \theta = \tan^{-1}(\lambda), \tag{6.5}$$

where $\lambda = \sqrt{w_2(q)/w_1(q)}$.

In a more typical situation when the qubit structure allows only for the real tunnel amplitude Δ, the y-axis rotation $R_y = \exp\{-i\sigma_y \int |\Delta'(t)| dt/\hbar\}$ (6.5) can be simulated if the rotation $R_x = \exp\{i\sigma_x \int \Delta(t) dt/\hbar\}$ around the x axis of the same magnitude (6.5) is preceded and followed by the rotations around the z-axis: $R_y = R_z^{-1} R_x R_z$, where the z-rotation $R_z = \exp\{i\sigma_z \pi/4\}$ can be created by the pulses of the qubit bias: $\int \epsilon(t) dt/\hbar = \pm\pi/4$. Such a three-step sequence can be simplified into two steps (Fig. 2b) by changing the order of rotations: first, the x-rotation by $\pi/4$ followed by one z-rotation:

$$\int \Delta(t) dt/\hbar = \pi/4 \, , \qquad \int \epsilon(t) dt/\hbar = (\pi/2 - \theta)/2 \, . \tag{6.6}$$

To take into account noise in the transformation cycle, we note that the time in between each pulse is in general finite. For the case of the two-step cycle, we model the noise by adding an additional noise induced rotation $U = \exp\{iv\tau_R \sigma_z/\hbar\}$ where τ_R is the total time elapsed before and after the z axis rotation. We have assumed that the applied pulses are short and the effect of the noise during the rotations is negligible.

6.2 Results

In the case of vanishing noise, all of the transformations bring the measured state of the qubit back to its initial state, where $\sigma_x = -1$. In all cases the completion of the cycle that started with a shift of the wave function amplitudes due to the state reduction involves part of a period of coherent oscillations that reverses this shift. However, coherent oscillations are known to actually transfer the charge or flux between the two basis states. Thus, because the cycle as a whole is closed, this fact shows that the changes in the qubit state caused by wave function reduction can not be interpreted only as the changes in our knowledge of the probabilities of the state of the qubit, but involves an actual transfer of charge or flux in the absence of the tunnelling amplitude.

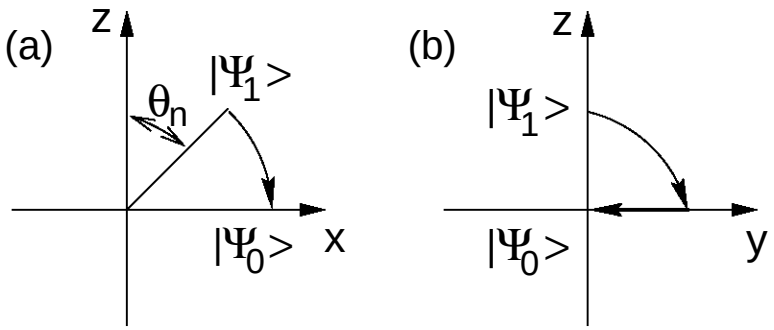

Figure 6.2: Diagram of the two possible transformations of the qubit state $|\psi_1\rangle$ into $|\psi_0\rangle$ after the measurement-induced state reduction $|\psi_0\rangle \to |\psi_1\rangle$: (a) direct one-step y-axis rotation (6.5); (b) projection on the $z-y$ plane of the two-step transformation (6.6).

To see this more quantitatively, one can derive the Bell-type inequality, a violation of which should show that understanding of the state reduction solely in terms of the probability changes can not be correct. The inequality is obtained by assuming that the process of switching off the tunnelling amplitude Δ in the beginning of the cycle does not lead to the state (6.2) but localizes the qubit in one of the basis states, i.e., produces an incoherent mixture of the qubit basis states with some probability p to be in the state $|1\rangle$. This process would provide then an alternative, classical description of the evolution during the measurement process, in which the qubit state is "objectively" well defined and coincides with one of the basis states. It is, however, unknown to us and the measurement gradually provides information about this unknown state. A convenient way of comparing such a classical description with quantum evolution is provided by the probability of reaching the wrong final state, in this case $\sigma_x = -1$.

In what follows, we will determine the probability of reaching the state $\sigma_x = -1$ for both the quantum and classical evolution under the influence of both low-frequency noise and detector non-ideality, in order to assess the stability of the cycle under these more realistic conditions. We start from the case when the phases accumulated during both the measurement and rotation cycle can be removed. In principle this can be accomplished, for example, by employing a spin echo technique, and is equivalent to setting $\tau_{M,R} = 0$.

In the case of classical evolution the probability $p^{(-)}$ to find the qubit in the state $\sigma_x = -1$ can be found by applying the transformation sequence to the incoherent state with the initial density matrix now given by $\rho = p|1\rangle\langle 1| + (1-p)|2\rangle\langle 2|$. The measurement part of the cycle acts as follows: for a detector

output q the probability changes as

$$p \to pw_1(q)/(pw_1(q) + (1-p)w_2(q)). \tag{6.7}$$

Applying the same transformations as to the state (6.2), one sees that the probability $p^{(-)}(q)$ of ending up in the state $\sigma_x = -1$, given the measurement outcome q, is

$$p^{(-)}(q) = w_1(q)w_2(q)/[(w_1(q) + w_2(q))(pw_1(q) + (1-p)w_2(q))]. \tag{6.8}$$

The final step involves averaging over all possible measurement outcomes q, $p^{(-)} = \int \sigma(q)p^{(-)}(q)dq$. Note that the detector non-ideality does affect the measurement outcome as the off-diagonal elements of the initial state were assumed to vanish. The probability of obtaining an outcome from the detector during the measurement process $\sigma(q)$ is given by

$$\sigma(q) = w_1(q)\rho_{11} + w_2(q)\rho_{22}, \tag{6.9}$$

where ρ_{jj} are the initial probabilities for the system to be in the state j. For the classical case these are simply $\rho_{11} = p$ and $\rho_{22} = 1 - p$. Finally we find,

$$p^{(-)} = \int dq \frac{w_1(q)w_2(q)}{w_1(q) + w_2(q)}. \tag{6.10}$$

Equation (6.10) shows that the probability of classical evolution to end up in the wrong state is finite and independent of the initial probability p. Furthermore, the expression is general in the sense that it is given only in terms of the probabilities that are characteristic of the detector and therefore could apply to any type of quantum measurement device.

Turning to the quantum evolution, the probability $p(\sigma_x = -1)$ of ending up in the state $\sigma_x = -1$ is found by applying the transformation sequence to the measured state (6.4). Next, the average is taken over both the noise and the measurement outcome. To average over the outcome we can use Eq. (6.9) but with ρ_{jj} corresponding to the diagonal elements of the initial state (6.2). This yields:

$$p(\sigma_x = -1) = p^{(-)} \left[1 - \sqrt{\frac{2\alpha}{\pi}} e^{\alpha} K_o(\alpha)\, e^{-\gamma} \right], \tag{6.11}$$

where $K_0(x)$ is the modified Bessel function of the second kind and $\alpha = \Delta^2/(4v_0^2)$. The second expression in the bracket corresponds to the off-diagonal matrix elements of (6.2) after averaging over the noise, with the factor $e^{-\gamma}$ describing the additional dephasing caused by a non-ideal detector. Consider

first the limit of strong noise, $\alpha \to 0$. In this case, the noise completely dephases the state (6.2) and thus, $p(\sigma_x = -1) \approx p^{(-)}$. In the opposite limit of vanishing noise, Eq. (6.11) reduces to $p(\sigma_x = -1) = p^{(-)}(1 - e^{-\gamma})$. When the detector is ideal ($\gamma = 0$), we see that the transformation cycle completely returns the qubit back to $\sigma_x = 1$, whereas for non-ideal detectors, there is always a non-vanishing probability of end up in the wrong state. Therefore, in order to distinguish quantum coherent evolution from that which is incoherent, it is necessary to have a detector which operates close to the quantum limited regime, $\gamma \ll 1$, and noise which is weak enough so that the initial state is not completely dephased, as illustrated in Fig. 6.3. Furthermore, one must employ weak measurement, i.e. if one of the probabilities $w_j(q)$ is zero, the measurement is projective implying that $p(\sigma_x = -1) = p^{(-)} = 0$ and therefore impossible to distinguish the two types of evolution. This conclusion should be independent of the specific form of the employed transformation cycle, since projective measurement is always expected to fully separate different components of the initial state of the measured system and completely suppress quantum coherence between them.

The discussion above means that observation of the probability of the state $\sigma_x = -1$ smaller than $p^{(-)}$,

$$p(\sigma_x = -1) < p^{(-)} \tag{6.12}$$

at the end of the transformation cycle proves that all transformations in this cycle, including the wave function reduction, are quantum coherent. Combined with the non-vanishing transfer of charge or flux during the "oscillation" step [(6.5), (6.6)] of the cycle, this fact implies that the wave function reduction induces similar transfer across the tunnel barrier separating the qubit basis states even if the corresponding tunnel amplitude is zero.

6.3 Conclusions

The purpose of this Chapter was to investigate the counter-intuitive properties of wave function reduction. More specifically, we considered a qubit subject to low-frequency noise measured by some general mesoscopic detector. A series of quantum transformations and associated Bell-type inequality were suggested to illustrate the possibility that charge or flux can be transferred between two states separated by an infinitely high barrier. Moreover, we have shown that such an effect is relatively robust against both detector non-ideality and the low-frequency environmental noise present in state-of-the-art qubit systems.

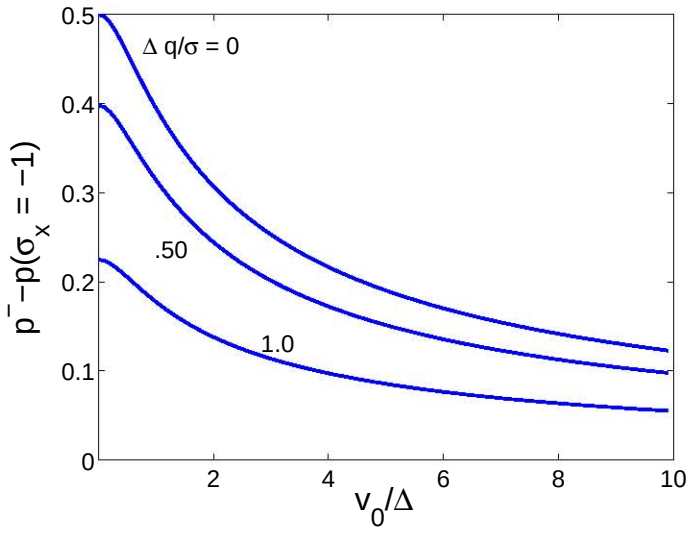

Figure 6.3: The difference between the classical and quantum "error" probabilities, Eqns. (6.10) and (6.11) respectively, plotted as a function of the noise amplitude v_o/Δ for an ideal detector $\gamma = 0$ for various values of the measurement strength $\Delta q/\sigma$.

Chapter 7

Landau-Zener Transitions and Decoherence in Adiabatic Quantum Computation

7.1 Introduction

In this chapter, we turn our attention to a different paradigm in the field of quantum information, namely that of Adiabatic Quantum Computation. As was mentioned in Chapter one, AQC involves an adiabatic transformation of the ground state Hamiltonian H_S of a qubit register in order to perform computations. One begins by preparing the system in the ground state of a known initial Hamiltonian H_i and slowly evolves the system towards some final Hamiltonian H_f, the ground state of which represents the solution to the problem. The most important restriction is that the evolution must occur slowly enough so that the system remains as close as possible to the instantaneous ground state of the total Hamiltonian H_S.

In general, the performance of an adiabatic algorithm depends on the structure of the energy spectrum of H_S. In this work, we will consider the situation which is typical for complex problems involving both search and optimization [124] where the performance is limited by the anti-crossing of the two lowest energy levels of the system. In the vicinity of the anti-crossing the problem is mapped to the usual Landau-Zener problem.

The classic Landau-Zener (LZ) [125–127] problem concerns non-adiabatic transitions in a two level system with a linearly time dependent potential. The Hamiltonian for such a case is given by

$$H_o(t) = \frac{1}{2}\left(vt\sigma_z + \Delta\sigma_x\right), \tag{7.1}$$

where $\sigma_{x,z}$ are the Pauli matrices, v is known as the sweep rate, and Δ is the coupling between the eigenstates $|\pm\rangle$ of σ_z. The instantaneous or adiabatic energies of (7.1) are given by, $E_{\pm}(t) = \pm(1/2)\sqrt{(vt)^2 + \Delta^2}$ and form an avoided crossing with an energy gap given by $g_m = \Delta$, as shown in Fig. 7.1. The time dependent problem can be solved exactly [125–127] and its evolution

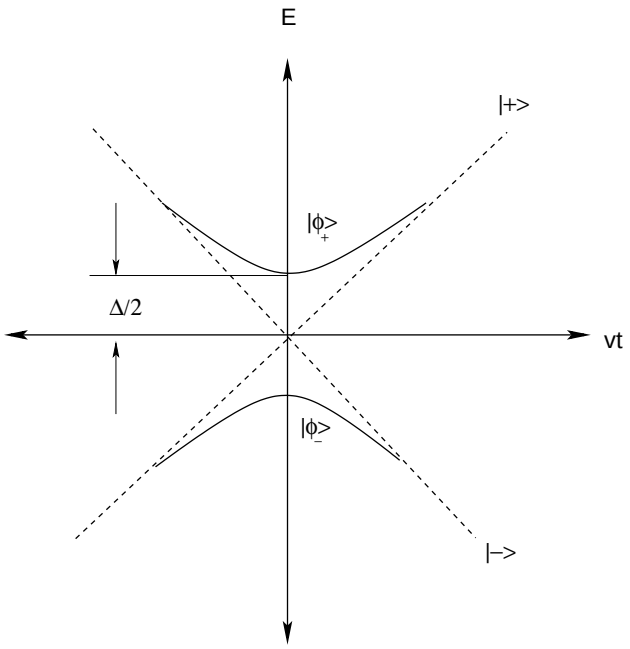

Figure 7.1: Energy levels of the Hamiltonian (7.1) as a function of vt. The solid lines correspond to the adiabatic energies while the dashed correspond to the diabatic energies, $E_d(t) = \pm vt$. Note that in the limit when $vt \gg \Delta$ the two energies coincide.

from $t = [-\infty, \infty]$, in the adiabatic basis of (2.1), is given by

$$U(\infty, -\infty) = \begin{pmatrix} \exp(-\imath\Phi)\sqrt{q_{LZ}} & -\sqrt{p_{LZ}} \\ \sqrt{p_{LZ}} & \exp(\imath\Phi)\sqrt{q_{LZ}} \end{pmatrix}. \tag{7.2}$$

Here

$$p_{LZ} = \exp\left(-\pi\Delta^2/2v\right) \tag{7.3}$$

represents the LZ-probability to make a transition across the adiabatic states and $q_{LZ} = 1 - p_{LZ}$. Finally, Φ is known as the Stokes' phase and is given by

$$\Phi = \pi/4 + \arg\Gamma(1 - \imath\delta) + \delta(\ln\delta - 1) \tag{7.4}$$

where, $\delta = \Delta^2/2v$ and $\Gamma(z)$ is the Gamma function.

In the limit when $\delta \ll 1$, Eq. (7.2) shows that $p \approx 1$. This implies that if the system is initially ($t = -\infty$) prepared in the ground state it will then transit very nearly unimpeded across the energy gap. However, in the opposite limit $\delta \gg 1$, $p \to 0$, and thus throughout the entire evolution the system remains close to the instantaneous ground state $|\phi_-\rangle$.

One of the main advantages that this scheme offers for quantum computation is the protection against environmentally induced decoherence. This is due to the energy gap that exists between the ground and excited states of H_S. It is also important to point out that it allows for the ground state to maintain its coherence properties for times which are much longer than that of single qubit without benefit of ground state protection. For the two state approximation, this particular feature of AQC remains intact, as has been previously demonstrated in Ref. [124], even if the temperature and/or decoherence strength are much larger than the energy gap. However, one question that can be immediately raised is how does decoherence affect the performance of an AQC algorithm? This question has particular relevance when it comes to discussing the practical implementation of AQC of which one particularly promising approach is to utilize solid state qubits.

In light of the above discussion one needs to understand what happens when the Hamiltonian describing LZ transitions given in (7.1) is coupled to some environmental system. The simplest case one can imagine is when $H_o(t)$ is coupled to an environment H_B consisting of a single two level system,

$$H = H_o(t) + H_B + \lambda\sigma_x\tau_x \qquad H_B = \frac{W}{2}\tau_z, \tag{7.5}$$

where $\tau_{x,z}$ are the Pauli matrices describing the environment, λ is the coupling strength, and W is the energy splitting of the environmental spectrum. As shown in Fig. 7.2(b) the two level crossing splits into four anti-crossings whose energy gaps are modified by the coupling λ to the environment. An environment with a continuous spectrum turns the anticrossing point into a continuous region of some width W (Fig. 7.2c) within which incoherent tunnelling between the two qubit states can take place. Thus for such typical models of the environment, the gap no longer exists in the "qubits+environment" system. The broadening W is directly related to the decoherence time of the qubit states. Any uncertainty W in the energy of an energy eigenstate makes the accumulated phase of this state also uncertain in time $\tau_{\rm decoh} \sim 1/W$. Since the broadening W typically increases with the number of qubits, while the minimum gap g_m decreases, any realistic large-scale system will eventually fall into the incoherent regime $W \gg g_m$. This means that studies of the adiabatic

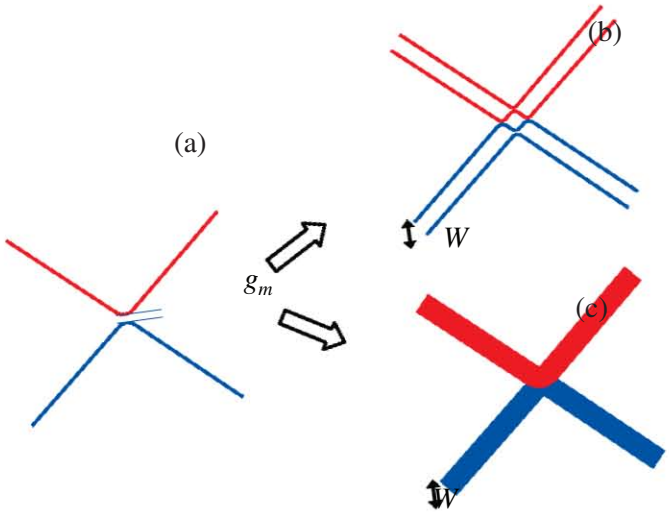

Figure 7.2: Broadening of the energy levels of a closed system (a) due to coupling to an environment made of (b) a single two-state system, or (c) infinitely many degrees of freedom with a continuous energy spectrum. In general, the coupling to an environment splits a single anticrossing into M^2 anticrossings where M is the number of environment energy eigenstates. For the environment with a continuous spectrum, the anticrossing turns into a continuous transition region of width W.

theorem do not apply to such *realistic* situations and therefore new ways of understanding the performance of AQC become necessary.

This chapter is dedicated to pursuing two interrelated topics. In the next section we study Landau-Zener transitions coupled to a simple environment. In particular, our interest will focus on the modification to the LZ transition probability when $H_o(t)$ is coupled to an environment consisting of a single harmonic oscillator. In this system only coherent transitions between the various energy levels can take place which leads to a dramatic modification of the LZ probability. We will also show how the phase accumulated during non-adiabatic transitions (e.g. the Stokes' phase) through the energy gaps leads to interference effects which appear, for example, in the qubit's transition probability. These effects, known as Stückelberg oscillations, have been recently observed in solid state qubits [128, 129].

In the second part of this chapter, we study the evolution of an adiabatic quantum computer in the "incoherent" regime by developing a corresponding description of Landau-Zener transitions for $W \gg g_m$ [130].

7.2 Landau-Zener transitions in a coupled qubit-oscillator system

In this section we investigate the coupling of a qubit undergoing Landau-Zener Transitions to an environment consisting of a single harmonic oscillator. Aside from the understanding garnered by exploring non-adiabatic transitions in this type of system, a secondary motivation concerns its experimental relevance particularly in the field of circuit quantum electrodynamics (CQED) [28, 29]. In analogue to cavity QED where atoms interact with quantized electromagnetic fields, superconducting charge [28] or flux [29] qubits play the role of atoms that are strongly coupled to a quantized harmonic oscillator which is embedded in the circuit. Recently, work has been done towards studying LZ transitions in these types of systems (see for example [131–133]) including proposals for utilizing LZ transitions to generate single photons at microwave frequencies [133] and to create [132] an entanglement of the qubit-oscillator states. However, studies thus far focus on the case when the oscillator is at zero temperature. In what follows we will show how coupling the qubit to an oscillator initialized in a thermal state will lead to the modification of the LZ transition probability as well as to the appearance of Stückelberg oscillations which could be experimentally observed in CQED systems.

7.2.1 Model

The model considered in this section follows the recent work done on LZ transitions in CQED systems [131–133] and is characterized by,

$$H(t) = \frac{vt}{2}\sigma_z + \Omega a^\dagger a + \frac{\Delta}{2}\sigma_x + \frac{\lambda}{2}\sigma_x\left(a^\dagger + a\right) \tag{7.6}$$

where Ω is the frequency of the oscillator and λ is the coupling strength between the two systems. In experimental applications both the energy sweep rate v and the tunnel coupling Δ can be tuned. The diabatic states of this system, i.e. those which diagonalize the first two terms of (7.6), are given by $|n,\pm\rangle = |\pm\rangle \otimes |n\rangle$ where $|\pm\rangle$ are the eigenstates of σ_z and $|n\rangle$ are the energy eigenstates of the harmonic oscillator. The associated diabatic energies are,

$$E_n^{\pm}(t) = \pm\frac{vt}{2} + \Omega n. \tag{7.7}$$

In the calculations that follow we will assume that initially, the combined qubit-oscillator system starts out in the state described by the density matrix

$$\rho(t \to -\infty) = |+\rangle\langle+| \otimes \rho_{osc}, \tag{7.8}$$

where

$$\rho_{osc} = \sum_n \rho_n |n\rangle\langle n|. \tag{7.9}$$

Here $|n\rangle$ are the eigenstates of the oscillator with energy $E_n = \Omega n$ and ρ_n is the occupation probability of the state $|n\rangle$. In the case of a thermal distribution of oscillator states, $\rho_n = e^{-\beta\Omega n}/Z$ with $\beta = 1/T$ and $Z = \sum_m e^{-\beta\Omega m}$ is the partition function.

The quantity of primary interest is the survival probability of the qubit, or the probability that once initialized in the state $|+\rangle$ that at $t \to \infty$ the qubit will remain in that state. For an isolated qubit, i.e. setting $\lambda = 0$ in (7.6), this is simply the LZ transition probability given in (7.3). For non-vanishing coupling the survival probability is found evolving the system from $t = -\infty$ to $t = \infty$ beginning with the state (7.8) and summing over all the oscillator states. This is given by,

$$P_{surv} = \sum_{m,n} \rho_n |\langle m, +|U(\infty, -\infty)|n, +\rangle|^2 \tag{7.10}$$

where $U(\infty, -\infty) = T\exp[-i\int_{-\infty}^{\infty} H(t')dt']$ and T is the usual time ordering. The above equation implies that the survival probability for the qubit is simply a sum over all possible transitions between states $|n_+\rangle$ and $|m_+\rangle$ weighted by the occupation probability of the state $|n_+\rangle$ which in turn is determined by the temperature T of the oscillator.

Due to the complexity of the system Hamiltonian (7.6) a full analytical result for the survival probability is not possible. However, in the following discussions we will be able to find analytical results in various limiting cases.

7.2.2 Survival Probability when $\Delta = 0$

In this we consider the case in which the coupling between the basis states of the qubit Δ vanishes. Then the Hamiltonian (7.6) reduces to,

$$H(t) = \frac{vt}{2}\sigma_z + \Omega a^\dagger a + \frac{\lambda}{2}\sigma_x(a^\dagger + a). \tag{7.11}$$

The energy spectrum of the system as a function of vt is shown schematically in Fig. 7.3. The effect of the final term in (7.11) is to couple the diabatic states

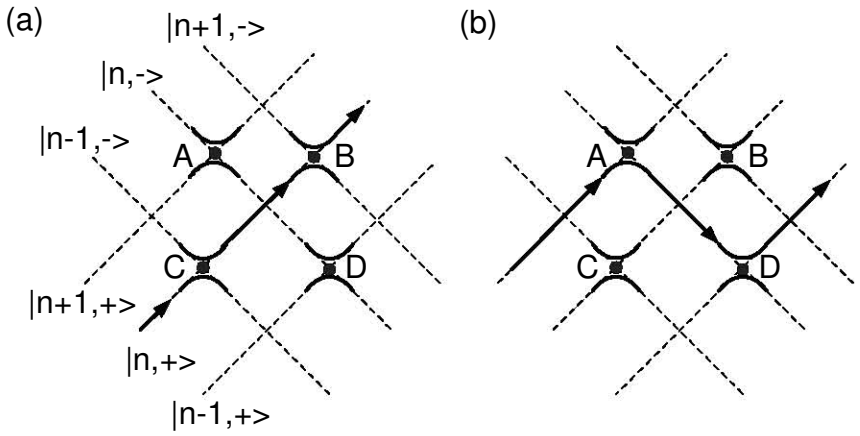

Figure 7.3: Energy diagram illustrating the anticrossings (solid lines) between the different diabatic energy levels (dashed lines) of the Hamiltonian (7.11). In the limit when the width of the anti-crossings are smaller than the separation between consecutive diabatic energy levels (which is Ω) transitions between the crossings can occur independent of one another. In this case, there are two possible paths that contribute to P_{surv}: (a) direct transitions which begin and end on the same diabatic state and (b) indirect transitions which go between $|n+1,+\rangle$ and $|n-1,+\rangle$.

$|n,+\rangle$ and $|n\pm 1,-\rangle$ and therefore causes the energy spectrum to exhibit anti-crossings between these states whenever $t = \pm\Omega/v = \pm t_o$.

In the limit when $\lambda \ll \Omega$, the avoided crossings are well separated from one another. To calculate transition amplitudes between the diabatic states we can then employ the independent crossing approximation (ICA) [134]. Under the ICA, due to separation of the avoided crossings, the dynamics of the system near the vicinity of an anticrossing can be well described by the standard two level Landau-Zener problem and each crossing is treated as independent of all others. This is illustrated in Fig. 7.4 near the crossing between two diabatic energy levels, $|n,+\rangle$ and $|n+1,-\rangle$. At their intersection, the adiabatic energies form an avoided crossing with an energy gap given by $\Delta E_n = \lambda\sqrt{n+1}$. Around the anti-crossing, the propagator in the adiabatic basis is given by

$$U_n(\infty,-\infty) = \begin{pmatrix} \exp(-\imath\Phi_n)\sqrt{q_n} & -\operatorname{sgn}(\lambda)\sqrt{p_n} \\ \operatorname{sgn}(\lambda)\sqrt{p_n} & \exp(\imath\Phi_n)\sqrt{q_n} \end{pmatrix}. \tag{7.12}$$

Here, $p_n = e^{-\pi\delta_n}$ and $q_n = 1 - p_n$ represent the probabilities to make a transition or to remain in the adiabatic state respectively, and $\delta_n = \Delta E_n^2/2v$.

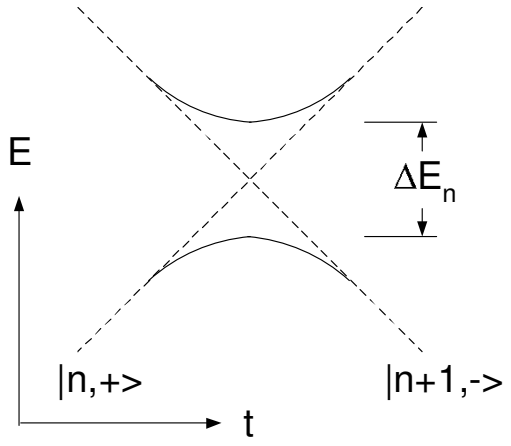

Figure 7.4: Energy diagram of the anti-crossing between two diabatic energy levels (dashed) and the corresponding adiabatic energy levels (solid).

The Stokes' phases are given by

$$\Phi_n = \frac{\pi}{4} + \arg\Gamma\left(1 - i\delta_n\right) + \delta_n\left(\ln\delta_n - 1\right). \tag{7.13}$$

Note also that transitions between states $|n,+\rangle$ and $|n-1,-\rangle$ are given by Eqns. (7.12) and (7.13) with $n \to n-1$.

Next, we turn our attention to determining the survival probability for the qubit using Eq. (7.10). Utilizing Eq. (7.10) the survival probability can be written as a sum of two separate contributions,

$$P_{surv} = P_0 + P_2 \tag{7.14}$$

where,

$$P_0 = \sum_{n=0} \rho_n |\langle n,+|U(\infty,-\infty)|n,+\rangle|^2 \tag{7.15}$$

corresponds to direct transitions which begin and end on the same diabatic state, as illustrated in Fig. 7.3a. The other term P_2 corresponds to transitions between diabatic states with the emission of two photons wherein the system begins in the state $|n+1,+\rangle$ and ends up in $|n-1,+\rangle$, in Fig. 7.3b. This is

given by,

$$P_2 = \sum_{n=2} \rho_n |\langle n-2, +|U(\infty, -\infty)|n, +\rangle|^2. \tag{7.16}$$

The fact that the survival probability separates into two separate terms is a direct result of the σ_x coupling of the qubit to the oscillator. It is important to note that transitions to states of higher energies (eg. transitions between states $|n, +\rangle$ and $|m, +\rangle$ where $E_m^+ > E_n^+$) are forbidden since the crossings must proceed forward in time. The fact that transitions from states of lower to higher energy are forbidden is a general feature of multilevel (LZ) problems and is known as the "no-go" theorem [134–137] whose validity is independent of the width of the level crossing. The "no - go" theorem has also been applied recently to dissipative LZ transitions [131, 138].

The direct transitions can be easily calculated using the ICA,

$$|\langle n, +|U(\infty, -\infty)|n, +\rangle|^2 = p_{n-1} p_n \tag{7.17}$$

which is simply the product of the transition probabilities across the individual anti-crossings located at points B and C in Fig. 7.3a. Inserting this result into Eq. (7.15) and summing over all the oscillator states yields,

$$P_0 = e^{-\frac{\pi\lambda^2}{4v}} \frac{\sinh(\beta\Omega/2)}{\sinh(\beta\Omega/2 + \pi\lambda^2/4v)}. \tag{7.18}$$

As one can see from the above equation in the limit when the oscillator is at zero temperature then $P_d = \exp(-\pi\lambda^2/2v)$ which is simply the LZ transition probability to make a transition at the anti-crossing between the states $|0, +\rangle$ and $|1, -\rangle$. In fact, it has been shown that this result holds even when the ICA fails (see e.g. Refs. [131, 133, 134, 138]). For non-vanishing temperatures, Eq. (7.18) shows that in the limit adiabatic limit when $v \ll \lambda^2$, the transition probability decays to zero.

The indirect transition rates can be found in the same way and are given by,

$$P_2 = e^{-2\beta\Omega} \left[1 - P_d \sinh\left(\frac{\beta\Omega}{2}\right) F(\beta, \lambda)\right] \tag{7.19}$$

where,

$$F(\beta, \lambda) = \frac{P_d}{\sinh\left(\frac{\beta\Omega}{2} + \frac{\pi\lambda^2}{2v}\right)} - \frac{\sinh\left(\frac{\pi\lambda^2}{4v}\right)}{\sinh\left(\frac{\beta\Omega}{2} + \frac{\pi\lambda^2}{4v}\right)}. \tag{7.20}$$

One of the most important observations to make about Eq. (7.19) concerns its behavior in the adiabatic limit, $v \ll \lambda^2$. In this case, P_2 does not vanish but in fact asymptotically approaches a temperature-dependent value of $\exp(-2\beta\Omega)$.

Qualitatively, the main reason for this can seen by inspecting indirect transition path in Fig. 7.3b. Consider the case where the system begins in the state $|n+1,+\rangle$. The first anti-crossing that the system approaches is at the point A in the figure. Since the probability of transiting across the gap is goes as $e^{-\pi\lambda^2(n+2)/2v}$, in the adiabatic limit, any transition will be strongly suppressed. Therefore, the system will adiabatically evolve along the lower energy level of the crossing and end up in the state $|n,-\rangle$. At the next crossing, located at point D, transitions across the gap are again exponentially suppressed and thus the system will end up in the state $|n-1,+\rangle$. So, in the adiabatic limit, $|\langle n-1,+|U(\infty,-\infty)|n+1,+\rangle| \to 1$ up to irrelevant phase factors. Since the survival probability is the sum of both direct and indirect transitions this will approach the value $\exp(-2\beta\Omega)$ in the adiabatic limit. In Fig. 7.5, the behavior

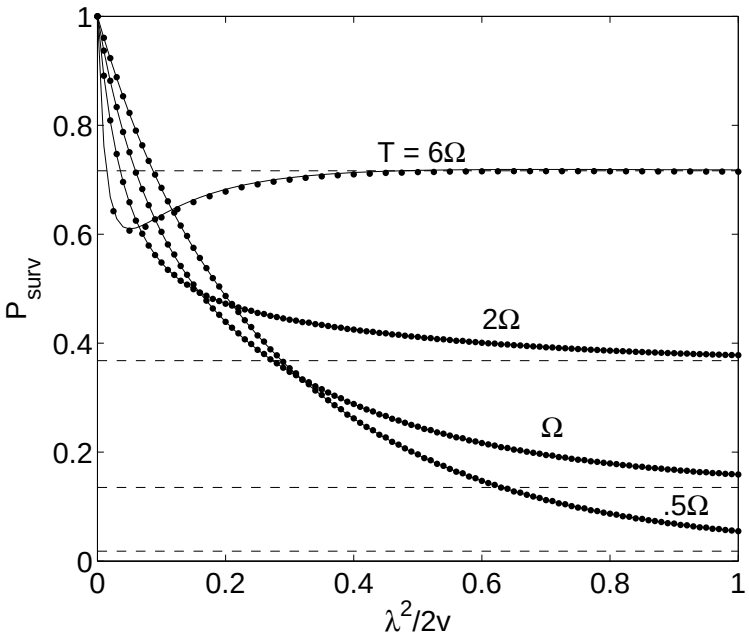

Figure 7.5: Survival probability as a function of $\lambda^2/2v$ for various oscillator temperatures. The dotted lines are obtained by a numerical solution of the propagator in Eq. (7.10) with $\lambda = .02\Omega$ and the solid lines are the survival probability found using the ICA.

of the survival probability is shown as a function of $\lambda^2/2v$ for various values of the temperature. The dotted lines shown in Fig. 7.5 compare the results obtained from the numerical evaluation of the propagator in Eq. (7.10) to the ICA. For comparison λ, has been set to $.02\Omega$ and shows excellent agreement

with the results obtained from the ICA.

7.2.3 Survival Probability when $\Delta \neq 0$

The next step in the analysis is to consider the case when Δ is non-vanishing and $\Delta, \lambda \ll \Omega$ so that the ICA applies. In this case, the possibility exists that non-adiabatic transitions between states of the same photon number but with different "spin", that is transitions between the diabatic states $|n,+\rangle$ and $|n,-\rangle$. As will be shown, this simple modification to the Hamiltonian has rather interesting consequences for the survival probability.

In the case of $\Delta \neq 0$, the survival probability (7.10) has three different contributions to it at finite oscillator temperature,

$$P_{surv} = P_0(\Delta) + P_2(\Delta) + P_1(\Delta), \tag{7.21}$$

where the first and second terms of the above equation have the same form as Eqns. (7.15) and (7.16), respectively, and

$$P_1(\Delta) = \sum_{n=1} \rho_n |\langle n-1,+|U(\infty,-\infty)|n,+\rangle|^2, \tag{7.22}$$

corresponds to transitions between diabatic states which have the same qubit state but differ by one photon.

Consider first, the calculation of the propagators contributing to $P_0(\Delta)$,

$$|\langle n,+|U(\infty,-\infty)|n,+\rangle|^2 = p_{n-1} p_n p_{LZ} \tag{7.23}$$

where, p_{LZ} is the LZ probability given in Eq. (7.3) and corresponds to the transition across the anti-crossing connecting the diabatic states $|n,\pm\rangle$. Since this is independent of the oscillator state, the contributions to the survival probability at finite temperature from direct transitions can be related to those in the case of vanishing Δ as $P_0(\Delta) = p_{LZ} P_0$, where P_0 is given by Eq. (7.23).

Similarly, the contributions from $P_2(\Delta)$ are also related in the same way as $P_2(\Delta) = p_{LZ} P_2$. This implies that in the adiabatic limit when $\Delta \gg v$, the survival probability no longer saturates but decays asymptotically toward zero as transitions across the energy gap between the diabatic states $|n,\pm\rangle$ are exponentially suppressed.

Finally, we turn our attention to the calculation the contribution stemming from Eq. (7.22). To calculate the propagator, $S_n = |\langle n-1,+|U(\infty,-\infty)|n,+\rangle|^2$, we note that there exists two paths to go from $|n,+\rangle$ to $|n-1,+\rangle$, with amplitudes $S^n_{1,2}$, as shown in Fig. 7.6. Therefore,

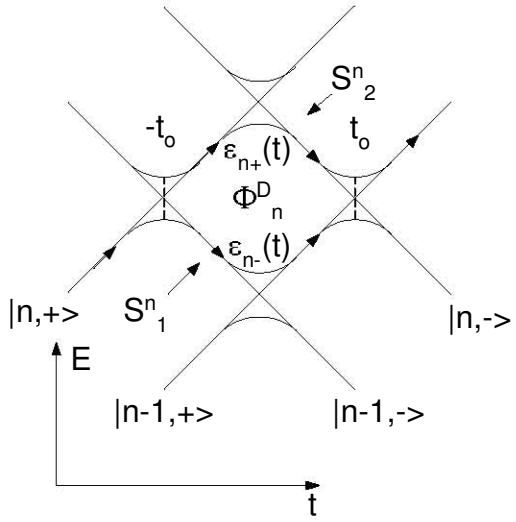

Figure 7.6: Energy level diagram for one photon transitions. The crossings of the diabatic states occur at $t = \pm\Omega/v, 0$. As indicated by the arrows there are two possible paths whose amplitudes are $S^n_{1,2}$ connecting the states $|n,+\rangle$ and $|n-1,+\rangle$. The dynamical flux, Φ^D_n, is the area enclosed by the adiabatic states of the Hamiltonian (7.11), $\epsilon_{n\pm}(t)$, between the diabatic crossings at $\pm\Omega/v$.

$$S_n = |S^n_1|^2 + |S^n_2|^2 + 2\,\mathrm{Re}(S^n_1 \bar{S}^n_2) \tag{7.24}$$

where $\bar{S}$ denotes the complex conjugate of the amplitude. By utilizing the propagator given by Eq. (7.12), we can then calculate the amplitudes of each path by taking the product of transition amplitudes at each crossing. These are given by,

$$S^n_{1,2} = -\Theta_{\lambda,\Delta}\sqrt{q_{n-1}p_{n-1}q_{LZ}}\,e^{\imath\left(\Phi^D_{1,2}(n)+\chi^{n-1}_{1,2}\right)}. \tag{7.25}$$

Here we have defined $\Theta_{\lambda,\Delta} = \mathrm{sgn}(\lambda)\,\mathrm{sgn}(\Delta)$. The quantities $\Phi^D_{1,2}(n)$ are the dynamical phases accumulated as the system evolves along the adiabatic eigenstates $\epsilon_{n\pm}(t)$ of the Hamiltonian (7.6) and $\chi^{n-1}_{1,2}$ correspond to the Stokes' phases picked up at each crossing whenever the system makes a transition between two diabatic states. These are given by $\chi^{n-1}_1 = \Phi - \Phi_{n-1}$ and $\chi^{n-1}_2 = -\chi^{n-1}_1$. Thus, Eq. (7.24) becomes,

$$S_n = 4q_{n-1}p_{n-1}q_{LZ}\cos^2\left(\frac{\phi_{n-1}}{2}\right), \tag{7.26}$$

where $\phi_{n-1} = \Phi^S_{n-1} - \Phi^D_n$ and represents the total flux enclosed by the adiabatic energies $\epsilon_{n\pm}(t)$ between the two crossing points $\pm t_o$. This has two contributions, one from the Stokes' phases, given by $\Phi^S_{n-1} = \chi_1^{n-1} - \chi_2^{n-1}$, and the other from the dynamical phase [139],

$$\Phi^D_n = \int_{-t_o}^{t_o} dt \left[\epsilon_{n+}(t) - \epsilon_{n-}(t)\right]. \tag{7.27}$$

The combined action of both phase contributions controls the interference between the between the paths $S^n_{1,2}$ and leads to oscillations in the survival probability of the qubit, when the oscillator is at a finite temperature. These are the well known Stuckelberg Oscillations. Finally, inserting Eq. (7.26) into (7.22) yields,

$$P_1(\Delta) = 8q \sinh\left(\frac{\beta\Omega}{2}\right) \sum_{n=1} q_{n-1} p_{n-1} \cos^2\left(\frac{\phi_{n-1}}{2}\right) e^{-(n+1/2)\beta\Omega}. \tag{7.28}$$

To understand the above equation further, consider the survival probability of the qubit in the low temperature limit ($T \ll \Omega$). Here, to good approximation, it is only necessary to consider the occupancy of ground and first excited state of the oscillator system. The energy spectrum of this system is similar to that shown in Fig. 7.6. Therefore, Eq. (7.28) reduces to,

$$P_{surv} = P_0(\Delta) + 4\rho_1 q_0^2 p_0 \cos^2(\phi_0/2). \tag{7.29}$$

Consider the case in which both Δ and λ are held fixed and the sweep rate v is varied. An inspection of Eq. (7.29) reveals that whenever v is tuned such that $\phi_0 = (2n+1)\pi$ with $n = 0, 1, 2, ...$ the second term vanishes which implies that the paths between $|1_+, +\rangle$ and $|0_+, +\rangle$ interfere destructively. However, in the case of $\phi_0 = 2n\pi$ the paths exhibit constructive interference. This means that the path interference can be controlled by tuning the sweep rate which in turn changes the amount of "flux" enclosed by the adiabatic states between different paths. In a sense, the physics of this system are very similar to that of a Mach-Zender Interferometer (MZ). Here, an incoming optical signal is split into two paths via a beam splitter, each having a different path length. These signals are then recombined through another beam splitter. An interference is setup between the two signals which depends on the path length difference. In our case, the role of the beam splitters are played by the crossings at times $\pm t_o$ and path interference is adjusted by modifying the flux ϕ_0. This type of analogy between LZ transitions and MZ has been proposed previously [140] and observed more recently in experiments with flux [129] and charge [128]

qubits under strong AC driving conditions.

In general, due to the complex form of the phase ϕ_o it is difficult to obtain a simple relation for which sweep rate can be tuned such that interference can be observed. However, in the case when $\Delta = \lambda$, all four of the anti-crossings between the diabatic states $|0, \pm\rangle$ and $|1, \pm\rangle$ have the same energy gap $\Delta E = \lambda$. This implies that the Stokes' phase contribution cancels out in ϕ_0 and so one only needs to consider the dynamical phase Φ_0^D in (7.27). Exploiting the fact that $\lambda \ll \Omega$ allows this to be easily calculated yielding $\phi_0 = \Omega^2/v$. Thus constructive (destructive) interference occurs when the sweep rate is

$$v = \Omega^2/(m\pi) \tag{7.30}$$

where m is an even (odd) integer. This implies that when the survival probability is plotted as a function of sweep rate with λ held fixed this will exhibit oscillatory behavior, as illustrated in the lower curve of Fig. 7.7. Finally, we

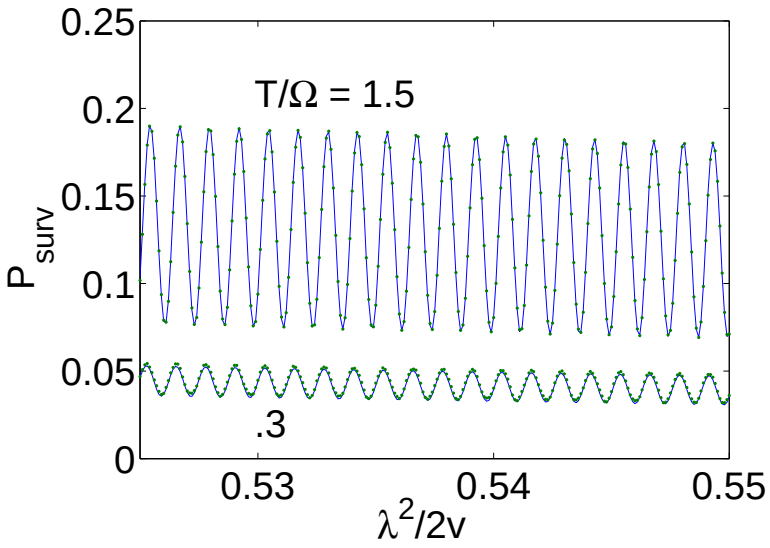

Figure 7.7: Survival probability when $\Delta = \lambda$ plotted as a function of $\lambda^2/(2v)$ where λ is held fixed at $.02\Omega$ and the sweep rate v is varied. Here the Stückelberg oscillations are clearly visible. Two different temperature regimes are shown and the comparison is made between the analytical expressions (solid lines) and the full numerical solution (dotted) to the propagator in Eq. (7.10).

consider the case for arbitrary temperatures. As the temperature is increased so does the occupation probability for energy levels above the ground state.

Therefore, as illustrated in Fig. 7.7, the amplitude of the Stückelberg oscillations increases with the temperature of the oscillators state. Furthermore, as can be seen by inspecting Eq. (7.28) the oscillations are composed of a number of path interferences between separate groups of diabatic states differing by one photon, as in Fig. 7.6. In these higher photon number states, the energy gaps of the anticrossings are no longer equal as in the low temperature case. This implies that the condition for constructive/destructive interference (7.30) is not valid and the result is that each of the oscillations exhibit interference maxima or minima at different values of the sweep rate. This leads to a slight phase shift in the oscillation pattern of the survival probability when compared against the low temperature case, as shown in Fig. 7.7.

In the limit of $v \ll \lambda$ an approximate expression can be developed for the survival probability. In this case, dominant term in Eq. (7.28) is $n = 1$ whereas all others are exponentially suppressed in this limit. Therefore, in this limit the survival probability is,

$$P_{surv} = P_0(\Delta) + P_2(\Delta) + 4\rho_1 q_0^2 p_0 \cos^2(\phi_0/2) \tag{7.31}$$

which is the same as the low temperature case, Eq. (7.29), except with the addition of the two-photon transition term $P_2(\Delta)$ which contributes for finite temperatures. The above equation implies that in the adiabatic limit only path interference in the between the two lowest lying diabatic states contribute to the Stückelberg Oscillations.

7.2.4 Conclusions and Experimental Prospect

As eluded to at the beginning of this section these results have relevance to current experiments in CQED [28, 29]. In these systems, the role of the qubit is played by a Cooper Pair Box [28, 141], or Josephson charge qubit [142]. Here, a superconducting island is coupled by two Josephson tunnel junctions to superconducting reservoirs. In the regime when the number of cooper pairs on the island differs by one, the system can be described by the two state Hamiltonian,

$$H_Q = \frac{1}{2}\left(E_J\sigma_z + \Delta\sigma_x\right) \tag{7.32}$$

where, E_J is the Josephson energy and Δ is the electrostatic energy of the island. The Josephson energy can be modified by applying an external flux bias Φ_b to the system so that $E_j = E_{J,max}\cos(\pi\Phi_b)$. As pointed out in Refs. [131–133] Φ_b can be modified such that the linear sweep required for LZ transitions can be emulated. Furthermore, Δ can be tuned via an external gate bias V_g coupled to the island via a capacitance C_g. The gate bias induces a charge

on the island $n_g = V_g C_g/e$ so that $\Delta = 4E_C(n_g - 1/2)$, where E_C is the coulomb charging energy. The resonator in these systems is realized by a superconducting transmission line which is then capacitively coupled to the qubit. The total Hamiltonian for this system is given by,

$$H = H_Q + \Omega a^\dagger a + \frac{\lambda}{2}\left(a^\dagger + a\right)\left[\sigma_x + n_g - 1/2\right], \tag{7.33}$$

where λ is the coupling strength between the qubit and the oscillator. Experimentally [28], coupling strengths of $\lambda/\Omega \approx 10^{-3}$ are common in these systems. Furthermore, recent experiments [30] allow for the possibility of initializing the oscillator in a thermal state. Here, the cavity can be populated in either a thermal state or coherent state by applying the appropriate drive signals to the oscillator. As one can see the case in which $\Delta = 0$ is obtained by setting the charge qubit to its degeneracy point ($n_g = 1/2$) which is also the point in which qubit decoherence is minimized [142]. In fact, for this case the asymptotic limits $v << \lambda$ of the survival probability apply to cases where the cavity is initialized in a coherent state such as,

$$|\psi_{coh}\rangle = e^{-|\alpha|^2/2} \sum_n \frac{\alpha^n}{\sqrt{n!}} |n\rangle \tag{7.34}$$

then in the adiabatic limit,

$$P_{surv} = 1 - e^{-\langle N\rangle}\left[1 + \langle N\rangle\right], \tag{7.35}$$

where, $\langle N\rangle = |\alpha|^2$ is the average photon number of the state.

Turing to the case in which $\Delta \neq 0$ such a situation can occur whenever the qubit is tuned off of its degeneracy point. However, some care should be taken in this case for two reasons. First, as shown in the Hamiltonian (7.33) off the degeneracy point an additional coupling term comes into play which tends to shift the equilibrium position of the oscillator. Anticipating this Δ was chosen in this work such that $\lambda(n_g - 1/2)/2 \sim \lambda^2$. Therefore effect of this term is negligible and the Hamiltonian given by (7.11) is an excellent approximation.

Secondly, tuning the qubit off of its resonance point dramatically increases the decoherence rate in the qubit [143]. Since the Stückelberg oscillations arise due to the fact the system maintains coherence throughout the entire evolution, the detuning of n_q should be relatively small.

To summarize, this section has focused on LZ transitions in a qubit coupled to a harmonic oscillator. It has been shown that the coupling of the qubit to the oscillator system allows for the possibility of drastic modifications to the survival probability of the qubit due to the fact that the coupling causes a

single anticrossing to split into multiple anticrossings. When the oscillator is initialized in a thermal state described by some temperature T, the system can transit coherently between the different diabatic states. In case when $\Delta = 0$ the survival probability saturates in the adiabatic limit and this value is directly related to the temperature of the oscillators thermal state. For non-vanishing Δ, multipath interference leads to the appearance of Stückelberg oscillations in the survival probability when plotted as a function of the sweep rate v. Increasing the temperature of this state causes the amplitude of these oscillations to increase.

7.3 Decohernce in Adiabatic Quantum Computation

In the next part of the Chapter we concentrate on the Landau-Zener transitions in the presence of decoherence, which is the opposite case to that was considered before. As pointed out at the beginning of this Chapter the motivation here is to evaluate the performance of AQC when the qubit system is subject to strong decoherence. To this end, we consider a model in which LZ transitions occur in the presence of an environment with a continuous spectrum in contrast to the previous case. We use the model of decoherence appropriate for solid-state circuits, where the AQC approach is particularly promising. One characteristic feature of such a model is that it should allow for non-Markovian, in particular low-frequency, environmental noise. Previous studies have mainly considered Markovian environments [56, 124, 144, 145]. A correct description of the interaction with a low-frequency environment, which has the strongest effect on the AQC algorithms [146], requires a non-perturbative or strong-coupling theory of the environment-qubit interaction.

Another feature of our "solid-state" approach is the assumption that the environment responsible for decoherence is in equilibrium at some temperature T, and is sufficiently large to enforce (on some time scale) the equilibration among the qubit states at the same temperature. Even the low-frequency noise that dominates the decoherence of the solid-state qubits (see, e.g., [147, 148]) comes usually from equilibrium sources [149]. Previous studies of the AQC decoherence used models that do not account directly for such equilibration [56, 144, 150–152]. Since environment temperature can not be reduced indefinitely, for a sufficiently large system, T will inevitably be larger than the minimum gap g_m. This means that in contrast to closed systems, Landau-Zener transitions in the presence of decoherence are intrinsically linked to thermal excitations out of the ground state, making it necessary to consider the two

types of the transitions simultaneously.

7.3.1 Model

Quantitatively, we introduce the decoherence as usual by adding the bath H_B and the interaction Hamiltonian $H_{\rm int}$ to the Hamiltonian H_S of the qubit register: $H_{\rm total}$=$H_S + H_B + H_{\rm int}$. As discussed above, we use the two-state approximation near the anticrossing, assuming that g_m is much smaller than the energy gaps separating the first two from the other levels. This two state approximation is in general valid for the minimum gaps that result from first order quantum phase transitions. For the second order quantum phase transitions, other methods become necessary, see e.g. [153].

$$H_S = -(\epsilon\sigma_z + g_m\sigma_x)/2, \qquad H_{\rm int} = -Q\sigma_z/2, \tag{7.36}$$

where σ's are the Pauli matrices, Q is an operator of the environmental noise, $\epsilon \equiv E(s-s_m)$ with $E \gg g_m$ defining the energy scale which characterizes the anticrossing at $s = s_m$. Independent couplings of individual qubits to their environments produce only the σ_z-coupled noise in the two-state model (7.36) [124]. We assume that the noise is Gaussian so that we do not need to specify H_B explicitly. Then, all averages can be expressed in terms of the spectral density:

$$S(\omega) = \int_{-\infty}^{\infty} dt\ e^{i\omega t}\langle Q(t)Q(0)\rangle,$$

where $\langle ...\rangle$ denotes averaging over the environment. Gaussian noise is expected if the environment consists of a large number of degrees of freedom all weekly coupled to the system [61].

In the regime of incoherent Landau-Zener transitions considered here, both the environment-induced broadening W of the two basis states of the Hamiltonian (7.36) and temperature T are taken to be much larger than g_m. This means that the time ($\sim 1/W$), during which the two states lose their relative phase coherence, is much smaller than the typical tunnelling time ($\sim 1/g_m$) which implies that the tunnelling between these states will be incoherent. In particular, the off-diagonal elements of the density matrix ρ of the system (7.36) vanish within the time $\tau_{\rm decoh} \sim 1/W$ so that ρ reduces to diagonal elements, i.e. to $\rho_z \equiv p_0 - p_1$, which is governed by the usual kinetic equation

$$\dot\rho_z = -\Gamma(\rho_z - \rho_\infty), \tag{7.37}$$

where $\Gamma = \Gamma_{01} + \Gamma_{10}$ and $\rho_\infty = [\Gamma_{10} - \Gamma_{01}]/\Gamma$. Here we use the standard notations: $|0\rangle$ and $|1\rangle$ are the two eigenstates of σ_z with eigenvalues ∓ 1, re-

spectively, p_j is the occupation probability of state $|j\rangle$, and Γ_{ij} is the rate of tunnelling from state $|i\rangle$ to $|j\rangle$.

The physics behind such an incoherent tunnelling is the same as for macroscopic resonant tunnelling (MRT) of flux in superconducting flux qubits which has been studied experimentally [149] and theoretically [154]. In particular, the transition rates have the structure of resonant peaks of width W in the vicinity of the anticrossing point. These rates can be explicitly calculated by a perturbation expansion in g_m and assuming Gaussian noise [154]:

$$\Gamma_{01}(\epsilon) = \frac{g_m^2}{4} \int dt e^{i\epsilon t} \exp\left\{ \int \frac{d\omega}{2\pi} S(\omega) \frac{e^{-i\omega t}-1}{\omega^2} \right\}. \tag{7.38}$$

The rate of the backward tunnelling is determined by the relation $\Gamma_{10}(\epsilon) = \Gamma_{01}(-\epsilon)$. In the case of white noise, $S(\omega) = S(0)$, Eq. (7.38) gives the tunnelling peak in the form of a Lorentzian line-shape:

$$\Gamma_{01}(\epsilon) = \frac{1}{2} \frac{g_m^2 W}{\epsilon^2 + W^2}, \qquad W = \frac{1}{2} S(0)\,. \tag{7.39}$$

On the other hand, in the situation characteristic for practical solid-state qubits when the noise is dominated by the low-frequency components, Eq. (7.38) reduces to a shifted Gaussian [154]:

$$\begin{aligned} \Gamma_{01}(\epsilon) &= \sqrt{\frac{\pi}{8}} \frac{g_m^2}{W} \exp\left\{ -\frac{(\epsilon-\epsilon_p)^2}{2W^2} \right\}, \\ W^2 &= \int \frac{d\omega}{2\pi} S(\omega), \qquad \epsilon_p = \mathcal{P} \int \frac{d\omega}{2\pi} \frac{S(\omega)}{\omega}. \end{aligned} \tag{7.40}$$

For the environment in thermal equilibrium, the width W and the position ϵ_p of the Gaussian are related by [154]:

$$W^2 = 2T\epsilon_p\,. \tag{7.41}$$

These theoretical results have been experimentally confirmed in flux qubits [149].

7.3.2 Results

Let us first study the kinetic equation (7.37) in two extreme cases. In the small-T regime $\rho_\infty \simeq \operatorname{sgn}\epsilon$ which implies, with the initial condition $\rho_z(0) = 1$, that the right hand side of (7.37) is nonzero only for $\epsilon > 0$. This leads to the

ground state probability

$$p_G = 1 - e^{-\gamma t_f}, \tag{7.42}$$

$$\gamma \equiv \frac{1}{t_f}\int_0^\infty \Gamma(\epsilon)\frac{d\epsilon}{\dot{\epsilon}} = \frac{1}{t_f}\int_{-\infty}^\infty \Gamma_{01}(\epsilon)\frac{d\epsilon}{\dot{\epsilon}}\,. \tag{7.43}$$

We shall see later that under relatively general conditions $\dot{\epsilon} \propto 1/t_f$ and therefore γ is independent of t_f. These equations assume that the range of ϵ is large enough to effectively cover the whole peak of Γ_{01}, therefore justifying infinite integration limits. In particular, the range of ϵ should be larger than (among other energies) the cutoff energy of the environment excitations. In the opposite large-T regime, one has $|\epsilon| \ll T$ and hence $\rho_\infty = 0$ in Eq. (7.37) for energy ϵ within some relevant interval around the anticrossing point $\epsilon = 0$ (this condition is made more precise below). The ground state probability is then

$$p_G = \frac{1}{2}\left(1 - e^{-2\gamma t_f}\right). \tag{7.44}$$

Because of the thermal excitations, p_G approaches 1/2 in the slow-evolution limit. For the intermediate T regime, p_G always falls between (7.42) and (7.44), therefore these equations give, respectively, upper and lower bounds for the probability of success (see Fig. 7.8 and discussion below).

An important feature of (7.38) is that for uniform evolution, i.e., $\dot{\epsilon} = \text{const} \equiv \nu$, it gives $\gamma t_f = \frac{1}{\nu}\int_{-\infty}^\infty \Gamma_{01}(\epsilon)d\epsilon = \pi g_m^2/2\nu$, independently of $S(\omega)$, leading in the small-T regime to the same Landau-Zener probability (7.42) as in the decoherence-free case. This result extends the recent proofs [131, 138, 155] that at $T = 0$ Landau-Zener probability is unaffected by decoherence. The physical reason for this is that the decoherence changes only the profile of the transition region while keeping the total transition probability the same. Therefore, in the two extreme regimes, the ground state probabilities (7.42) and (7.44) are completely independent of the form of the noise spectrum $S(\omega)$.

At intermediate temperatures, on the other hand, the quantitative t_f-dependence of the probability p_G is sensitive to the specific form of $S(\omega)$ and therefore to the tunnelling rates. For Gaussian rates (7.40) and uniform evolution, p_G calculated from Eq. (7.37) is shown in Fig. 7.8. The curves characterize the transition between the low- (7.42) and high- (7.44) temperature limits. At small evolution times when $t_f \ll \gamma^{-1}$ all curves coincide, with $p_G = \gamma t_f$ in the linear approximation, independently of temperature T. The temperature dependence of p_G appears only in the second-order terms in γt_f. For slow evolution, $t_f \geq \gamma^{-1}$, p_G varies from 1 to 1/2 with temperature T – see inset in Fig. 7.8. If the evolution is infinitely slow, the occupation probabilities of the states $|0\rangle$ and $|1\rangle$ should always reach the local thermal equilibrium. This,

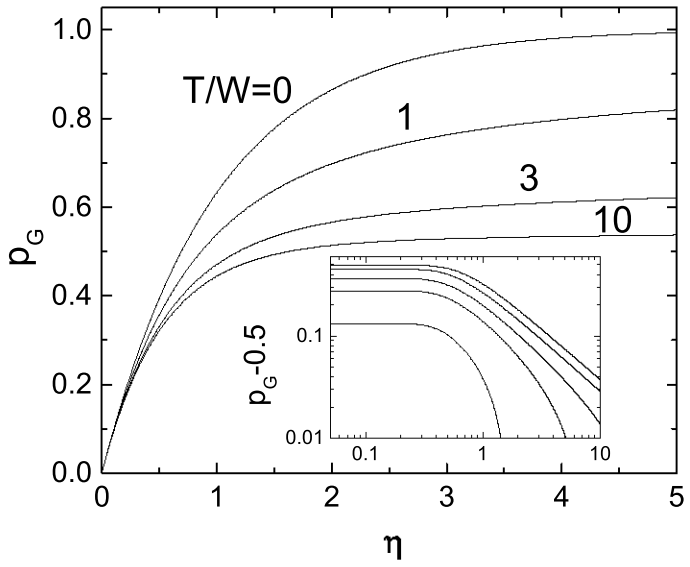

Figure 7.8: The occupation probability p_G of the ground state as a function of the dimensionless evolution time γt_f for different temperatures T in the case of the Gaussian tunnelling rates (7.40). The inset shows the dependence of p_G on T/W for $\gamma t_f = 1$; 1.5; 2; 3; 5 from lower to upper curves respectively.

however, is not the relevant regime for the present discussion. In the relevant case, the rate ν is comparable to the maximum tunnelling rates Γ, and therefore becomes much larger than the tunnelling rates as the system moves away from the resonance, so that the local equilibrium is not maintained. This means that, strictly speaking, the large-T result (7.44) is valid for any t_f only for $T \gg E$. Asymptotic analysis of the evolution equation for the case of the Gaussian rates (7.40) shows that in the more interesting regime when $T \gg W$ but $T \ll E$, the ground-state probability is:

$$p_G = \frac{1}{2} + \frac{W}{\sqrt{2}T}[\ln \gamma t_f]^{1/2}. \tag{7.45}$$

This equation describes the increase of p_G towards the local equilibrium at sufficiently large evolution time t_f, and corresponds to the large-T part of the two curves with larger γt_f in the inset in Fig. 7.8.

7.3.3 Relevance to AQC

We now use the results presented above to discuss the performance of AQC in the incoherent regime $g_m \ll W, T$. For this, one needs to distinguish global and local adiabatic evolutions. In the *global* scheme, the adiabatic evolution is uniform, $\dot{\epsilon} = \text{const} = E/t_f$, and Eqs. (7.42) and (7.44) show that the required computational time $t_f \simeq \gamma^{-1} = 2E/\pi g_m^2$ coincides with the decoherence-free case independently of decoherence and temperature T. Even if the large T reduces p_G to $\simeq 1/2$, to find correct solution, one only needs to repeat the computation process on average two times.

Global adiabatic evolution, however, does not yield the optimal performance in coherent AQC. Indeed, for the case of adiabatic Grover search [151], the global adiabatic scheme yields the complexity of the classical exhaustive search, i.e., $t_f = O(N)$, where N $(= 2^n)$ is the size of data base. In the more efficient *local* scheme [151], one takes $\dot{\epsilon}(t) = \alpha g(t)^2$, so that the adiabatic condition is satisfied uniformly (the system slows down in the region of small gap) and the computation time is $t_f = \pi/\alpha g_m$ which for the case of adiabatic Grover search yields the optimal $O(\sqrt{N})$ performance. The local evolution plays crucial role for the scaling analysis of the AQC [151, 156, 157], although in some cases it is only assumed implicitly. In general, however, finding the gap $g(s)$ is as hard as solving the original problem, and only in some cases, e.g, the adiabatic Grover search, $g(s)$ is independent of the final solution and can be found *a priori* analytically.

The enhanced performance of the local scheme comes at a price of its stronger sensitivity to decoherence. A qualitative reason for sensitivity of local AQC is that although decoherence does not change the total integral transition probability, it distributes it over a much larger energy interval $W \gg g_m$, making it necessary to slow down the evolution for a longer period of time. If one uses the same $\epsilon(t)$ as in the decoherence-free case, the average tunnelling rate (7.43) is dominated by the vicinity of the point $\epsilon = 0$. Quantitatively, $\dot{\epsilon} = \alpha g^2$ and $t_f = \pi/\alpha g_m$ yield $(t_f \dot{\epsilon})^{-1} = g_m/\pi g^2 \approx \delta(\epsilon)$, which together with (7.43) and (7.38) give $\gamma \approx \Gamma_{01}(0) \propto g_m^2$. Therefore the computation time is $t_f \simeq \gamma^{-1} \propto g_m^{-2}$, which is similar to the performance of the global scheme with the only possible enhancement compared to the global case being a prefactor. In the case of white noise, Eq. (7.39) leads to $\gamma = g_m^2/2W$, while for the low-frequency noise, Eq. (7.40) gives $\gamma = \sqrt{\pi/8}(g_m^2/W)e^{-W^2/8T^2}$. Notice that in the latter case, lowering T with constant width W [149] does not shorten the computation time.

7.3.4 Conclusions

To summarize, we have studied the decoherence effects on AQC due to general non-Markovian environments in the strong decoherence regime, in which the broadening of the energy levels completely smears out the anticrossing region. Our strong-coupling treatment shows that global AQC remains unaffected by strong decoherence $W > g_m$ and is independent of the type of noise, while the local AQC provides only a prefactor improvement of the algorithm running time in this regime and does not change the scaling of this time with g_m as compared to the case without decoherence. Thus, the local AQC can only maintain its properties if $W < g_m$. Since $W \sim 1/\tau_{\mathrm{decoh}}$, and $t_f \sim 1/g_m$ for the local scheme in the weak-decoherence regime, the computation time is limited by the decoherence $t_f < \tau_{\mathrm{decoh}}$ in the same way as in gate model QC. Therefore, the advantageous scaling of the local AQC requires phase coherence throughout the evolution as in the gate model. Insensitivity of AQC to decoherence only holds for the global scheme and does not apply to local AQC. It should be emphasized that our results are based on the fact that the two-state model holds, which the broadening of the energy levels and also thermal excitation do not mix the lowest two states with other excited states. For stronger noise or higher temperatures, one needs to take higher states into consideration.

Chapter 8

Conclusions

The work in this dissertation has examined the applications of Quantum Antidots in both charge transport experiments and Quantum Information. The first part of the dissertation presented a model to describe coherent quasiparticle transport in structures involving multiple antidots. The main result is that the anyonic exchange statistics of these quasiparticles is manifested directly in the DC tunnel conductance of these systems even in the absence of quasiparticle exchange. Most notably, it was shown that in tunnelling through a line of three antidots, the statistics should be exhibited as a non-vanishing resonant peak of the tunnel conductance and represents an experimentally viable approach to determining the anyonic exchange statistics of quasiparticles from the Fractional Quantum Hall effect. The second half of the dissertation examined possible applications of quantum antidots in Quantum Information. The use of the quantum antidot electrometer was discussed as a potential detector for FQHE qubits. It was shown that the CLL effects of the edge states entered into the measurement characteristics of the detector. Finally, the non-trivial aspects of wave function reduction in measurements of a single qubit was examined as well as the coherent synchronization of oscillations in a continuously measured double qubit system. Finally, we evaluated the performance of adiabatic quantum computation in the presence of low frequency noise which is particularly applicable to solid state AQC implementations. We showed that in the presence of decoherence, caused by low frequency noise, the insensitivity of AQC to decoherence only holds for the global scheme and does not apply to local AQC.

There are several possible directions in which to extend the work done in this dissertation. As far as charge transport with multiple antidots is concerned, it would be interesting to extend the theory to include quasiparticles to filling fractions other than those belonging to primary quantum hall liquids. This would allow for the possibility to examine how the statistics of

these quasiparticles enter into the DC conductance of multi-anitdot systems. Another avenue of exploration is to examine the measurement characteristics of the QAE in the co-tunnelling regime. It has been shown previously that the single electron transistor in this regime can be made to approach the limit of an ideal detector [99]. Therefore, it is only natural to question whether the QAE can reach this limit. Furthermore, having a detector which could operate in this regime would be a great benefit to Quantum Computation based on FQHE quasiparticles.

Bibliography

[1] D. C. Tsui, H. L. Störmer, and A. C. Gossard, Phys. Rev. Lett. **48**, 1559 (1982).

[2] K. von Klitzig, G. Dorda, and M. Pepper, Phys. Rev. Lett. **45**, 494 (1980).

[3] R. B. Laughlin, Phys. Rev. Lett. **50**, 1395 (1983).

[4] R. B. Laughlin, Rev. Mod. Phys. **71**, 863 (1999).

[5] D. Arovas, J. R. Schrieffer, and F. Wilczek, Phys. Rev. Lett. **53**, 722 (1984).

[6] B. I. Halperin, Phys. Rev. Lett. **52**, 1583 (1984).

[7] V. J. Goldman and B. Su, Science **267**, 1010 (1995).

[8] R. de Picciotto, M. Reznikov, M. Heiblum, V. Umansky, G. Bunin, and D. Mahalu, Nature **389**, 162 (1997).

[9] M. Reznikov, R. de Picciotto, T. Griffiths, M. Heiblum, and V. Umansky, Nature **399**, 238 (1999).

[10] F. Camino, W. Zhou, and V. Goldman, Phys. Rev. Lett. **95**, 246802 (2005).

[11] F. Camino, W. Zhou, and V. Goldman, Phys. Rev. B **72**, 075342 (2005).

[12] E.-A. Kim, Phys. Rev. Lett. **97**, 216404 (2006).

[13] V. J. Goldman, Phys. Rev. B **75**, 045334 (2007).

[14] J. Jain and C. Shi, Phys. Rev. Lett. **96**, 136802 (2006).

[15] B. Rosenow and B. Halperin, Phys. Rev. Lett. **98**, 106801 (2007).

[16] A. Y. Kitaev, Ann. Phys. **303**, 2 (2003).

[17] S. Lloyd, `quant-ph/0004010`.

[18] M. H. Freeman, A. Y. Kitaev, M. J. Larsen, and Z. Wang, `quant-ph/0101025v2`.

[19] J. Preskill, in *Introduction to Quantum Computation and Information*, edited by H. K. Lo, S. Papesku, and T. Spiller (World Scientific, Singapore, 1998), p. 213.

[20] D. V. Averin and V. J. Goldman, Solid State Comm. **121**, 25 (2002).

[21] V. J. Goldman, I. Karakurt, J. Liu, and A. Zaslavsky, Phys. Rev. B **64**, 085319 (2001).

[22] I. J. Maasilta and V. J. Goldman, Phys. Rev. B **57**, R4273 (1998).

[23] M. Kataoka, C. J. Ford, G. Faini, D. Mailly, M. Y. Simmons, D. R. Mace, C.-T. Liang, and D. A. Ritchie, Phys. Rev. Lett. **83**, 160 (1999).

[24] M. R. Geller, D. Loss, and G. Kirczenow, Phys. Rev. Lett. **77**, 5110 (1996).

[25] A. Braggio, M. Merlo, N. Magnoli, and M. Sassetti, Phys. Rev. B **74**, 041304R (2006).

[26] D. V. Averin, in *Quantum Noise in Mesoscopic Physics*, edited by Y. V. Nazarov (Kluwer, Dordrecht, 2003), p. 229.

[27] D. V. Averin, in *Exploring the Quantum- Classical Frontier: Recent Advances in Macroscopic and Mesoscopic Quantum Phenomena*, edited by J. R. Friedman and S. Han (Nova, New York, 2003), p. 447.

[28] A. Wallraff, D. I. Schuster, A. Blais, L. Frunzio, R.-S. Huang, J. Majer, S. Kumar, S. M. Girvin, and R. J. Schoelkopf, Nature **431**, 162 (2004).

[29] I. Chiorescu, P. Bertet, K. Semba, Y. Nakamura, C. J. P. M. Harmans, and J. E. Mooij, Nature **431**, 159 (2004).

[30] D. I. Schuster, A. A. Houck, J. A. Schreier, A. Wallraff, J. M. Gambetta, A. Blais, L. Frunzio1, J. Majer, B. Johnson, M. H. Devoret, et al., Nature **445**, 515 (2007).

[31] J. M. Leinaas and J. Myrheim, Nuovo Cimento B **37**, 1 (1977).

[32] F. Wilczek, Phys. Rev. Lett. **48**, 1144 (1982).

[33] B. I. Halperin, Phys. Rev. B **25**, 2185 (1982).

[34] X. G. Wen, Adv. Phys. **44**, 405 (1995).

[35] X. G. Wen, Phys. Rev. B **43**, 11025 (1991).

[36] X. G. Wen, Phys. Rev. Lett. **64**, 2206 (1990).

[37] X. G. Wen, Phys. Rev. B **44**, 12838 (1990).

[38] X. G. Wen, Int. J. Mod. Phys. B **6**, 1711 (1992).

[39] M. Stone and M. P. A. Fisher, Int. J. Mod. Phys. B **8**, 2539 (1994).

[40] M. Grayson, D. C. Tsui, L. N. Pfeiffer, K. W. West, and A. M. Chang, Phys. Rev. Lett. **80**, 1062 (1998).

[41] A. M. Chang, L. N. Pfeiffer, and K. W. West, Phys. Rev. Lett. **77**, 2538 (1996).

[42] A. M. Chang, Rev. Mod. Phys. **75**, 1449 (2003).

[43] I. J. Maasilta and V. J. Goldman, Phys. Rev. B **55**, 4081 (1997).

[44] C. L. Kane and M. P. A. Fisher, Phys. Rev. Lett. **72**, 724 (1994).

[45] M. Grayson, D. C. Tsui, L. N. Pfeiffer, K. W. West, and A. M. Chang, Phys. Rev. Lett. **86**, 2645 (2001).

[46] I. J. Maasilta, Ph.D. thesis, Stony Brook University (1998).

[47] D. V. Averin and K. K. Likharev, in *Mesoscopic Phenomena in Solids*, edited by B. Altshuler, P. Lee, and R. Webb (Elsevier, Amsterdam, 1991), p. 173.

[48] L. P. Kouwenhoven, C. M. Marcus, P. L. Mceuen, S. Tarucha, R. M. Westervelt, and N. S. Wingreen, in *Mesoscopic Electron Transport*, edited by L. Sohn, L. Kouwenhoven, and G. Schön) (Kluwer, Dordrecht, 1997), p. 105.

[49] D. Deutsch, Proc. R. Soc. London Ser. A **400**, 97 (1985).

[50] M. A. Nielsen and I. L. Chuang, *Quantum Computation and Quantum Information* (Cambridge University Press, 2000).

[51] P. W. Shor, in *Proceedings of the 35th Annual Symposium on the Foundations of Computer Science* (IEEE Press, Los Alamitos, CA, 1994).

[52] L. K. Grover, Phys. Rev. Lett. **79**, 325 (1997).

[53] D. Simon, in *Proceedings of the 35th Annual Symposium on the Foundations of Computer Science* (IEEE Press, Los Alamitos, CA, 1994), p. 116.

[54] E. Farhi, J. Goldstone, S. Gutmann, and M. Sipser, `quant-ph/0001106`.

[55] E. Farhi, J. Goldstone, and S. Gutmann, `quant-ph/0007071`.

[56] A. Childs, E. Farhi, J. Goldstone, and S. Gutmann, `quant-ph/0012104`.

[57] E. Farhi, J. Goldstone, S. Gutmann, J. Lapan, A. Lundgren, and D. Preda, Science **292**, 472 (2001).

[58] A. Mizel, M. W. Mitchell, and M. L. Cohen, Phys. Rev. A **63**, 040302(R) (2001).

[59] J. von Neumann, *Mathematical Foundations of Quantum Mechanics* (Princeton University Press, Princeton, 1955).

[60] J. A. Wheeler and W. H. Zurek, *Quantum Theory and Measurement* (Princeton University Press, Princeton, 1984).

[61] A. J. Leggett, S. Chakravarty, A. T. Dorsey, M. P. A. Fisher, A. Garg, and W. Zwerger, Rev. Mod. Phys. **59**, 1 (1987).

[62] A. Korotkov, Phys. Rev. B **60**, 005737 (1999).

[63] S. A. Gurvitz, Phys. Rev. B **56**, 15215 (1997).

[64] Y. Makhlin, G. Schön, and A. Shnirman, Phys. Rev. Lett. **85**, 4578 (2000).

[65] D. V. Averin, Fort. d. Phys. **48**, 1055 (2000).

[66] S.-X. Li, Y. Yu, Y. Zhang, W. Qiu, S. Han, and Z. Wang, Phys. Rev. Lett. **89**, 098301 (2002).

[67] A. A. Clerk, S. M. Girvin, and A. D. Stone, Phys. Rev. B **67**, 165324 (2003).

[68] A. Messiah, *Qauntum Mechanics* (North-Holland, Amsterdam, 1961), ch. 27.

[69] L. Saminadayar, D. C. Glattli, Y. Jin, and B. Etienne, Phys. Rev. Lett. **79**, 2526 (1997).

[70] D. V. Averin and J. A. Nesteroff, Physica E **40**, 58 (2007).

[71] D. V. Averin, Solid State Comm. **105**, 659 (1998).

[72] A. Shnirman, G. Schön, and Z. Hermon, Phys. Rev. Lett. **79**, 2371 (1997).

[73] Y. Makhlin, G. Schön, and A. Shnirman, Nature **398**, 305 (1999).

[74] D. J. Flees, S. Han, and J. E. Lukens, Phys. Rev. Lett. **78**, 4817 (1997).

[75] Y. Nakamura, C. D. Chen, and J. S. Tsai, Phys. Rev. Lett. **79**, 2328 (1997).

[76] S. D. Sarma, M. Freedman, and C. Nayak, Phys. Rev. Lett. **94**, 166802 (2005).

[77] L. S. Georgiev, Phys. Rev. B **74**, 235112 (2006).

[78] V. V. Ponomarenko and D. V. Averin, JETP Lett. **74**, 87 (2001).

[79] V. V. Ponomarenko and D. V. Averin, Phys. Rev. B **70**, 195316 (2004).

[80] I. Safi, P. Devillard, and T. Martin, Phys. Rev. Lett. **86**, 4628 (2001).

[81] C. L. Kane, Phys. Rev. Lett. **90**, 226802 (2003).

[82] V. V. Ponomarenko and D. V. Averin, Phys. Rev. B **71**, 241308(R) (2005).

[83] K. T. Law, D. E. Feldman, and Y. Gefen, Phys. Rev. B **74**, 045319 (2006).

[84] D. V. Averin and J. A. Nesteroff, Phys. Rev. Lett. **99**, 096801 (2007).

[85] D. V. Averin and A. N. Korotkov, Sov. Phys. JETP **70**, 937 (1990).

[86] C. W. Beenakker, Phys. Rev. B **44**, 1646 (1991).

[87] D. V. Averin, A. N. Korotkov, and K. K. Likharev, Phys. Rev. B **44**, 6199 (1991).

[88] C. de C. Chamon and X. G. Wen, Phys. Rev. Lett. **70**, 2605 (1993).

[89] A. Furusaki and N. Nagaosa, Phys. Rev. B **47**, 3827 (1993).

[90] X. G. Wen, Phys. Rev. B **44**, 5708 (1991).

[91] Y. Oreg and A. M. Finkel'stein, Phys. Rev. Lett. **74**, 3668 (1995).

[92] V. J. Goldman and E. Tsiper, Phys. Rev. Lett. **86**, 5841 (2001).

[93] E. Fradkin, *Field Theories of Condensed Matter Systems* (Addison-Wesley, Redwood City, 1991), ch. 7.

[94] J.-X. Zhu and Z. Wang, Phys. Rev. A **53**, 600 (1996).

[95] M. Batchelor, X.-W. Guan, and N. Oelkers, Phys. Rev. Lett. **96**, 210402 (2006).

[96] M. D. Girardeau, Phys. Rev. Lett. **97**, 100402 (2006).

[97] A. Aassime, G. Johansson, G. Wendin, R. J. Schoelkopf, and P. Delsing, Phys. Rev. Lett. **86**, 3376 (2001).

[98] B. E. Kane, N. S. McAlpine, A. S. Dzurak, R. G. Clark, G. J. Milburn, H. B. Sun, and H. Wiseman, Phys. Rev. B **61**, 2961 (2000).

[99] D. V. Averin, in *Macroscopic Quantum Coherence and Quantum Computing*, edited by D. V. Averin, B. Ruggiero, and P. Silvestrini (Kluwer Academic, New York, 2000), p. 399.

[100] A. Braggio, R. Fazio, and M. Sassetti, Phys. Rev. B **67**, 233308 (2003).

[101] M. Merlo, A. Braggio, N. Magnoli, and M. Sassetti, Phys. Rev. B **75**, 195332 (2007).

[102] A. Braggio, N. Magnoli, M. Merlo, and M. Sassetti, Phys. Rev. B **74**, 041304 (2006).

[103] A. N. Korotkov, Phys. Rev. B **49**, 10381 (1994).

[104] J. H. Davies, P. Hyldgaard, S. Hershfield, and J. W. Wilkins, Phys. Rev. B **46**, 9620 (1992).

[105] W. Mao, D. V. Averin, R. Ruskov, and A. N. Korotkov, Phys. Rev. Lett. **93**, 056803 (2004).

[106] W. Mao, D. V. Averin, F. Plastina, and R. Fazio, Phys. Rev. B **71**, 085320 (2005).

[107] B. Trauzettel, A. N. Jordan, C. W. J. Beenakker, and M. Büttiker, Physical Review B **73**, 235331 (2006).

[108] G. Lüders, Ann. Phys. (Leipzig) **8**, 322 (1951).

[109] M. Goldberger and K. Watson, Phys. Rev. **134**, B919 (1964).

[110] J. Bell and M. Nauenberg, in *Preludes in Theoretical Physics* (North Holland, Amsterdam, 1966), p. 279.

[111] J. S. Bell, *Speakable and Unspeakable in Quantum Mechanics* (Cambridge University Press, 1987).

[112] A. Peres, *Quantum Theory* (Kluwer, 1993), chap. 12.

[113] A. Einstein, B. Podolsky, and N.Rosen, Phys. Rev. **47**, 777 (1935).

[114] J. Bell, Physics **1**, 195 (1965).

[115] D. Averin, K. Rabenstein, and V. Semenov, Phys. Rev. B **73**, 094504 (2006).

[116] D. Averin and E. Sukhorukov, Phys. Rev. Lett. **95**, 126803 (2005).

[117] A. Leggett and A. Garg, Phys. Rev. Lett. **54**, 857 (1985).

[118] A. Korotkov and D. Averin, Phys. Rev. B **64**, 165310 (2001).

[119] R. Ruskov, A. Korotkov, and A. Mizel, Phys. Rev. Lett. **96**, 200404 (2006).

[120] A. Jordan, A. Korotkov, and M. Buttiker, Phys. Rev. Lett. **97**, 026805 (2006).

[121] N. Chtchelkatchev, G. Blatter, G. Lesovik, and T. Martin, Phys. Rev. B **66**, 161320 (2002).

[122] C. Beenakker, C. Emary, M. Kindermann, and J. van Velsen, Phys. Rev. Lett. **91**, 147901 (2003).

[123] P. Samuelsson, E. Sukhorukov, and M.Buttiker, Phys. Rev. Lett. **92**, 026805 (2004).

[124] M. H. S. Amin, C. J. S. Truncik, and D. V. Averin, `arXiv:0803.1196`.

[125] L. D. Landau, Phys. Z. Sowjetunion **2**, 46 (1932).

[126] C. Zener, Proc. Roy. Soc. London A **137**, 696 (1932).

[127] E. C. G. Stueckelburg, Helv. Phys. Acta **5**, 369 (1932).

[128] M. Sillanpaa, T. Lehtinen, A. Paila, Y. Makhlin, and P. Hakonen, Phys. Rev. Lett. **96**, 187002 (2006).

[129] W. D. Oliver, Y. Yu, J. C. Lee, K. K. Berggren, L. S. Levitov, and T. P. Orlando, Science **310**, 1653 (2005).

[130] M. H. S. Amin, D. V. Averin, and J. A. Nesteroff, Phys. Rev. A **79**, 022107 (2009).

[131] K. Saito, M. Wubs, S. Kohler, Y. Kayanuma, and P. Hanggi, Phys. Rev. B. **75**, 214308 (2007).

[132] M. Wubs, S. Kohler, and P. Hanggi, Physica E **40**, 187 (2007).

[133] K. Saito, M. Wubs, S. Kohler, P. Hänggi, and Y. Kayanuma, Euro. Phys. Lett **76**, 547 (2006).

[134] S. Brundobler and V. Elser, J. Phys. A **26**, 1211 (1993).

[135] A. V. Shytov, Phys. Rev. A. **70**, 052708 (2004).

[136] N. A. Sinitsyn, J. Phys. A **37**, 10691 (2004).

[137] M. V. Volkov and V. N. Ostrovsky, J. Phys. B **38**, 907 (2005).

[138] M. Wubs, K. Saito, S. Kohler, P. Hänggi, and Y. Kayanuma, Phys. Rev. Lett. **97**, 200404 (2006).

[139] V. N. Ostrovsky, M. V. Volkov, J. P. Hansen, and S. Selstø, Phys. Rev. B **75**, 014441 (2007).

[140] A. V. Shytov, D. A. Ivanov, and M. V. Feigel'man, Eur. Phys. J. B. **36**, 263 (2003).

[141] D. V. Averin, A. B. Zorin, and K. K. Likharev, Sov. Phys. JETP **61**, 407 (1985).

[142] Y. Makhlin, G. Schön, and A. Shnirman, Rev. Mod. Phys. **73**, 357 (2001).

[143] T. Duty, D. Gunnarsson, K. Bladh, and P. Delsing, Phys. Rev. B **69**, 140503 (2004).

[144] J. Aberg, D. Kult, and E. Sjöqvist, Phys. Rev. A **71**, 060312 (2005).

[145] M. Amin, P. Love, and C. Truncik, Phys. Rev. Lett. **100**, 060503 (2008).

[146] M. Tiersch and R. Schützhold, Phys. Rev. A **75**, 062313 (2007).

[147] G. Ithier, E. Collin, P. Joyez, P. J. Meeson, D. Vion, D. Esteve, F. Chiarello, A. Shnirman, Y. Makhlin, J. Schriefl, et al., Phys. Rev. B **72**, 134519 (2005).

[148] J. M. Martinis, K. B. Cooper, R. McDermott, M. Steffen, M. Ansmann, K. D. Osborn, K. Cicak, S. Oh, D. P. Pappas, R. W. Simmonds, et al., Phys. Rev. Lett. **95**, 210503 (2005).

[149] R. Harris, M. W. Johnson, S. Han, A. J. Berkley, J. Johansson, P. Bunyk, E. Ladizinsky, S. Govorkov, M. C. Thom, S. Uchaikin, et al., Phys. Rev. Lett. **101**, 117003 (2008).

[150] M. Sarandy and D. Lidar, Phys. Rev. Lett. **95**, 250503 (2005).

[151] J. Roland and N. J. Cerf, Phys. Rev. A **65**, 042308 (2002).

[152] S. Ashhab, J. R. Johansson, and F. Nori, Phys. Rev. A **74**, 052330 (2006).

[153] S. Mostame, G. Schaller, and R. Schtzhold, Phys. Rev. A **76**, 030304(R) (2007).

[154] M. H. S. Amin and D. V. Averin, Phys. Rev. Lett. **100**, 197001 (2008).

[155] A. Wan, M. Amin, and S. Wang, `cond-mat/0703085`.

[156] E. Farhi, J. Goldstone, S. Gutmann, and D. Nagaj, Int. J. Quantum Inf. **6**, 503 (2008).

[157] L. M. Ioannou and M. Mosca, Int. J. Quantum Inf. **6**, 419 (2008).